Membrane Interactions of Human Annexin A1 and Plant Annexins

Nien-Jen Hu

Ph.D. thesis

The University of Edinburgh

December 2007

EX BIBL UNIV EDINBURGH

Abstract

Calcium plays a vital role as a second messenger in the signal transduction. Numerous proteins change their conformations or cellular localisation in response to fluctuations in the cytosolic calcium level. Annexins constitute a protein family regulated by calcium. Most members of the protein family share a unique calcium binding site, different from E-F hand and C2 domain proteins. The calcium ions harboured in the binding sites allow annexins to associate with negatively charged membrane phospholipids. Although the physiological functions of annexins are not well characterised, it is believed that annexins are involved in membrane domain organisation and cytoskeleton.

In addition to membrane binding, human annexin A1 (AnxA1) shows an extraordinary ability in membrane aggregation. The helical N-terminal domain of AnxA1 inserts into the C-terminal core in the absence of calcium. Upon calcium binding, the N-terminal domain is exposed, and previous studies have suggested that it harbours a secondary, calcium-independent membrane binding site.

In this study, the domain movement of AnxA1 in response to Ca^{2+} in the presence of phospholipid membrane was studied using the intrinsic fluorophore Tryptophan 12 on its N-terminal domain. Increases in fluorescence intensity and blue shift of emission peak wavelength show that the N-terminal domain has a hydrophobic interaction with phospholipids. Neutron diffraction profiles of multi-stack phospholipid bilayers in the presence of AnxA1 N-terminal peptides indicate that the peptides lie parallel to the surface of phospholipid bilayers. These results support the notion that the N-terminal domain interacts with membranes in a calcium-independent manner. A model where membrane aggregation is mediated simultaneously by the two membrane binding sites of one AnxA1 molecule is thus possible.

Plant annexins, annexin Gh1 from *Gossypium hirsutum* and annexin 24 from *Capsicum annuum* (Anx(Gh1) and Anx24(Ca32), respectively), have been reported to possess a calcium-dependent membrane binding behaviour similar to animal annexins. Interestingly, hydrophobic and positively charged residues are well conserved among plant annexins, and fully exposed on the convex side (canonical membrane binding side) of the C-terminal core surface. In this study, Anx(Gh1) and Anx24(Ca32) are demonstrated to also possess calcium-independent membrane binding activity, which is directly attributed to these conserved surface residues. Anx(Gh1) was successfully crystallised using high concentration of $CaCl_2$ in a phosphate crystallisation buffer. Three Ca^{2+} ions are localised in the Ca^{2+}-bound structure presenting typical Ca^{2+} coordination geometries observed in animal annexins.

Two adjacent cysteine residues, Cys116 and Cys243, have been speculated to carry a putative RedOx function of Anx(Gh1). Such a function could explain the inhibitory role of Anx(Gh1) in plant cellulose synthesis, which requires oxidised cellulose synthase (CesA). The RedOx activity of Cys116 and Cys243 was probed using trypsin digest mapping of Anx(Gh1) with H_2O_2 treatment. These experiments, as well as the crystal structure of Anx(Gh1) under oxidising conditions, indicate that the two cysteine residues remain in a reduced state.

Declaration

This thesis is a presentation of my original research work. Wherever contributions of others are involved, every effort is made to indicate this clearly, with due reference to the literature, and acknowledgement of collaborative research and discussions.

The work was done under the guidance of Dr Andreas Hofmann and Dr Jeremy Bradshaw, at the Institute of Structural & Molecular Biology, School of Biological Sciences, The University of Edinburgh, UK.

Nien-Jen Hu

Signature 

Date 31/03/08

Acknowledgements

I would like to take this opportunity to offer my great gratitude to a number of people without whose help and support this thesis would never have been possible.

It is difficult to overstate my gratitude to my primary Ph.D. supervisor, Dr. Andreas Hofmann, who helped me to construct my research project, and provided me directions and sharp criticism while I was writing the thesis. He is the role model who influences my research career so deeply. I also thank to my secondary supervisor, Dr. Jeremy Bradshaw, for his inspiration and warm support. It has always been a great pleasure working with him.

I would like to acknowledge many people who help me to accomplish my experiments: Dr. Adlina Yusof who instructed me the lab techniques of protein expression and purification; Dr. Marjorie Harding who taught me the fundamental knowledge of X-ray crystallography and Dr. Iain McNae who gave practical courses in solving crystal structure; Dr. Thomas Hauss, Dr. Silvia Dante, Dr. Hans Lauter and Dr. Richard Heenan, who offered great supports and detailed discussions at neutron instruments.

I thank to my work colleagues who gave me stimulating encouragement and kind assistance: Koklian Ho, Dr. Daphne Kan, Anja Winter and Marc Daley in lab work; Dr. Paul Taylor, Yi-Gong Sheng, Kun-Yi Hsin and Farid Saadedin for IT support. I am especially grateful to Dr. Kirsten Lily and Jillian Adie for advices of thesis style and proofreading.

I cannot end without thanking my parents, on whose financial support and constant encouragement I have relied throughout my time at the Academy. I want express gratitude to my brother, Nien-Chia, and sister in law, Mei-Chuan, for taking care of my parents. Without their support, I would not be able to study in Edinburgh.

Lastly, I would like to give my immense pleasure to thank my beloved wife, Tzy-Wen, who always gives me the solid support and endless love. I dedicate the work to her and the oncoming baby.

Abbreviations

A_{260}	light absorption at wavelength 260 nm
A_{280}	light absorption at wavelength 280 nm
ACDP	Automated CD Data Processing
AFDP	Automated Fluorescence Data Processing
Anx(Gh1)	cotton *Gossypium hirsutum* annexin
Anx24(Ca32)	bell pepper *Capsicum annuum* annexin
AnxA1	annexin A1
AnxA5	annexin A5
CCP4	The Collaborative Computational Project Number 4 in Protein Crystallography
CD	circular dichroism
CesA	cellulose synthase
CHCA	α-cyano-4-hydroxycinnamic acid
ΔG	Gibbs energy changes
ΔH	enthalpy changes
ΔS	entropy changes
DMPA	1,2-Diimyristoyl-sn-Glycero-3-Phosphatidic acid
DMPC	1,2-Dimyristoyl-sn-Glycero-3-Phosphocholine
DMPS	1,2-Dimyristoyl-sn-Glycero -3-Phosphoserine
DSC	differential scanning calorimetry
EDTA	ethylenediaminetetraacetic acid
ER	endoplamic reticulum
ESI-MS	electrospray mass spectroscopy
HEPES	4-(2-hydroxyethyl)-1-piperazineethanesulfonic acid
ICAM-1	intracellular adhesion molecule 1
ILL	Institut Laue-Langevin
$InsP_3$	inositol-1,4,5-trisphospate
IPTG	isopropyl-1-thio-β-D-galactopyranoside
ITC	isothermal titration calorimetry
K_d	binding affinity constant

kD	kilodalton
λ_{ex}	excitation wavelength
λ_{max}	emission maximum wavelength
LUV	large unilamellar vesicle
m/z	mass to charge ratio
MALDI	matrix-assisted laser desorption/ionization
MES	2-(*N*-morpholino)ethanesulfonic acid
MLV	Multilamellar vesicle
MS	mass spectroscopy
PC	phosphocholine
PE	phosphatidylethanolamine
p*I*	isoelectric point
PMSF	phenylmethanesulphonylfluoride
PS	phosphatidylserine
S100A11	S100 calcium binding protein A11
SANS	small angle neutron scattering
SDS-PAGE	sodium dodecyl sulfate polyacrylamide gel electrophoresis
SUV	Small unilamellar vesicle
T_m	transition temperature
Tris	trishydroxymethylaminomethane
UV/Vis	Ultraviolet-visible spectroscopy
VCAM-1	vascular cell adhesion molecule 1

Table of contents

List of Figures

List of tables

List of publications

Parts of the study have been submitted in the following articles.

1. Yusof, A. M., Hu, N.-J., Wlodawer, A. & Hofmann, A. (2005). Structural evidence for variable oligomerisation of the N-terminal domain of cyclase-associated protein (CAP).*Proteins*, 58(2):255-262

2. Hu, N.-J., Currid, M., Daley, M. & Hofmann, A. (2005). Automated CD and fluorescence data processing with ACDP and AFDP (v2.4). *Appl. Spectrosc.*, 59: 68A

3. Dabitz, N., Hu, N.-J., Yusof, A. M., Tranter, N., Winter, A., Daley, M., Zschörnig, O., Brison, A. & Hofmann, A. (2005). Structural determinants for plant annexin-membrane interactions. *Biochemistry.* 44(49):16292-300

4. Hu, N. -J., Bradshaw, J., Lauter, H., Buckingham, J., Solito, E., & Hofmann, A. (2007). Membrane-induced folding and structure of membrane-bound annexin A1 N-terminal peptides - Implications for annexin-induced membrane aggregation. *Biophys. J.* in press.

5. Hu, N. –J., Yusof, A. M., Winter, A., Osman, A., Reeve, A. K. & Hofmann, A. The crystal structure of calcium-bound annexin Gh1 from Gossypium hirsutum indicates different mechanisms of membrane binding in plant and animal annexins. (*submitted*)

1 Introduction

1.1 Structural overview of annexin

Calcium is one type of second messenger in cells and plays an important role in various signalling transduction pathways. Upon activation of membrane receptors by extracellular stimuli, second messengers trigger subsequent signalling cascades and induce cellular changes. For example, it is well known that calcium ions are released from endoplasmic reticulum (ER), after the phospholipase C product, inositol-1,4,5-trisphospate ($InsP_3$), binds to $InsP_3$ receptors in the ER (*1*). The initial increase of Ca^{2+} concentration, therefore, launches a series of functional responses. Annexins constitute a protein family whose members can bind to membranes containing anionic phospholipids in the presence of Ca^{2+} (*2-6*). Since the late 1970s and early 1980s, annexins have been widely reported in different taxonomic kingdoms. In vertebrates, the multigene family of annexins were designated annexin group A, i.e. annexins A1-A13 (abbreviated to AnxA1-AnxA13). The family of proteins has been demonstrated to be involved in membrane trafficking and reorganisation, in processes such as exocytosis, endocytosis, and phagocytosis. Moreover, several annexins, such as AnxA2, AnxA4 and AnxA6, have been shown to mediate Ca^{2+} and Cl^- channels. In addition to the intracellular functions mentioned above, numerous extracellular annexins have been found, which possess physiological roles such as anti-inflammatory ability (AnxA1), anticoagulant properties (AnxA5) and receptor activity for different extracellular ligands or small compounds (AnxA2) (*7, 8*).

Although annexins were discovered in early 1980s, it was only in 1990, when Huber and coworkers determined the first X-ray structure of an annexin family member - AnxA5 -, and it became possible to visualise the molecular arrangement of the membrane protein and

calcium ions (*9, 10*). The general shape of AnxA5 is like a curved disc, which is mainly composed of the C-terminal core, in which the N-terminal region is harboured in the concave side of the curved disc (Figure 1-1, panel a). Since then the three-dimensional structures of several annexin members have been determined: AnxA1 (*11, 12*), AnxA2 (*13*), AnxA3 (*14, 15*), AnxA4 (*16, 17*), AnxA6 (*18, 19*), AnxA8 (*20*), and AnxB12 (*21, 22*) from animals; bell pepper Anx24(Ca32) (*23*), cotton Anx(Gh1) (*24*) and *Arabidopsis* annexin (*25*) from plants; annexin C1 from fungus *Dictyostelium discoideum* (*26*); alpha-11 giardin from protozoa *Giardia lamblia (27)*. Structurally, the annexins share a topology of fourfold 70-residue repeats in the C-terminal core (repeats I to IV). Each repeat is like a helical bundle composed of five α-helices — A, B, C, D and E. Helices A, B, D and E, adopt a helix-loop-helix motif (termed as loop AB and loop DE), respectively. Helix C lies perpendicularly between the two loop motifs and connects them. Primary structure study revealed that a conserved motif, called the endonexin fold, is present in each repeat (*28*). The motif consists of the sequence of K-G-X-G-T-(38)-D/E where the bidentate acidic residues (Asp or Glu) appear in the DE loop, 38 residues further on in the endonexin sequence.

Calcium ions are coordinated by the conserved endonexin fold on the convex side of the annexin disc (*10*). To distinguish them from the canonical type I calcium binding sites (i.e. EF-hand), the two new calcium binding sites observed in AnxA5 (Figure 1-1, panels b and c) were termed as type II and type III calcium binding sites. The type II calcium binding site is provided by the endonexin sequence and found within the AB loop in each repeat where the calcium ions are coordinated by three carbonyl oxygen atoms located in the AB loop, the side chain carboxyl groups of a bidentate residue in the DE loops and one water molecule. Swairjo et al. (*29*) solved the X-ray structure of AnxA5 in the presence of calcium ions and lipid analogues. The structure of the complex not only identified the type II calcium binding site, but also provided structural evidence that the membrane-annexin interaction is mediated

by calcium ions: the calcium ions serve as bridges and are coordinated by the backbone carbonyl oxygen atoms and side-chain carboxylates of annexins, as well as by the phosphoryl oxygen atoms of the phospholipid backbone.

In contrast, in the type III calcium binding site, which is not composed of endonexin sequence, calcium ion is coordinated by two backbone carbonyl oxygen atoms, one neighbouring bidentate residue and three water molecules. Type III calcium binding sites are located in DE loop and calcium ions in the binding sites are weakly bound. It has therefore been speculated that type III binding sites may play a minor role in membrane binding (*30*). In some annexins, AB loop might harbour more than one calcium ion and provides an alternative coordination pocket, which is termed AB' site. Similar to type III binding site, AB' site also involves one or two backbone carbonyl groups and one adjacent bidentate amino acid. Two or three water molecules complete the coordination. AB' site has been observed in several annexins (*9, 12-15, 29*). Recently, the crystal structure of calcium-bound alpha-11 giardin revealed a new binding site in the DE loop, which is termed type IIIb (*27*). The calcium ions are coordinated by carbonyl oxygens of Lys53, Ile56 and side chain oxygen of Asn58 and Glu62 (monodentate). Asp126 of one monomer donates its carbonyl oxygen to complete an intermolecular coordination. Ca^{2+} ions found in annexin family are summarised in Appendix, indicating the coordination locations, numbers, types, and distances.

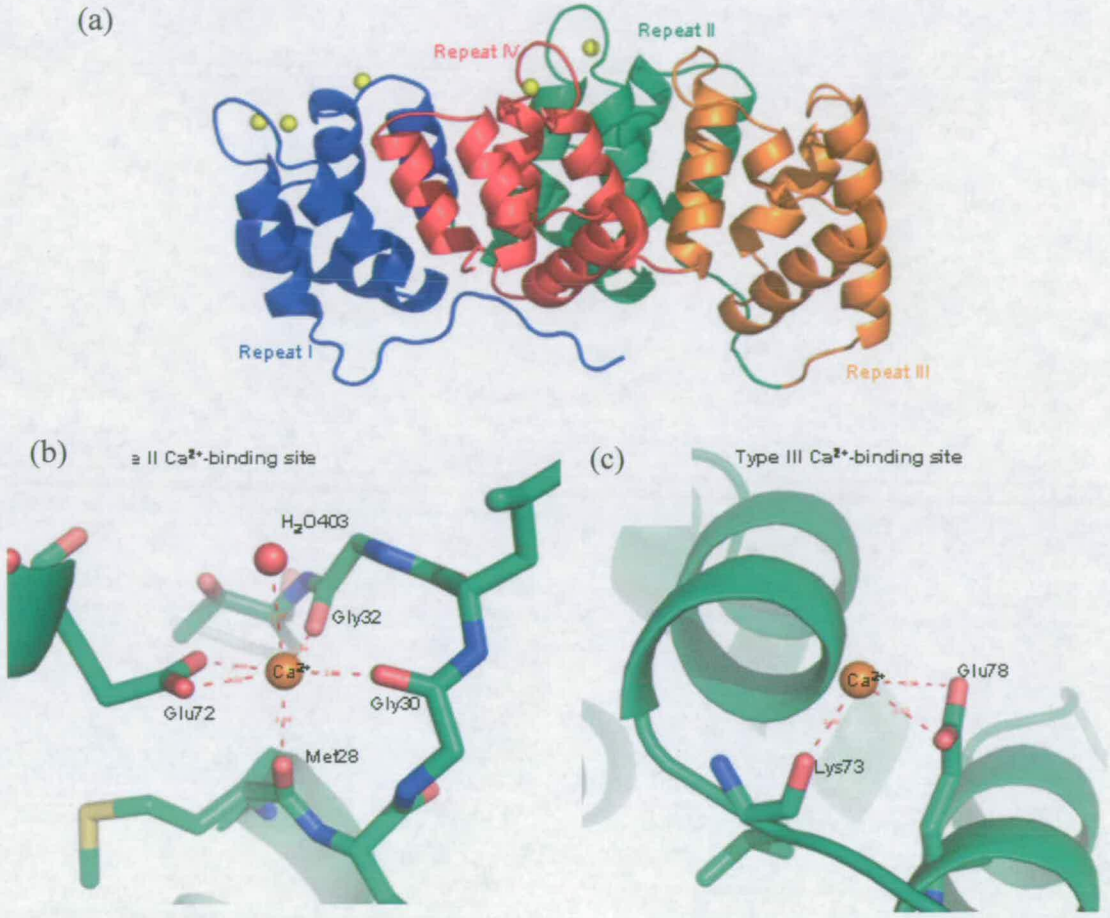

Figure 1-1 Structural model of AnxA5 and its Ca^{2+}-binding sites. (a) Ribbon diagram of AnxA5 in the presence of Ca^{2+} (PDB code: 1AVR). Repeat I is shown in blue, repeat II in green, repeat III in orange and repeat IV in red. Bound Ca^{2+} ions are illustrated in yellow spheres. (b) Type II Ca^{2+}-binding site located in the AB loop in repeat I. The Ca^{2+} ion is coordinated by three backbone carbonyl oxygens of Met28, Gly30 and Gly32, and two bidentate oxygens from Glu72, and solvent water H_2O403. (c) Type III Ca^{2+}-binding site located in the DE loop in repeat I. The Ca^{2+} ion is coordinated by the backbone carbonyl oxygen of Lys73 and two bidentate oxygens of Glu78 and several water molecules. All figures are created and rendered with PyMOL (*31*).

1.2 Biochemical properties and physiological functions of annexins

1.2.1 Membrane binding and cytoskeleton organisation

Annexins are ubiquitous in intracellular plasma. The canonical property that annexins bind to negatively charged phospholipid surfaces represents their biological functions on the cytoplasmic leaflet of membranes where acidic phospholipids are enriched. The property has led to the introduction of AnxA5 as a diagnostic tool for probing apoptotic cells which show dominant amount of phosphatidylserine on cell surface (*32*). Recently, annexins have also been reported to be involved in organisation of membrane microdomain (raft) organisation and cytoskeleton by regulating intracellular Ca^{2+}. In the sarcolemma of smooth muscle cells, AnxA2 can promote lipid raft clustering by binding to lipid raft in a Ca^{2+}-dependent manner and lead to a change in transmembrane signal transduction (*33, 34*). AnxA1, AnxA2 and AnxA8 associate with actin, indicating that annexins are directly involved in the formation of membrane cytoskeleton, which plays a vital role in cellular motility, endocytosis and cytokinesis (*35-37*). It is speculated that the membrane-bound annexins form a network on the surface of the bilayer and organise a membrane-recruitment platform for other proteins (*8*).

In addition to Ca^{2+}-dependent membrane binding, annexins also exhibit a Ca^{2+}-independent phospholipid binding activity. AnxA5 bound to phosphatidylserine (PS) vesicles at pH 4 and caused content leakage of PS vesicles at pH 5 in the absence of Ca^{2+} (*38*). Hydrophobicity assessment assays demonstrated that AnxA5 and AnxB12 might insert into the bilayer at pH 5.0 and below (*39*). The authors proposed a conformational change of these proteins at acidic pH. They cause a channel-like activity in the presence of phospholipids, implicating a role as either peripheral or transmembrane proteins. Similar findings of Ca^{2+}-independent

phospholipid binding at acidic pH were also reported on AnxA2 (*40*). The results reveal that different annexins associate with membrane by means of varying mechanisms each of which is regulated by basic biological conditions, e.g. Ca^{2+}, pH and membrane lipid content (cholesterol, glycolipid and sphingolipid).

1.2.2 Membrane aggregation and fusion mediated by several annexins

In contrast to the homologous pattern in the C-terminal core, the N-terminal domains, which are located in the concave side of annexins, vary in length and sequence in each annexin family member. The specific property of each annexin is likely to be determined by the N-terminal region. A comparison of the length of the N-terminal regions of each annexin, reveals remarkable variance — between 11 and 19 residues (annexins A3, A4, A5, A6, A10, A12, A13), 33 and 42 residues (annexins A2 and A1, respectively), and more than 100 residues (annexins A7 and A11). The annexins containing considerably longer tails have been shown to harbour binding sites for S100 proteins, e.g. AnxA1: S100A11 (*41, 42*), AnxA2: S100A10 (*43*), AnxA11: S100A6 (*44*), and different phosphorylation sites for various kinases (*11*).

Interestingly, it has been reported that AnxA1 possesses the capability to aggregate neutrophil and chromaffin cell granules (*45, 46*). Furthermore, AnxA2, AnxA4 and AnxA7 have been demonstrated to promote aggregation of phospholipid vesicles and chromaffin granule ghosts (*47-49*). It was thus hypothesised that AnxA1, AnxA2, AnxA4 and AnxA7 are likely to play a key role in endocytosis and exocytosis due to their strong vesicle-aggregating activities (*6, 50*). Among these proteins, AnxA1 is of the greatest interest due to the anti-inflammatory activity (see 1.2.3). Numerous studies of its membrane aggregation ability have been undertaken. Lee and Pollard performed a liposome aggregation assay by

measuring the turbidity of PS liposome suspension (*51*). They demonstrated liposome aggregation induced by AnxA1, but not by AnxA5. Andree and colleagues employed the chimera protein, annexin I_N-V_C (the N-terminus of AnxA1 fused to the core of AnxA5), to elucidate the aggregation ability of phospholipid vesicles (*52*). They showed that the chimera protein is able to interact simultaneously with two separate membranes. In addition, a vesicle turbidity assay of various truncated mutants of AnxA1 identified that the unique N-terminal region is involved in vesicle aggregation (*53*).

1.2.3 Anti-inflammatory response of AnxA1

Although annexins are generally intracellular proteins that localise to the cytoplasm and cytosolic organelles, AnxA1, AnxA2 and AnxA5 have also been found on the cell surface despite the lack of a secretory signal peptide (*54-56*). AnxA1 is of great pharmaceutical interest because it is upregulated by anti-inflammatory glucocorticoids and functions as a cellular mediator of glucocorticoids (*57*). It has been reported that when neutrophils adhere to the inflamed endothelium, AnxA1 is mobilised and externalised by an unknown pathway and downregulates the transmigration of neutrophils (*58*). Interestingly, both exogenously applied AnxA1 and peptides derived from the N-terminal domain of AnxA1 show an inhibitory effect on neutrophil transmigration (*59*). It has been shown that cell adhesion of leukocytes to the endothelium is mediated by a group of adhesion receptors on the surface of inflamed cells, called integrins, and Ig-like adhesion molecules expressed by endothelial cells, such as intracellular adhesion molecule 1 (ICAM-1) and vascular cell adhesion molecule 1 (VCAM-1). Externalised AnxA1 competes with the endothelial integrin counterreceptor, VCAM-1, for binding to α4 integrin (*60*). It has been demonstrated that, in several animal models, exogenously administrated AnxA1 shows anti-inflammatory activities (*61*). Thus AnxA1 possesses great pharmaceutical potential and presents an attractive candidate for anti-inflammatory drug development.

1.2.4 Plant annexins

Compared to much of the research done on animal annexins, plant annexins were not characterised until the late 1980s. It was only established that higher plant cells contain annexins in 1989 (*62*). Since then, plant annexins have been purified and studied from various plant organisms (*63, 64*). It was shown that plant annexins are abundant and ubiquitous proteins accounting for at least 0.1% of the total proteins from the plant sources studied. The purified proteins from plants revealed a Ca^{2+}-dependent binding activity to PS, similar to that found in animal annexins. Sequence comparisons indicated that the proteins are homologous to the known members of the animal annexin family. Interestingly, plant annexins appear as a doublet with similar molecular weights across all plant species, stemming from the significant separation on SDS-PAGE. For example, two proteins with a mass of 34 and 35 kDa were identified in tomato (*62*). In *Gossypium hirsutum* (cotton), two proteins with 35 and 35.5 kDa were designated as Anx(Gh1) and Anx(Gh2), respectively (65). p32 and p38 found in *Capsicum annuum* (bell pepper) were named as Anx24(Ca32) and Anx24(Ca38) (23). The variation in size is probably due to the differing length of the N-terminal domain implying the two annexins from the doublet may have a different function in plant cells compared to animal annexins.

Like annexins in animal cells, it has been speculated that plant annexins act as vital proteins in the membrane cytoskeleton. Calvert et al. demonstrated that tomato annexins, p34 and p35, bind to F-actin but not to G-actin in a Ca^{2+}-dependent manner (*66*). An I-R-I motif on the helix B in repeat III, well conserved among almost all plant annexins, has been considered to be responsible for the interaction. Surprisingly, plant annexins have been reported to have a putative peroxidase function. Gidrol et al. reported that an annexin-like protein in *Arabidopsis thaliana* restored the H_2O_2 resistant ability of the *ΔoxyR* mutant of *E. coli* (*67*). The authors proposed that the N-terminal domain of the *Arabidopsis* annexin shares some

similarity with heme binding motif of plant peroxidases. Gorecka et al. hypothesised that the conserved histidine in plant peroxidases is responsible for the oxidative stress response (*68*).

1.3 Unique structural features of AnxA1 and plant annexins

1.3.1 Conformational change of AnxA1 upon calcium-dependent binding to membrane

Although it has been suggested that the N-terminus of AnxA1 is involved in membrane aggregation, the mechanism of how the N-terminal tail binds to phospholipids remains controversial. Lee and Pollard (*51*) carried out a calcium titration experiment at pH 6 and demonstrated that AnxA1 revealed a maximum of liposome aggregation ability at the Ca^{2+} concentration of 0.5 mM. The extent of aggregation is ten-fold less at the Ca^{2+} concentration of 0.1 mM. De la Fuente and Ossa (*69*) reported that upon AnxA1 binding to phospholipids, the N-terminal tail is more solvent accessible and more easily cleaved by trypsin or cathepsin. Those observations implicate protein conformational changes upon calcium-dependent binding to the membrane and results in expulsion of the N-terminal tail to the surrounding environment. There are several models that have been suggested to explain the mechanism of membrane aggregation mediated by annexins (Figure 1-2). The first model assumes membrane aggregation is conducted simultaneously by two membrane binding sites on one annexin molecule (Figure 1-2a) (*45, 52, 70, 71*). The second model suggests that an annexin-annexin complex linked via their N-terminal tails (Figure 1-2b) or other binding partners, such as S100 proteins (Figure 1-2c), promotes aggregation of two opposite membranes (*42, 45, 70, 72*).

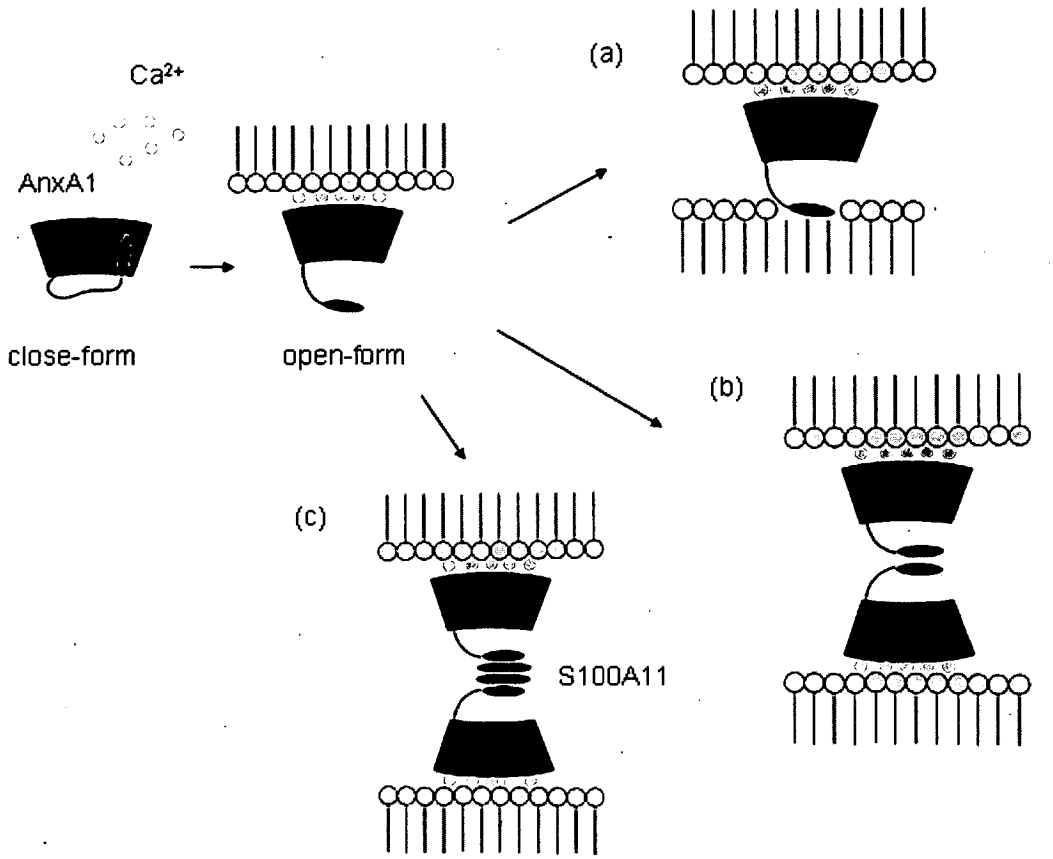

Figure 1-2 Models describing the possible mechanisms of membrane aggregation mediated by AnxA1. The N-terminal tail is inserted into the annexin core in the absence of Ca^{2+}. Upon the binding of Ca^{2+} and adhesion to a membrane, the tail is exposed, allowing its amphipathic α-helix to interact with (a) a second bilayer, or (b) another AnxA1 monomer, or (c) an S100A11 dimer and another AnxA1 monomer. (*7, 11*)

The canonical endonexin folds are conserved at the C-terminal core of AnxA1 and it is well accepted that the interaction between the convex side of AnxA1 and phospholipids is mediated by the "calcium bridge". The N-terminal tail is able to interact with phospholipids or other binding partners without the presence of calcium ions. Surface pressure measurements of the phospholipid monolayer demonstrated that AnxA1 can penetrate the monolayer and promote the increase of surface pressure in the absence of calcium ions (*73*). Under the same conditions, N-terminally truncated AnxA1 shows an attenuated effect on the

monolayer and AnxA5 is hardly able to increase the surface pressure. Bitto and colleagues (*74*) performed surface plasmon resonance (SPR) measurements and suggested that the membrane interaction with the N-terminal tail of AnxA1 is not specific for negatively charged phospholipids. X-ray crystallography and NMR experiments have shown that the N-terminal tails of both AnxA1 and AnxA2, form an amphipathic α-helix conformation (*11, 75, 76*). That conformation would facilitate the direct contact of the N-terminal tails of AnxA1 and AnxA2, with membranes, by hydrophobic interaction.

A putative mechanism has been suggested: first, AnxA1 binds to the anionic phospholipids in a calcium-dependent manner. Then, once it is membrane-bound in the presence of Ca^{2+}, AnxA1 exposes its N-terminal tail containing the amphipathic helix and interacts with the hydrophobic part of either membranes (*74*), or a binding partner, such as S100A11 (*42*). Although the model of membrane aggregation induced by AnxA1 is still elusive, it is clear that there are two independent interaction sites on each AnxA1 molecule.

Extensive efforts have been devoted to investigate the protein structure of AnxA1. In 1993, the first X-ray crystallographic structure of N-terminus truncated AnxA1 in the presence of Ca^{2+} was published (PDB code: 1AIN) (*77*). The N-terminal region was truncated for ease of protein expression and purification, producing a protein lacking the N-terminal 32 residues. The authors determined that the C-terminal core is composed of four homologous α-helix-rich domains, which resemble the structural topology of AnxA5 (*9*). Six calcium ions are located in the loop regions of helix-loop-helix motifs on the convex side of the core domain. The AB loops in the four repeats form the type II calcium-binding sites harbouring one calcium ion each. Two more calcium ions have been identified in the DE loops in repeats I and IV, which form type III calcium binding sites. Structural superposition of AnxA1 on AnxA5, revealed that the major differences were located at the AB and DE loops in repeat

III, and the AB loops in repeat I, even though the sequence alignment of the annexin family shows that the calcium-binding loops regions are highly conserved.

Rosengarth and coworkers (*11*) successfully crystallised full-length porcine AnxA1 and determined its structure in the absence of Ca^{2+} (PDB code: 1HM6) (Figure 1-3a). The authors reported that the N-terminal 26 amino acids fold into two α-helices, which tilt against each other at Glu17. Residues 2-12 adopt an amphipathic conformation. Residues 27-43 in the N-terminal tail form a random coil structure. The most remarkable difference was observed in repeat III due to the insertion of the N-terminal tail into the C-terminal core. Helix D in repeat III is displaced and unfolds as a flap covering the N-terminal tail (Figure 1-3c). The authors hypothesised that the conformation of the N-terminal tail buried in the core is an inactive form, because of the absence of calcium ions, and the unwound helix D in repeat III would refold into its original helical structure upon AnxA1 binding to the membrane. Thus, calcium ions serve as a "switch" for changing the protein structure and regulate the function of AnxA1.

In 2003, the X-ray structure of full-length AnxA1 in the presence of calcium ions (PDB code: 1MCX) was solved by Rosengarth and Luecke (*12*) (Figure 1-3b). As they had previously hypothesised, the N-terminal tail is expelled from the C-terminal core and helix D in repeat III refolds to coordinate calcium ions (Figure 1-3d). Two more Ca^{2+} ions were identified in the new Ca^{2+}-bound structure compared to the previously solved proteolytic AnxA1 structure. One is located in the AB loop of repeat II and the other is in the DE loop of repeat III. Therefore, there are two calcium ions coordinated by the AB loop of repeat II. This feature resembles the complex structure of AnxA5 and phospholipid analogs, where two Ca^{2+} ions are found in each AB loop (*29*). Unfortunately, the electron densities of residues 1-40 are not visible, although the authors claimed the protein is complete due to the evidence from mass spectrometry: the existence of a peak corresponding to the mass of full-length AnxA1. The

invisibility of those residues in the electron density map corresponding to the N-terminal domain is probably due to the high flexibility in the exposed form. As a result, the folding property and the binding behaviour of the expelled N-terminal domain are still not known.

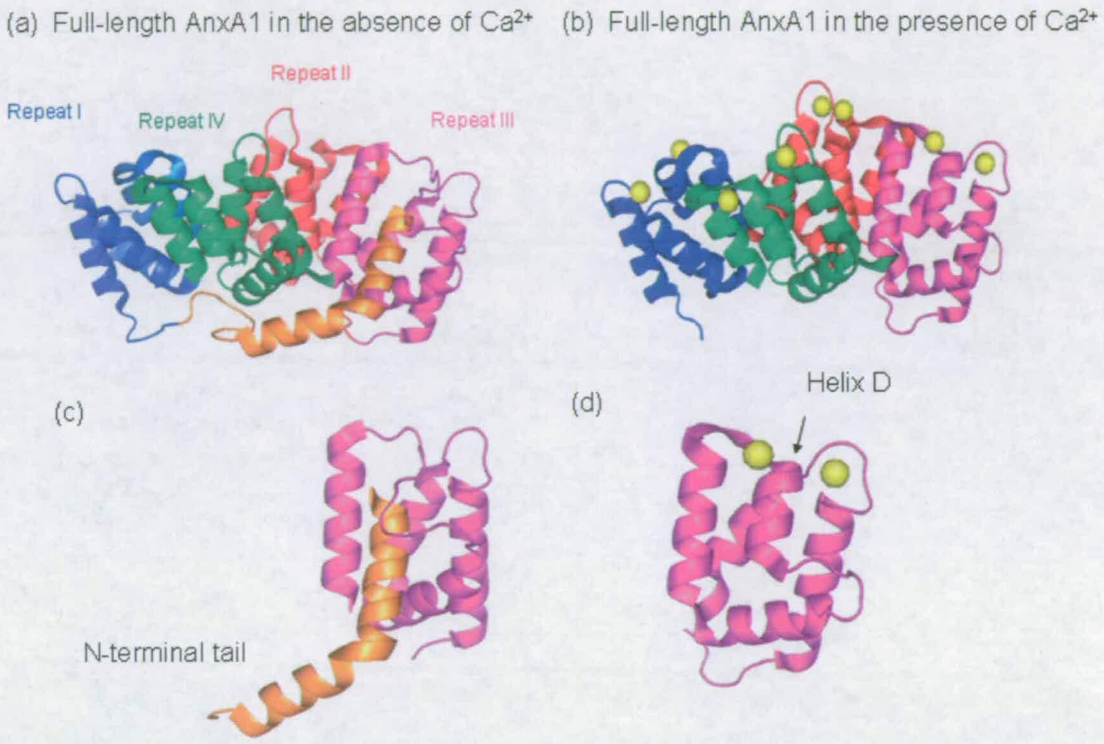

Figure 1-3 Ribbon diagrams of full-length AnxA1 (a) in the absence of Ca^{2+} (PDB code: 1HM6), and (b) in the presence of Ca^{2+} (PDB code: 1MCX). The N-terminal tail is shown in orange, repeat I in blue, repeat II in red, repeat III in magenta, and repeat IV in green. Ca^{2+} ions are represented by yellow spheres. (c) A closer view depicting the N-terminal tail inserted into the core, displacing the helix D in repeat III in the absence of Ca^{2+}. (d) Helix D is refolded in the presence of Ca^{2+} (*11, 12*). All figures are created and rendered with PyMOL (*31*).

1.3.2 Calcium-binding sites on the convex surface of plant annexins

Primary structure analysis reveals that plant annexins share a similar sequence pattern of fourfold 70-amino acid repeats. The first X-ray structure of a plant annexin, Anx24(Ca32) from *Capsicum annuum*, was identified by Hofmann et al. (PDB code: 1DK5) (*23*). In 2003, another plant annexin, Anx(Gh1) from *Gossypium hirsutum*, was also determined (PDB code: 1N00) (*24*). From the crystal structures of the two plant annexins, the authors identified several conformational features not present in the non-plant annexins.

Firstly, as known from studies of animal annexins, AB and DE loops serve as Ca^{2+}-binding sites on the convex surface of the protein. Sequence alignment of plant annexins with animal annexins revealed that the canonical Ca^{2+} binding motif composed of endonexin sequence is observed in repeat I and shows some modifications in repeat IV. Structural comparison using Ca^{2+}-bound AnxA5 as a template reveals cotton Anx(Gh1) possesses a suitable loop for Ca^{2+} coordination in repeat I. It has three carbonyl oxygens in the AB loop and two oxygens provided by the bidentate side chain in the DE loop, 38 residues further along from the AB loop (Figure 1-4a, b). The canonical calcium binding site in repeat IV is also a possibility, although the bidentate residue is sterically pointing away from the AB loop region (Figure 1-4c, d). In contrast, the loop regions in repeats II and III are not ideal for calcium coordination due to the lack of the downstream bidentate residues.

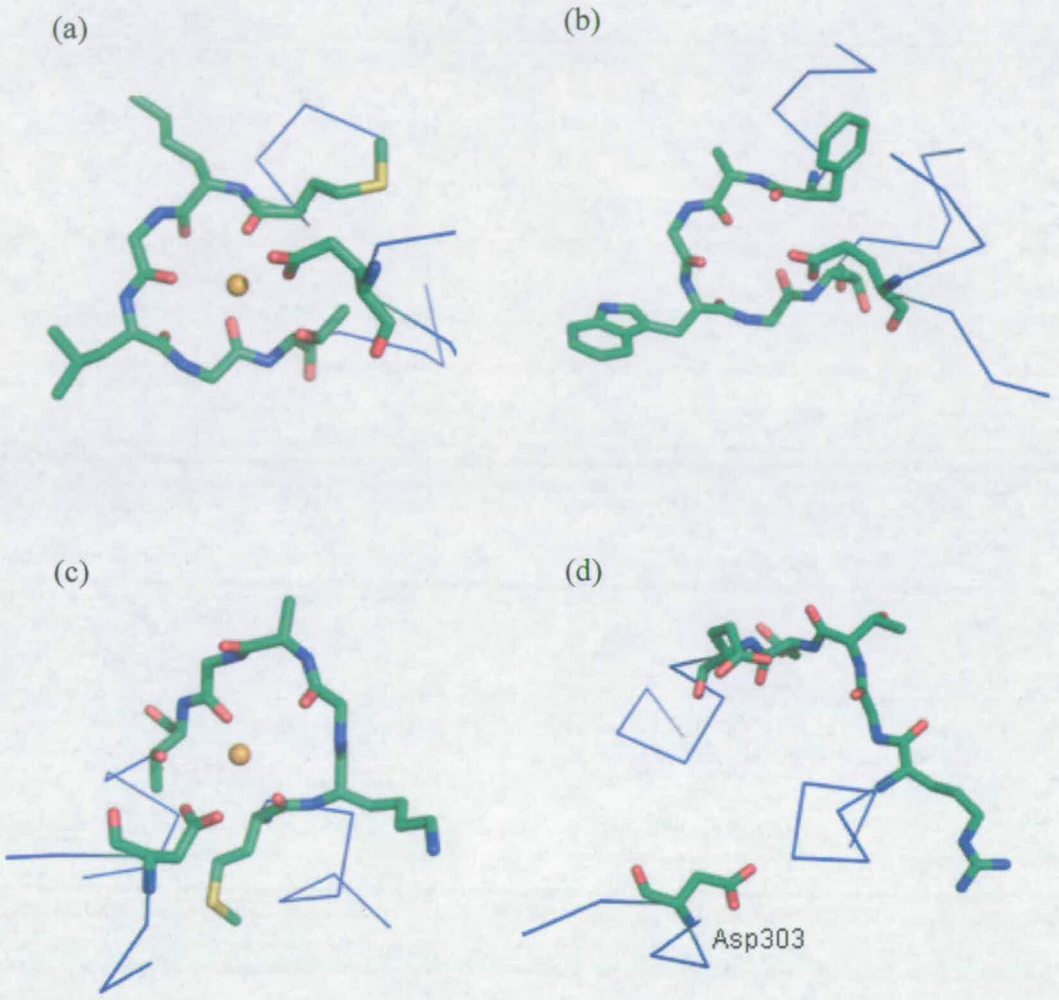

Figure 1-4 Comparison of the Ca^{2+} binding loops in AnxA5 (panels a and c) and Anx(Gh1) (panels b and d). The yellow spheres represent the Ca^{2+} ions. (a) and (b) show the IAB loop of AnxA5 and Anx(Gh1), respectively. Anx(Gh1) provides a favourable environment for Ca^{2+} coordination. (c) and (d) show the IVAB loops of AnxA5 and Anx(Gh1), respectively. The figure shows that the IVAB loop of Anx(Gh1) is distorted and the bidentate residue Asp303 is too far away for the Ca^{2+} coordination.

Secondly, a conservation of tryptophan residue in the AB loop in repeat I has been found in plant annexins. Of the two Trp35 residues in the Anx24(Ca32) dimer, one exhibited a loop-in, and the other a loop-out conformation. Anx(Gh1) was found as a monomer in each unit cell, and, superimposed on Anx24(Ca32), the Trp32 of Anx(Gh1) is located halfway between the loop-in and loop-out conformations of Anx24(Ca32) Trp35. The Trp35 in the Anx24 loop-out conformation sticks into a hydrophobic cleft provided by another non-crystallographic symmetry partner. Thus, it was suggested that the loop movement serves as a switch and is involved in the mechanism of protein self-association (*64*).

Thirdly, both annexins share conserved hydrophobic and positively charged residues extending from the convex surface (Figure 1-5a), which are not present in non-plant annexins (Figure 1-5b) (*24*). In the presence of PS/PE liposomes (regardless of whether calcium ions were supplied or not), maximal fluorescence emission reveals blue-shift in wavelength, suggesting a hydrophobic interactions between the proteins and the membranes. From the X-ray structure, the three chromophore residues, Trp35, Trp107 and Tyr192 are all located on the convex surface. Considering the fluorescence observations, it has been speculated that the aromatic residues penetrate the membrane and interact directly with the backbone of phospholipids upon membrane binding. Therefore, it has been proposed that Ca^{2+}-dependent membrane binding is mediated by the canonical endonexin folds in the first, and possibly, fourth repeats. The existence of hydrophobic and positively charged residues on the convex surface might compensate for the absence of the endonexin fold and form an alternative membrane interaction site without a requirement for Ca^{2+} ions to act as a bridge.

Plant annexins share a similar overall structure with non-plant annexins and harbour potential Ca^{2+} binding loops on the protein surface, even though they display a different membrane binding mechanism. To elucidate the coordination of Ca^{2+} provided by plant annexins, X-ray crystallographic information would provide a structural insight of the

calcium binding loops. However, there have been no successful attempts to co-crystallise plant annexins with Ca^{2+}, probably due to the positively charged residues adjacent to the Ca^{2+} binding sites, providing a repulsive force preventing binding of the cations. Thus, characterisation of the Ca^{2+}-dependent and -independent membrane interactions is crucially required to elucidate the membrane binding mechanisms and the functions of the protein family in plant kingdom.

(a)

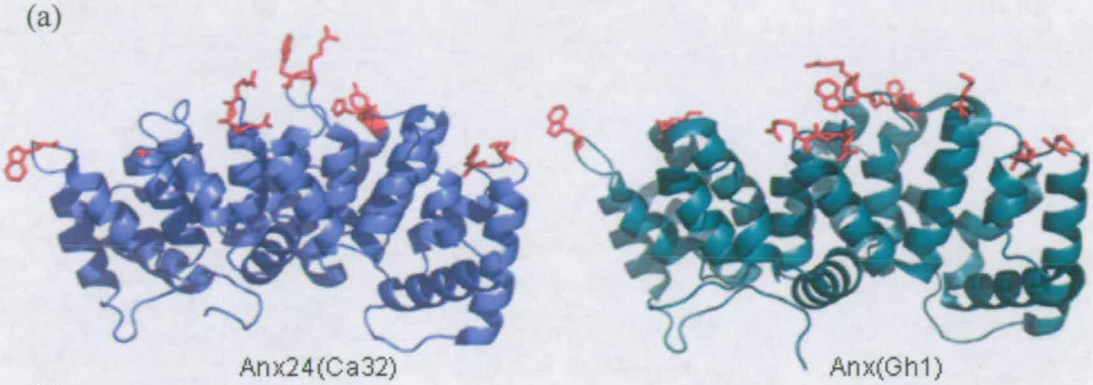

(b)

```
Cotton          ---------------------------MAHHHHATLTVPTTVPSVSEDCEQLRKAPSGWGT  34
Mallow          -------------------------------MATLTVPSTLPSVSEDCEQLRKAPSGWGT  29
Bell_pepper     ------------------------MAHHHHHHMASLTVPAHVPSAAEDCEQLRSAFKGWGT  37
Potato          ---------------------------------MASLTVPAEVPSVAEDCEQLRSAFKGWGT  29
Tobacco         ---------------------------------MASLTVPAEVPSVAEDCEQLRSAFKGWGT  29
Tomato          ---------------------------------MSSLKVPASVPDPYEDAEQLKKAFKGWGT  29
Maize           ---------------------------------MATLTVPSSVPAVAEDCEQLHKAFEGWGT  29

AnxA1           MAMVSEFLKQAWFIENEEQEYVQTVKSSKGGPGSAVSPYPTFNPSSDVAALHKAIMVKGV  60
AnxA5           ----------------------MAQVLRG-------TVTDFPGFDERADAETLRKAMKGLGT  33
                                                      *   *:.*:   *.

Cotton          LLANEATKRWTSSNQVLMEIACTRSANQLLHARQAYHARYKKSLEEDVAHHTTGDFHKLL  154
Mallow          LLANEATKRWTSSNQVIMEIACRSSSDQLLRARQAYHVRYKKSLEEDVAHHTTGDFRKLL  149
Bell_pepper     KLAKEATKRWTKSNFVLVELACTRSPKELVLAREAYHARYKKSLEEDVAYHTTGDHRKLL  157
Potato          YLAKEATKRWTKSNFVLVEIACTRSPKELVLAREAYHARNKKSLEEDVAYHTTGDHRKLL  149
Tobacco         YLAKEATKRWTKSNFVLVEIACTRSPKELVLAREAYHARYKKSLEEDVAYHTTGEHRKLL  149
Tomato          YLVNEATKRLTASNWGIMEIACTRSSDDLFKARQAYHAPYKKSLEEDVAYHTVGDFRKLL  149
Maize           VLANEEAKKSHPGGRALVEIACARTPAQLFAVKQAYHDRFKRSLEEDVAAHVTGDFRKLL  149

AnxA1           DELRAAMKGLGTDEDTLIEILASRTNKEIRDINRVYREELKRDLAKDITSDTSGDFRNAL  180
AnxA5           YELKHALKGAGTNEKVLTEIIASRTPEELRAIKQVYEEEYGSSLEDDVVGDTSGYYQRML  153
                   .   *     .   : *: .  :  ::   ...*.     .* .*:. .. * .:. *

Cotton          LPLVSSYRYEGEEVNMTLAKTEAKLLHEKISNKAYSDDD-VIRVLATRSKAQINATLNHY  213
Mallow          LPLVSSYRYEGDEVNMTLAKTEAKLLHEKISNKAYSDDD-VIRVLATRSKSQINERLNHY  208
Bell_pepper     VPLVSSYRYGGEEVDLRLAKAESKILHEKISDKAYSDDE-VIRILATRSKAQLNATLNHY  216
Potato          VPLVSSYRYGGDEVDLRLAKAESKVLHEKISDKAYSDDE-VIRILATRSKAQLNATLNHY  208
Tobacco         VALVSSYRYGGDEVDLRLAKAEAKILHEKISDKAYSDNE-VIRILATRSKAQINATLNHY  208
Tomato          VPLITAFRYEGDEVNMTLARKGSKYLHEKISDKAYHDEE-IIRIISTRSKAQLSATFNHY  208
Maize           VPLVSAYRYDGPEVNTSLAHSEAKILHEKIHKKAYSDEE-IIRILTTRSKAQLLATFNSY  208

AnxA1           LSLAKGDRSEDFGVNEDLADSDARALYEAGERRKGTDVNVFNTILTTRSYPQLRRVFQKY  240
AnxA5           VVLLQAHRDPDAGIDEAQVEQDAQALFQAGELKWGTDEEKFITIFGTRSVSHLRKVFDKY  213
                : *  . *  .  ::   .   :: *.:    :  * : .  :: *** .::   :: *

Cotton          KNEYGNDINKDLKADPKDEFLALLRSTVKCLVYPEKYFEKVLRLAINRRGTDEGALTRVV  273
Mallow          KNEYATDINKDLKADPKDEFLALLRSTVKCLVYPEKYFEKVLRLAINKRGTDEGALTRVV  268
Bell_pepper     KDEHGEDILKQLEDG--DEFVALLRATIKGLVYPEHYFVEVLRDAINRRGTEEDHLTRVI  274
Potato          KDEYGEDILKQLEDE--DEFVALLRATIKGLVYPEHYFVEVLRDAINRRGTEEDHLSRVI  266
Tobacco         KDEYEEDILKQLEEG--DEFVGLLRATIKGLVYTEHYFVEVLRDAINRRGTEEDHLTRVI  266
Tomato          HDHHGHEIIKDLEADDDDEYLKLLRAAIECLK-PREHFEKVLRLAIKKLGTDEWDLTRVV  267
Maize           KDQFTHAINKDLKADPKDEFLSTLRAIIRCFTCPDRYFEKVIRLALGGMGTDEDDLTRVV  268

AnxA1           TKYSKHDMNKVLDLELKGDIEKCLTAIVKCATSKPAFFAEKLHQAMKGVGTRHKALIRIM  300
AnxA5           MTISGFQIEETIDRETSGNLEQLLLAVVKSIRSIPAYLAETLYYAMKGAGTDDHTLIRVM  273
                      : : :.    .:    * : :.       .: : :  *:   ** .  * *::
```

Figure 1-5 Conservation of surface-exposed residues. (a) Hydrophobic and positively-charged residues (drawn in red) exposed on the convex surface of bell pepper annexin (left panel) and cotton annexin (right panel). (b) Sequence alignment showing that the exposed residues are well conserved in plant annexins but not in animal annexins, such as AnxA1 and AnxA5.

1.3.3 Oxidative stress response study of Anx(Gh1) from *Gossypium hirsutum*

The crystal structure of Anx(Gh1) has been solved by Hofmann et al. (*24*). It was shown that Anx(Gh1) possesses an unusual sulphur cluster composed of the three sulphur atoms of Met112, Cys116 and Cys243 (Figure 1-6). Although the distance between the two cysteine residues is short enough (5.5 Å) to form a disulfide bond, they are present in reduced thiolate forms. The sulphur atom of Met112, which is located at the a distance of 3.4 Å and 4.0 Å, respectively, from the sulphur atoms of Cys243 and Cys116, forms a hydrogen bond with each cysteine sulfhydryl group. The authors propose that the S_3 cluster is involved in the oxidative stress response, because oxidation of the thiol groups of the two cysteine residues can release two free electrons, which can be donated to the partially reduced oxygen species. Furthermore, the two hydrogen bonds formed by the methionine and the two cysteines, increase the RedOx potential of the two cysteines to more negative values. It has been demonstrated that cotton Anx(Gh1) colocalises with cellulose synthase (CesA) complexes (*78*), which is a transmembrane protein and plays a role in the process of glucan polymerisation. The oxidised (dimerised) form of CesA is required in the cellulose synthesis. Therefore, it is suggested that Anx(Gh1) serves as a regulatory protein to maintain CesA staying at reduced (monomerised) form and thus inhibit the synthesis of cellulose (*24*). The activity may be conducted by two possible mechanisms: (1) Anx(Gh1) reduces H_2O_2 in cytoplasm and prevents the formation of oxidised CesA, or (2) Anx(Gh1) reduces the oxidised form of CesA, and thus inhibits the synthesis process (*24*).

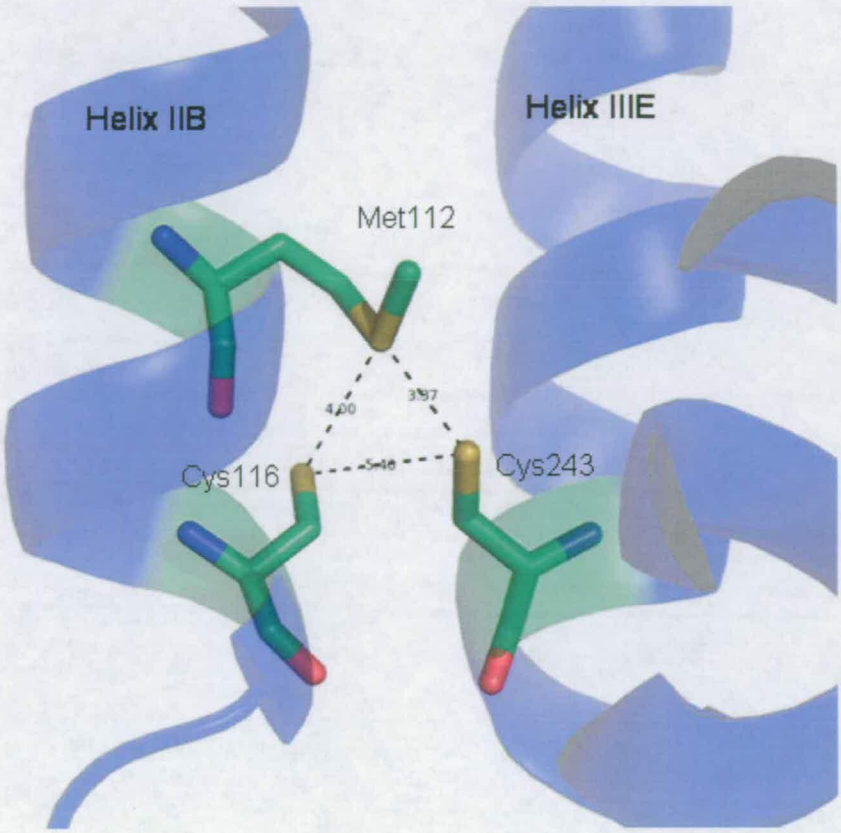

Figure 1-6 The sulphur cluster of cotton Anx(Gh1). A three-dimensional schema of the S_3 cluster composed of Met112 and Cys116 located in helix IIB and Cys243 located in helix IIIE. Distances between the sulphur atoms are given in Å.

1.4 Project aims

The overall aims of the project are to characterise the domain movement of the N-terminal tail of full-length human AnxA1, and to study membrane aggregation mediated by AnxA1. Circular dichroism (CD) spectroscopy was employed to evaluate the secondary structure content of full-length AnxA1 and the AnxA1 N-terminal peptide at varying pH and Ca^{2+} concentrations. The effects of Ca^{2+} on the domain movement of the AnxA1 N-terminus were studied by means of fluorescence emission of the single intrinsic tryptophan in the N-terminal domain. Conformational forms of AnxA1 in the presence and absence of phospholipid were also compared by adding small unilamellar vesicles in solution. The

mechanism of membrane aggregation induced by AnxA1 was elucidated by liposome turbidity measurement, liposome co-pelleting assay and measuring changes in the *d*-spacing of large multilamellar vesicles (chapter 4).

The Ca^{2+}-independent interaction of the AnxA1 N-terminus with membrane was investigated by injecting AnxA1 N-terminal peptides into a buffer covered by phospholipids monolayer and measuring the lateral surface changes caused by the peptides. Folding properties of the N-terminal peptides were characterised and compared by CD spectroscopy in the presence and absence of vesicles. The binding behaviour of the peptides was studied at the molecular level using neutron scattering diffractometry (chapter 5).

Ca^{2+}-dependent membrane binding of plant annexins was investigated and compared to that of animal annexins using phospholipid monolayer surface pressure measurements and liposome co-pelleting assay. Differential scanning calorimetry (DSC) was used as a tool to evaluate the effect of cotton Anx(Gh1) membrane binding on phospholipid packing in the presence and absence of Ca^{2+} ions (chapter 6). Ca^{2+}-binding stoichiometry of Anx(Gh1) and enthalpy changes upon Anx(Gh1) membrane-binding were quantified using isothermal titration calorimetry (ITC). Calcium binding loops on the convex surface of Anx(Gh1) were also characterised at an atomic level using X-ray crystallography (chapter 7). To understand whether Anx(Gh1) is involved in the oxidative stress response, tryptic mapping and high resolution X-ray crystallography were used to evaluate whether the two adjacent cysteine residues, Cys116 and Cys243, form an intramolecular disulfide bond after H_2O_2 treatment (chapter 8).

2 Protein expression and purification

2.1 Bacterial transformation

Human AnxA1 cDNA in pKA was kindly provided by Joannes Sri Widada. Cotton annexin cDNA His_4-Anx(Gh1) (U73746) was inserted into plasmid pRSET_6c. Bell pepper cDNA His_6-Anx24(Ca32) (E511) was inserted into plasmid pRSET_5d. Untagged plant annexin cDNAs in plasmid pRSET_6d were already available in the lab.

Bacterial transformation was conducted by mixing 0.1 μg ~ 1 μg cDNA inserted plasmid and 20 ~ 200 μl competent *E. coli* BL21(DE3) cells for 30 min incubation on ice. DNA uptake was conducted by heating the mixture at 42°C for 3 min and another 5 min on ice. 800 μl LB medium was then added and the cells incubated at 37°C for 45 min. Cells were spun down by centrifuge with 4000 rpm for 10 min at room temperature. The pellets were resuspended with 100 μl fresh LB medium followed by spreading on LB-agar plate containing 100 μg/ml ampicillin.

2.2 Protein expression

0.5 litre culture of transformed cells were grown overnight at 37°C in LB medium containing 100 μg/ml ampicillin. 25 ml of the overnight culture was used to inoculate 8 litres LB medium containing 100 μg/ml ampicillin. The inoculated medium was grown at 37 °C until the absorbance at 600 nm reached 0.6 (log phase). The medium was inoculated with 0.5 mM isopropyl-1-thio-β-D-galactopyranoside (IPTG). Another 100 μg/ml ampicillin was added and the cells were grown at 30 °C overnight. The cells were harvested by centrifugation at 5000 rpm for 20 min. The pellets were resuspended in lysis buffer containing 100 mM NaCl,

1 mM EDTA, 20 mM Tris (pH 8.0), 0.1% Triton X-100, 1 mM PMSF and 5 mM Benzamidinium chloride.

2.3 Cell lysis

The resuspended cell pellet was frozen in liquid nitrogen and thawed in 20 °C water. After 3 freeze-thaw cycles, the cell extract was subjected to 10 times of 10 sec on and off pulse ultrasonication on ice with an interval of 10 sec for each sonication. The cell lysate was centrifugated in a BECKMAN Avanti J-25 centrifuge at 23,000 rpm for 20 min. The supernatant was collected carefully without disturbing the cell pellets and another round of centrifugation was applied to reduce cell debris blockage of chromatography column for protein purification.

2.4 Protein purification

2.4.1 Human AnxA1

The supernatant separated from the cell pellets was dialysed against 20 mM Tris (pH 8.0) at 4 °C overnight. Meanwhile, Q-sepharose matrix (Amersham Biosciences) was pre-equilibrated with 20 mM Tris (pH 8.0). After an intensive wash, a linear gradient of 0.5 M NaCl over 300 ml was set up to elute the protein. AnxA1 was eluted at a concentration range of 60-80 mM NaCl.

The collected fractions were then dialysed against 10 mM Tris (pH 8.0), 100 mM NaCl, and 2 mM $CaCl_2$ overnight and applied to pre-equilibrated heparin sepharose 6 matrix (Amersham Biosciences). After a wash with equilibration buffer, the protein was eluted with elution buffer (20 mM Tris, pH 8.0, 100 mM NaCl, 4 mM EDTA).

Size exclusion chromatography was then conducted using Sephacryl S-200 HR gel-filtration column to remove impurities. Appropriate fractions were collected, pooled and concentrated with a concentrator (Vivaspin, Sartorius) followed by extensive buffer exchange with 20 mM Tris (pH 8.0), 150 mM NaCl and 0.2 mM EDTA. Protein yield and purity were examined by SDS-PAGE (*79*) and ultraviolet-visible spectroscopy (UV/Vis).

2.4.2 Cotton His_4-Anx(Gh1) and bell pepper His_6-Anx24(Ca32)

The first purification step was performed using Ni-NTA affinity chromatography. Cell extract was applied to Ni-NTA (QIAGEN) matrix and washed intensively with 20 mM Tris (pH 8.0), 100 mM NaCl and 20 mM imidazole to reduce non-specific binding. Gel-filtration was then performed by Sephacryl S-200 HR column followed by buffer exchange, and protein concentration using a Vivaspin ultrafiltration concentrator (Sartorius). Proteins were stored in 20 mM Tris (pH 8.0) and 100 mM NaCl. Protein yield and purity were examined by SDS-PAGE and UV/Vis.

2.4.3 Untagged cotton Anx(Gh1) and untagged bell pepper Anx24(Ca32)

Purification was carried out based on the reversible Ca^{2+}-dependent binding of annexins to phospholipids vesicles (*80*). After cell lysis and centrifugation, protein supernatant was applied to liposome made from soy extract in the presence of 15 mM $CaCl_2$ followed by thorough mixing with gentle stirring at 4 °C overnight. The liposome pellet was spun down using ultracentifugation at 40,000 rpm for 1 h. The protein-attached liposome pellet was resuspended and washed with buffer A containing 20 mM Tris (pH 8.0), 100 mM NaCl and 15 mM $CaCl_2$. Another 1 h ultracentrifugation was performed and liposome pellet was resuspended with buffer B containing 20 mM Tris (pH 8.0), 100 mM NaCl and 20 mM EDTA followed by 1 h ultracentrifugation. The protein should be detached from the

liposome pellet due to the Ca^{2+} chelation by EDTA. Further protein dissociation was carried out using buffer B with addition of strong chelator CHELEX (Sigma). The supernatant was carefully collected using a pipettor without disturbing the vesicle pellet.

The supernatant was dialysed against 20 mM Tris (pH 7.5) overnight and applied to a Q-sepharose matrix. A NaCl gradient of 0.5 M over 400 ml was set up and the protein was eluted at concentration range of 150-290 mM NaCl. Active elution fractions were pooled and concentrated followed by the final purification procedure of size exclusion chromatography. Protein yield and purity were monitored by SDS-PAGE and UV/Vis.

2.5 Protein concentration determination

Protein was diluted using an appropriate amount of buffer and the UV/Vis absorption scan was performed from 500 nm to 210 nm. Protein concentrations were determined using the Warburg-Christian equation (*81*):

$$[\text{Protein}] = 1.55 \times A_{280} - 0.76 \times A_{260} \text{ (mg/ml)},$$

where A_{280} is the absorption at λ = 280 nm and A_{260} is the absorption at λ = 260 nm. A dilution factor was then multiplied to obtain the original protein concentration.

2.6 Protein mass identification

Purified proteins were identified using MALDI-TOF to assess the mass of full-length protein. For further identification, proteins were digested with trypsin and the peptide masses were fingerprinted using peptide search engine Mascot (*82*). For the detailed experimental procedures, refer to chapter 3, Section 7, Matrix-assisted laser desorption/ionization (MALDI).

2.7 Results

2.7.1 Human AnxA1

The first purification step of human AnxA1 was anion-exchange chromatography. SDS-PAGE monitoring of the elution profile is shown in Figure 2-1. Human AnxA5 (35.7 kD) was used as protein marker unless otherwise specified. After this step, there were serious contaminations in fractions 5 onwards, and a significant amount of protein with a similar molecular weight of AnxA1 was still in the flowthrough (FT in Figure 2-1). As a result, the pooled fractions and flowthrough were subjected to the following purification steps respectively.

The purity of eluted AnxA1 from the heparin-sepharose column was fairly satisfactory. There was still a contamination of 70 kD (Figure 2-2, fractions 3 and 4). Interestingly, the proteins in the flowthrough of the anion-exchange step also revealed an affinity to the heparin sepharose column (data not shown), suggesting that more AnxA1 can be recovered. Since the distinct difference in size of the contaminants and the protein of interest, size-exclusion chromatography was then performed to purify AnxA1. Figure 2-3 shows that the high molecular weight proteins were separated successfully using the Sephacryl S-200 HR column gel-filtration column (elution volume 60-70 ml).

It has been previously reported that AnxA1 has an expelled and flexible N-terminal helix in the presence of Ca^{2+} (*12*). After the final purification step, AnxA1 was prone to self-truncation over several days. As shown in the mass spectrum of full-length AnxA1 (Figure 2-4a), in addition to the intact protein with mass of 38.5 kD, there was a truncated species with mass of 37.1 kD. However, exchange for the storage buffer containing 0.2 mM EDTA reduced the self-truncation of AnxA1 significantly (Figure 2-4b).

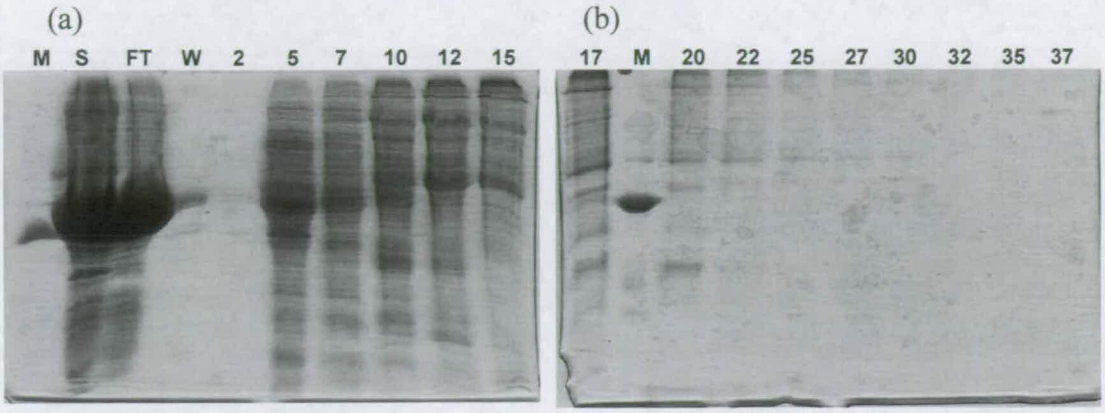

Figure 2-1 AnxA1 purification using Q-sepharose ion exchange chromatography. Eluted fractions from anion exchange column. **M**: AnxA5 (35.7 kD). **S**: crude cell extract. **FT**: flowthrough. **W**: wash. **2-37**: fraction tubes 2-37. Fractions 5-7 were pooled for following purification steps.

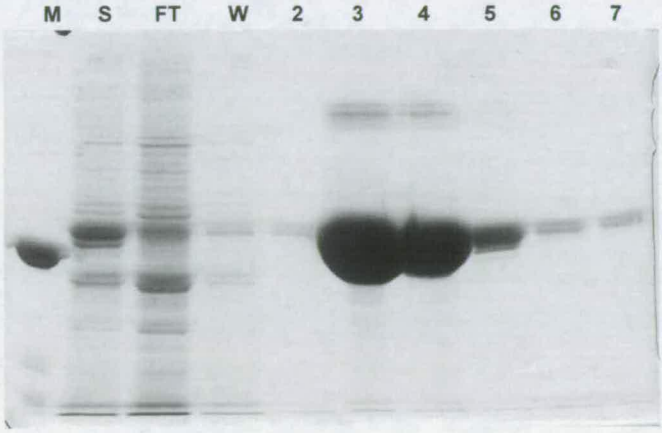

Figure 2-2 AnxA1 purification using heparin sepharose chromatography. **M**: AnxA5. **S**: pooled fractions collected from Q-sepharose ion exchange chromatography. **FT**: flowthrough. **W**: wash. **2-7**: fraction tubes 2-7. Fractions 3 and 4 were pooled for size-exclusion chromatography.

(a)

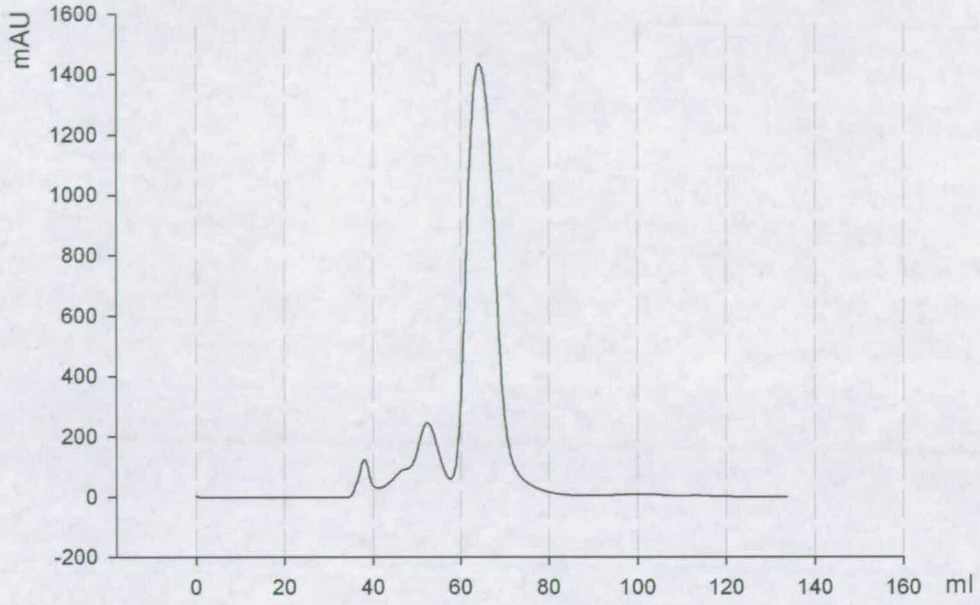

(b)

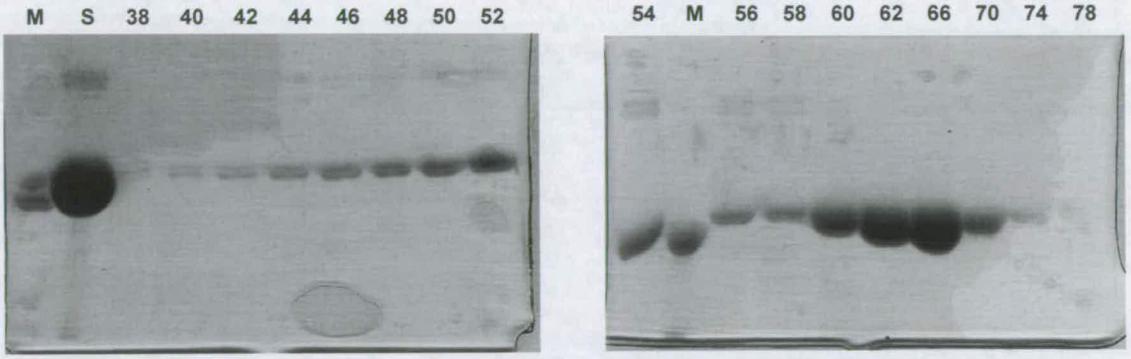

Figure 2-3 (a) Gel-filtration chromatography profile of AnxA1. (b) SDS-PAGE (12%) of active fractions. **M**: AnxA5. **S**: concentrated AnxA1 after heparin sepharose column. **38-78**: elution volumes (ml) of fractions.

(a)

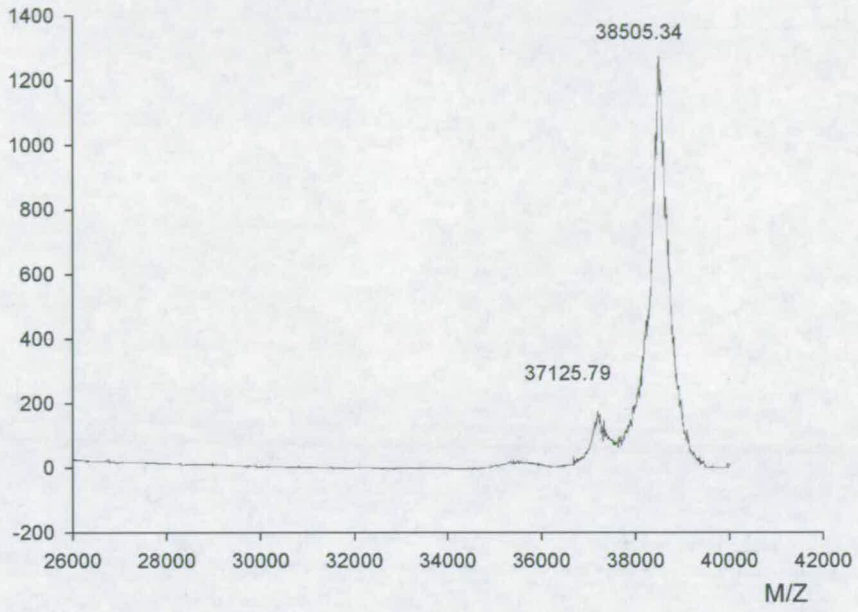

(b)

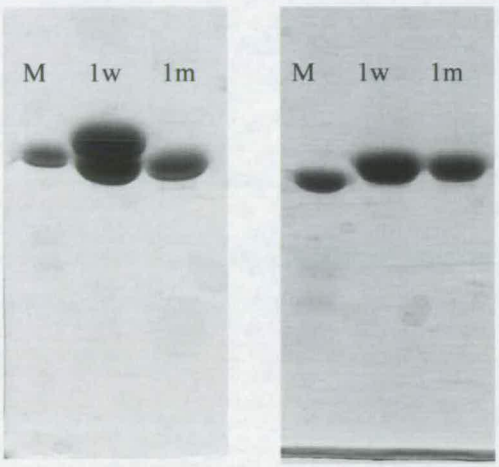

Figure 2-4 (a) Mass spectroscopy of human AnxA1 stored in the buffer containing no EDTA over one week. The numbers represent the quantified mass for each peak. (b) Left panel: AnxA1 stored in the buffer containing no EDTA over one week (1w) and four weeks (1m). Right panel: AnxA1 stored in the buffer containing 0.2 mM EDTA over one week (1w) and four weeks (1m).

2.7.2 Cotton His_4-Anx(Gh1) and bell pepper His_6-Anx24(Ca32)

After Ni-NTA affinity chromatography, most of the contaminants were separated using 20 mM imidazole, as shown in Figure 2-5 (fraction 11). His_4-Anx(Gh1) (36.5 kD) was eluted at the concentration range of 35-40 mM imidazole. However, one can observe contaminations at both high and low molecular weights. Active fractions were collected and concentrated followed by size-exclusion chromatography. The gel-filtration column completely separated His_4-Anx(Gh1) (Figure 2-6, fractions B7 - B10) from high molecular weight proteins (Figure 2-6, fractions B3 and B4) and low molecular weight proteins (Figure 2-6, fractions B12 - C1). The purification procedures also applied to the purification of His_6-Anx24(Ca32).

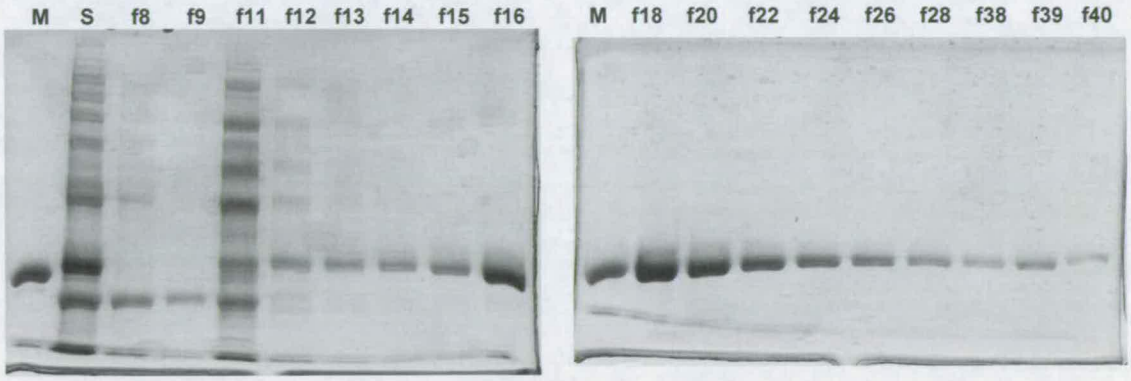

Figure 2-5 Purification of His_4-Anx(Gh1) using Ni-NTA chromatography. **M**: AnxA5. **S**: crude cell extract. **f8-f40**: fractions 8-40.

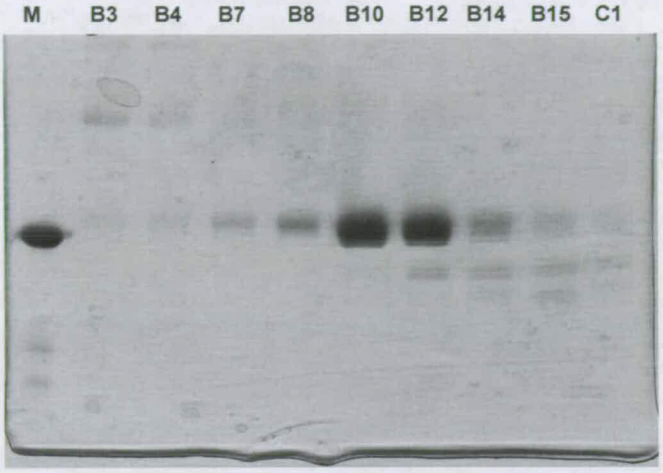

Figure 2-6 Purification of His_4-Anx(Gh1) using Sephacryl S-200 Gel-filtration chromatography. **M**: AnxA5. **B3-C1**: fractions B3-C1.

2.7.3 Untagged cotton Anx(Gh1) and untagged bell pepper Anx24(Ca32)

The purification result of untagged Anx(Gh1) is shown in Figure 2-7. In the presence of 15 mM Ca^{2+}, Anx(Gh1) was bound to liposomes tightly and no significant protein was present in the supernatant and wash. Upon adding 20 mM EDTA, Anx(Gh1) was dissociated from liposomes and protein was isolated from liposome pellet after 1 h ultracentrifugation (Figure 2-7 D1 and D2). However, in the presence of EDTA, Anx(Gh1) was still observed in the liposome pellets (Figure 2-7, P1 and P2). It was speculated that an additional hydrophobic interaction between plant annexins and phospholipid membrane may be causing this retention (*23*).

The liposome pellet became very unstable after the addition of EDTA. Although intensive ultracentrifugation was applied, it was still very difficult to remove the excess of phospholipids in the supernatant. The subsequent anion-exchange chromatography removed

the phospholipid contamination successfully. Untagged Anx(Gh1) was eluted in the range between 200 and 400 mM NaCl (Figure 2-8). The procedure also applied to the purification of untagged Anx24(Ca32).

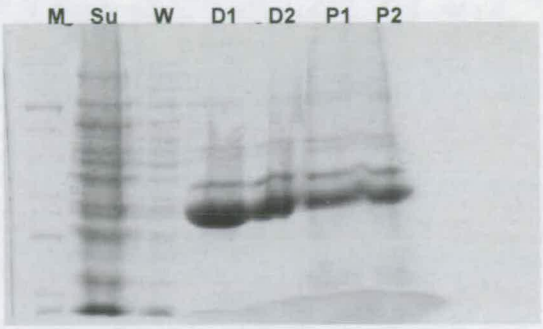

Figure 2-7 Reversible Ca^{2+}-mediated purification using liposomes. **M**: wide range protein marker. **Su**: the supernatant obtained from the first ultracentrifugation. **W**: the supernatant obtained from the second ultracentrifugation. **D1**, **D2**: the supernatants obtained after the addition of EDTA and CHELEX, respectively. **P1**, **P2**: the liposome pellets after the addition of EDTA and CHELEX, respectively.

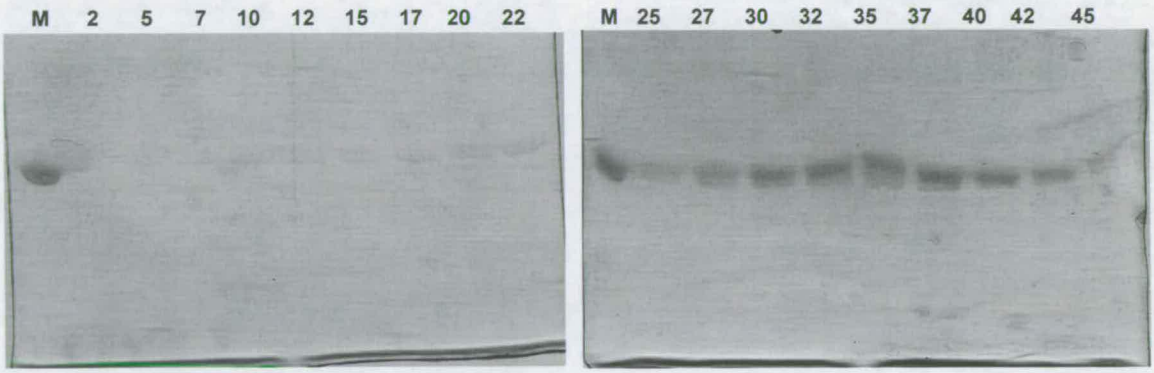

Figure 2-8 Purification of untagged Anx(Gh1) using anion-exchange chromatography. **M**: AnxA5.**2-45**: eluted fractions.

2.8 Discussion

Ion-exchange chromatography was employed to purify untagged proteins, such as human AnxA1, cotton Anx(Gh1), and bell pepper Anx24(Ca32). To achieve useful binding affinity between resin and protein, buffer pH and NaCl concentration should be selected appropriately. Since an anion-exchange column was used, the proteins must be negatively charged in solution. Therefore, the buffer pH was chosen according to the isoelectric point (p*I*) of proteins. AnxA1 has a p*I* of 6.62 and it can strongly bind to positively charged Q-sepharose resin at Tris buffer pH 8.0. AnxA1 eluted as sharp peak at NaCl concentration range of 60-80 mM. However, untagged plant annexins, Anx(Gh1) and Anx24(Ca32), have p*I* of 6.07 and 5.62, respectively. Using Tris buffer at pH 8.0 would enhance the deprotonation, and makes proteins more negatively charged. This results in a tighter affinity between proteins and resin. This strong affinity requires more NaCl molecules to compete with the positively charged resin for proteins and leads to broad elution peaks. The broad peaks caused difficulty in the following fraction collection and protein concentration steps.

The purpose to dialyse AnxA1 against 20 mM Tris containing no salt after cell lysis was to remove NaCl from the lysis buffer. Cell extract containing NaCl made poor binding of proteins to Q-sepharose resin due to the binding competition between negatively charged proteins and Cl^- anions for resin. However, AnxA1 revealed a poor stability in no salt buffer. Therefore, it is recommended to perform anion-exchange chromatography immediately after dialysis.

Ni-NTA affinity chromatography revealed excellent purification ability on His-tagged annexin proteins. However, background contaminants having a high potential to bind to Ni-NTA, thus reduce binding affinity between His-tag and nickel ions on the matrix. After applying samples to Ni-NTA affinity column, it is recommended to wash off the column

using at least 20 mM imidazole. This has improved washing off the non-specific proteins binding to the resin. One should note that the cell lysis buffer contained 1 mM EDTA. Theoretically, nickel ions would be stripped off from resin by the chelating reagents. However, cell extract containing 1 mM EDTA worked successfully in this case. If Ni-NTA column turns to a whitish colour, dialysis against the buffer containing no EDTA is recommended. The column can be recovered by the Ni^{2+} recharging procedure.

It has been reported that AnxA1 is subject to proteolytic cleavage within the N-terminal domain in cells and the cleavage was enhanced in the presence of Ca^{2+} (*83*). Truncation of the unique N-terminus of AnxA1 results in change of function and cellular distribution. The susceptibility of AnxA1 to proteolysis is regulated by different phosphorylation states of the N-terminal domain (*84, 85*). The purification results showed that AnxA1 in a buffer containing no EDTA was very liable to self-cleavage in solution probably due to the minute amount of Ca^{2+} ions in buffer. The chelation of Ca^{2+} reduced the self-truncation significantly after purification, suggesting the N-terminal domain might be at a more stable state due its firm insertion into the C-terminal core.

3 Materials and methods

3.1 Preparation of vesicles

3.1.1 Multilamellar vesicles (MLVs)

MLVs were prepared following the method of Szoka and Papahadjopoulos (*86*). Appropriate amounts of pure lipid or mixture were dissolved in chloroform/methanol (v/v 2:1) followed by evaporation using nitrogen gas stream. The dry lipid film was placed under vacuum for 12 h to remove the residual organic solvent. Appropriate aqueous buffer was then added to resuspend the dry lipid film by vigorous votexing. The solution was left for 30 min for complete hydration. Throughout the process, the temperature of the mixture was maintained above the transition temperature of the lipids.

3.1.2 Small unilamellar vesicles (SUVs)

SUVs tend to be used for spectrum measurements because they scatter less light than do large liposome particles. Dispersion of MLVs using sonication yields SUVs with diameters ranging from 15 ~ 50 nm. The procedure was modified from that of Pangano and Weinstein (*87*). Appropriate amounts of DMPC and DMPS (mol 3:1) were loaded in a round-bottom test tube and dissolved thoroughly in chloroform/methanol (v/v 2:1). A stream of nitrogen gas was applied to evaporate the organic solvent. The resulting thin lipid film was then placed in a vacuum for 12 h to eliminate residual traces of organic solvent. Aqueous buffer was then added to the test tube to a final concentration of 10 mg/ml phospholipids, and swirled by vortex at 35 °C. Lipid molecules were freed from the test tube and a milky

multilamellar vesicle solution was produced. Subsequently, bath sonication was performed to disperse the MLVs and convert them to SUVs. A nitrogen gas stream was also employed to avoid oxidative degradation of lipid caused by sonication. The temperature of sonication bath was kept at 4 °C during the whole process. The preparation of SUVs was not considered to be finished until the lipid solution adopted a clear bluish colour.

3.2 Turbidity measurements with liposomes

Turbidity of liposome suspensions has been employed to monitor the ability of AnxA1 to aggregate membrane (*51, 53, 71*). Briefly, 50 μg of AnxA1 and 0.75 mg DMPC/DMPS (molar ratio 3:1) SUV were mixed in 300 μl buffer containing 20 mM MES (pH 6.0), 100 mM NaCl and 0.2 mM EDTA. The solution mixture was loaded in a quartz cuvette with 1 cm light path. Turbidity changes were detected at wavelength of 450 nm using Perkin-Elmer spectrophotometer. Liposome aggregation was initiated by adding Ca^{2+} and the turbidity of the sample was measured at appropriate Ca^{2+} concentrations. Here, appropriate Ca^{2+} ions were added to overcome the initial 0.2 mM EDTA for the final Ca^{2+} concentrations of desire. In order to correct for the turbidity changes caused by Ca^{2+}-dependent liposome aggregation, the reading for each measurement was subtracted from liposome-only sample containing no AnxA1.

3.3 Monolayer surface pressure measurements

Kinetic studies of monolayer adsorption were carried out on a computer-controlled Langmuir film balance (NIMA) at 20 °C. The area of the Teflon trough was 300 cm^2 (30 cm × 10 cm). It was equipped with a movable barrier allowing the adjustment of the surface area of phospholipids monolayer. Subphase buffer containing 20 mM MES, 100 mM NaCl, pH 6.0 was filtered with Whatman 0.1 μm filter paper and was poured into the trough until the

surface was 2 mm higher than the trough brim (210 ml). The surface of the buffer was separated by the movable barrier into two isolated areas. For optimal circulation and mixture an extra stirrer made of Teflon, rotating at 6 rpm, was applied at the area where no phospholipids were added. The surface pressure was measured with surface potential meter using 1 × 2.3 cm^2 plates cut from filter paper (Whatman, No. 1). Lipid solution was prepared with mixture of DMPC and DMPS (mol 3:1) dissolved in chloroform/methanol (v/v 2:1) at a concentration of 1 mg/ml and 30 µl of lipid solution was applied onto the surface of subphase by Hamilton microsyringe. A lipid monolayer was spread and balanced by waiting for 20 min. The thin film was compressed by moving the barrier to generate a surface pressure of 10 mN/m, a figure that is thought to mimic the biological membrane condition (*73, 88*). After 5 min of equilibration, peptides or proteins were injected into the subphase to a final concentration of 30 nM, using a Hamilton microsyringe extending beneath the barrier. The surface pressure (mN/m) against time (sec) was recorded until no further increase of surface pressure was observed.

3.4 Copelleting assay

For elucidation of calcium-dependent membrane-binding ability of annexin proteins, a copelleting assay, based on the association between the proteins and vesicles, was performed according to previous studies (*23, 89*). The protein samples were added to DMPC/DMPS (mol 3:1) liposomes with a total lipid content of 0.2 µmole in liposome buffer containing 180 mM saccarose, 50 mM NaCl and 10 mM HEPES pH 7.5, and appropriate Ca^{2+} concentration. The mixtures were incubated for 30 min at room temperature and were subjected to centrifugation for 45 m. Liposome pellets were separated from the supernatant and resuspended with 200 µl of liposome buffer and 50 µl SDS solution (10%). For examination of AnxA1 recovery from membrane association after chelation, 300 µl of elution buffer containing 20 mM MES (pH = 6.0), 100 mM NaCl, and 10mM EDTA was added after the

45 min centrifugation. After resuspending the pellet thoroughly, the liposome suspension solution was then centrifuged again for another 45 min. The supernatant was separated carefully from liposome pellet, and both supernatant and pellet were stored at 4 °C for following electrophoresis. Liposome samples and a protein control sample were subjected to SDS-PAGE and the gel images were scanned and analysed with *ImageJ* (http://rsb.info.nih.gov/ij/) and normalised with respect to the protein control sample. The process of copelleting assay is illustrated in Figure 3-1.

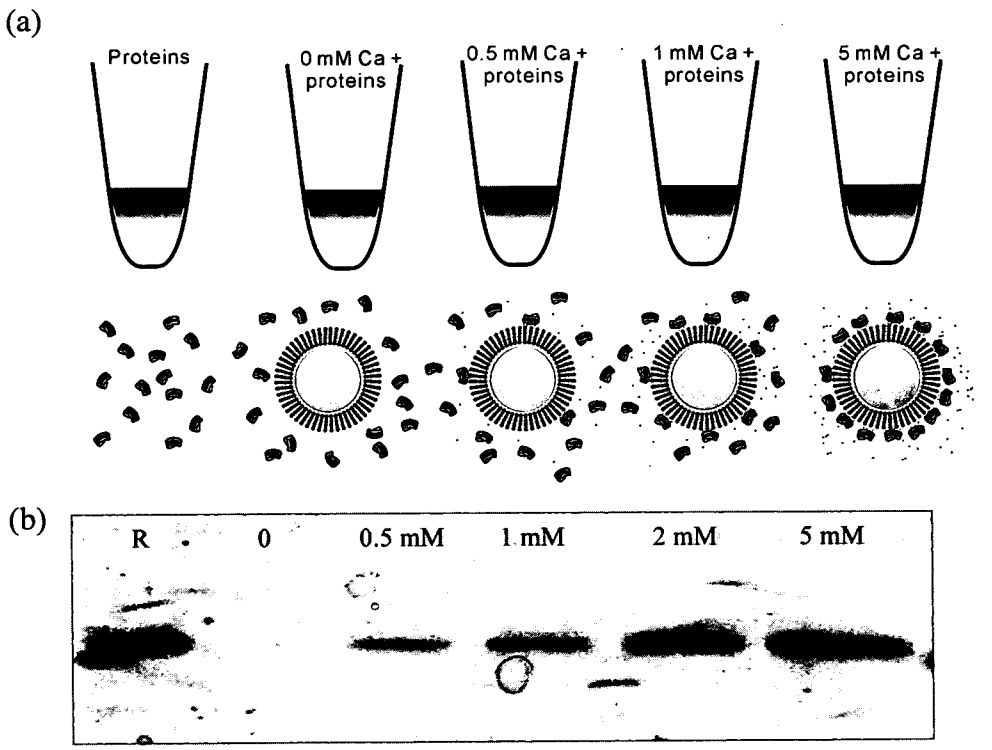

Figure 3-1 (a) Schematic presentation of copelleting assay. Annexin proteins bind the liposomes in a Ca^{2+}-dependent manner. (b) A SDS-PAGE showing the membrane-bound annexins for each Ca^{2+} concentrations. The membrane binding degree was calculated by the ratio of membrane-bound annexins to the reference band, which represents 100% of membrane binding degree.

3.5 Circular dichroism spectroscopy (CD)

Circular dichroism is the difference in absorption of left- and right-handed circularly-polarised light induced by chiral or asymmetric molecules. Biological macromolecules, such as DNA and proteins, are composed of chiral elements and thus they absorb left- and right-handed polarised lights to different extents. Recombination of the two components, after they have passed through the samples, produces elliptically polarised light. The ellipticity is designated by its angle, θ (Figure 3-2a). The difference in absorption is wavelength-dependent and yields a CD spectrum. In order to remove the effects of cuvette path length and sample concentration, one can use molar ellipticity, $[\theta] = 100 \times \theta / cl$, where c is the sample concentration, and l is the path length of cuvette.

The spectroscopic technique has been widely applied in structural biology. The CD spectrum, a plot of θ against the wavelength in the range of 190 ~ 260 nm, enables assessment of the secondary structure of a protein. The three main secondary structures of proteins, i.e. α-helix, β-sheet and random coil, produce distinct CD spectra, respectively (Figure 3-2b). One can extract the secondary information of an unknown protein using linear combinations of these reference spectra and calculate the percentage of each secondary structural component. However, like all spectroscopic techniques, the result of a CD spectroscopy measurement is an average over the entire molecular population, and it does not determine which residues are involved in the specific secondary components. Nevertheless, CD spectroscopy complements X-ray crystallography and NMR in the study of protein structure. It provides a quick means to assess the conformational stability of protein under different temperatures, pH values, buffer compositions and chemical denaturants. CD spectroscopy is also used to monitor conformational change of protein-protein and protein-ligand complexes.

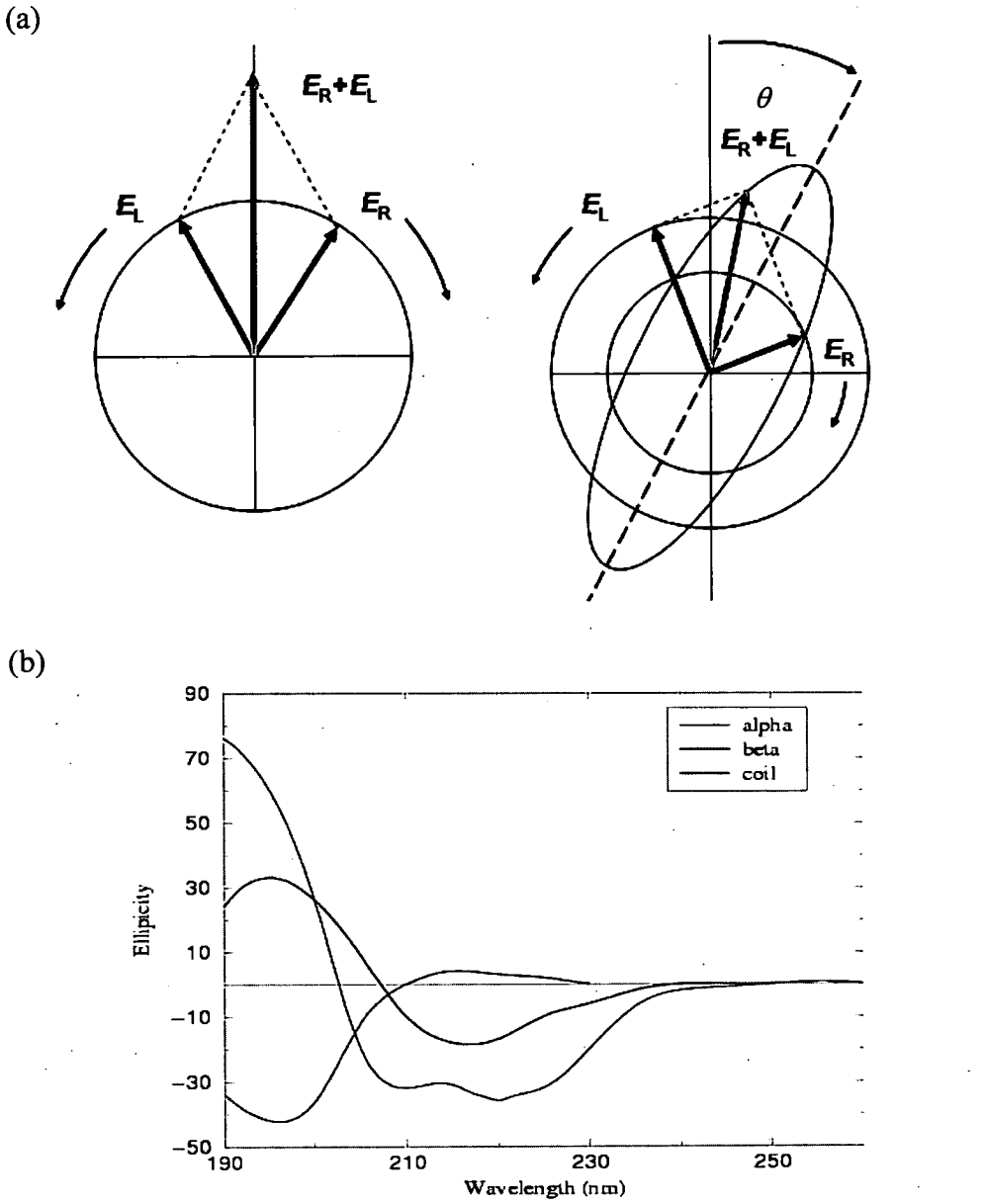

Figure 3-2 (a) The left (E_L) and right (E_R) circularly polarised components of plane polarised radiation. Left panel: the absorption of the two opposite components is the same and leads to a linear polarised line. Right panel: different absorption of the two components produces ellipticity with the ellipticity angle θ. Figures are taken from http://www.ruppweb.org/cd/cdtutorial.htm. (b) CD spectra of various secondary structure elements: α-helix (black trace); β-sheet (blue trace); random coil (green trace). The figure is taken from http://besley.chem.nottingham.ac.uk/research/research-proteincd.html.

In the present studies, the far-UV CD spectra were measured between 190 and 260 nm using Jasco-810 spectropolarimeter while the temperature was maintained at 20 °C. Concentrated samples are diluted to 0.16 - 0.08 mg/ml with 10 mM NaH_2PO_4 at appropriate pH and loaded in a 1 mm path-length cuvette. All spectra were averaged over three scans. CD spectra were measured in the presence of appropriate $CaCl_2$ concentrations (0.1 - 10 mM) at different pH values (pH = 3, 4.5, 6.2 and 7.4). To analyse the effect of membrane binding on conformational changes, sequential measurements were performed in the following procedures: (1) protein samples with addition of DMPC/DMPS (mol 3:1) SUVs (mol lipid/protein is 800:1), (2) followed by addition of 0.2 mM Ca^{2+}, and (3) addition of 1 mM EDTA.

For CD measurements of AnxA1 N-terminal peptide, the synthetic peptide powder was dissolved in 10 mM NaH_2PO_4 buffer (pH 6.2) and the concentration was adjusted to 0.08 mg/ml. 0.57 mg of DMPC/DMPS (mol 3:1) SUVs (mol lipid/peptide 100:1) was then added to monitor the conformational change of rat AnxA1 2-26 peptide. All sample spectra were corrected by subtracting blank samples containing no protein or peptide. Baseline subtraction and secondary structure prediction was carried out using the programme *ACDP* (*90, 91*).

3.6 Fluorescence spectroscopy

Fluorescence is a luminescence process in which the analyte molecules emit light triggered by the absorption of photon. The molecules at electronic excited state return to their electronic ground state and thus release the excess of energy as photon. Luminescence can be divided into three types, namely fluorescence, phosphorescence and chemiluminescence. Fluorescence and phosphorescence are very similar because both of them require the absorption of photons prior to the phenomenon. The difference is that the electronic energy transition resulting in fluorescence does not change the spin number of the molecule so the

life-time process is very short. On the contrary, phosphorescence involves a change of the spin number and shows slower emission rate. Chemiluminescence, the third type of luminescence, occurs when an excited species formed in the course of a chemical reaction emits photons in order to reach its electronic ground state.

As Figure 3-3 shows, a molecule is at a singlet state if all its electron spins are paired. When one electron of a molecule in the pair is excited to a higher energy state and the splitting electron is still paired with the ground electron, the molecule is in its excited singlet state. In contrast, if the excited electron which is unpaired, the molecules is in its triplet state. As a photon of radiation is absorbed, the energy is lifted to the excited electronic singlet state. Fluorescence occurs as a molecule returns to the electronic ground state, from the excited singlet state, by emission of a photon.

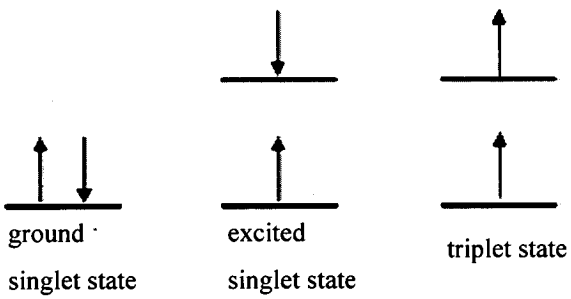

Figure 3-3 Diagram for singlet/triplet excited states.

The efficiency of a molecule with which absorbed energy produces fluorescence is expressed as quantum yield (Φ) or quantum efficiency which is the ratio of the number of luminescent molecules to the total number of excited molecules.

$$\Phi = \frac{\#\ photons\ emitted}{\#\ photons\ absorbed} \qquad \textbf{Equation 3-1}$$

The quantum yield and emission spectra are affected by the polarity of surrounding environment. After absorption of energy, the fluorophore molecule is lifted to an excited state resulting in alteration of dipole moment of the fluorophore, and thus the dipole moments of the solvent and the fluorophore molecule are unaligned. Solvent molecules assist in stabilising the energy state to a lower level by realigning the dipole moments. Therefore, the polar solvent molecules reduce the excited energy level and the loss of energy results in a shift of fluorescence emission to longer wavelength. When a fluorophore molecule is exposed to a polar solvent, one can observe the attenuation of quantum yield and red shift of emission maximum wavelength.

There are two amino acids (tryptophan and tyrosine) that can serve as intrinsic fluorophores due to their aromatic rings. The two amino acids have different absorption and emission wavelengths. The quantum yields of the three residues are also distinct. Tryptophan absorbing UV at 280 nm possesses the highest fluorescence emission intensity and quantum yield. Emission wavelength and intensity of tryptophan can be affected dramatically by solvent polarity. A protein with core buried tryptophan residues might have a red shift of 10-20 nm of emission once they are exposed to polar solvent. Tyrosine has a characteristic fluorescence profile but the fluorescence intensity is weaker. The two intrinsic fluorophores which generate different emission and excitation profiles have been used to monitor protein conformation and folding properties using fluorescence spectroscopy.

In this study, all fluorescence spectra were recorded using FluoroMax-3 (Jobin Yvon Horiba) at 20 °C. Sample concentrations were adjusted to a final concentration of 0.16 mg/ml with appropriate buffer and loaded in a quartz cuvette with 1 cm optical pathlength. Tryptophan emission was measured with excitation wavelength λ_{ex} = 295 nm. Emission spectra were monitored between 300 and 500 nm. For effect of Ca^{2+} on N-terminal domain movement of AnxA1, fluorescence spectra were collected in the presence of different concentrations of

$CaCl_2$ (0.1 ~ 10 mM) at pH 6.0 and pH 8.0. The tryptophan spectra were collected at titration of $CaCl_2$ (0.1 ~ 2 mM) in the presence of SUVs composed of DMPC/DMPS (mol 3:1). Solvent accessibility of tryptophan in the presence of vesicles was evaluated by the ratio of emission intensity at 350 nm and 380 nm ($F_{\lambda=350}/F_{\lambda=380}$). The maximum emission wavelength (λ_{max}) was determined using *PeakFit*^{TM} (AISN Software Inc.). All sample spectra were corrected with spectra of samples in the absence of protein. Baseline subtraction and peak integration was performed with the programme *AFDP* (*90, 91*).

3.7 Matrix-assisted laser desorption ionization (MALDI)

MALDI is a laser-based soft ionization method used in mass spectrometry. This technique has been applied to ionise thermolabile, non-volatile organic biomolecules such as peptides, proteins, glycoproteins, oligosaccharides, and oligonucleotides, due to its gentle ionisation process (*92*). It provides a straightforward method to check the mass of samples with excellent accuracy (up to 0.01 % error value).

The ionisation in MALDI is performed by bombardment of the analyte with a laser beam. Analytes are pre-mixed with matrix, which protects the analytes and transfers laser energy into them. The analytes are thus ionised. Matrices are crystallised compounds, among which 3,5-dimethoxy-4-hydroxycinnamic acid (sinapinic acid) is a common one for protein analysis while α-cyano-4-hydroxycinnamic acid (CHCA) is used for peptide analysis. Matrix is dissolved in solution composed of purified water, organic solvent (usually acetonitrile) and minute amount of trifluoroacetic acid. Biological analytes are then added with matrix solution and dissolved properly due to the mixture of hydrophilic and hydrophobic solvents. An aliquot of sample-matrix solution is applied onto a MALDI metal plate. As the solvent vaporises, the analytes lie homogeneously on the surface of the metal plate and form crystals with the matrix. The laser beam is fired on the matrix-analyte mixture, and the matrix

absorbs the energy and transfers it to analytes, allowing them to undergo a phase transition from solid state to gas state (Figure 3-4). Analytes are ionised by gas phase proton transfer from matrix.

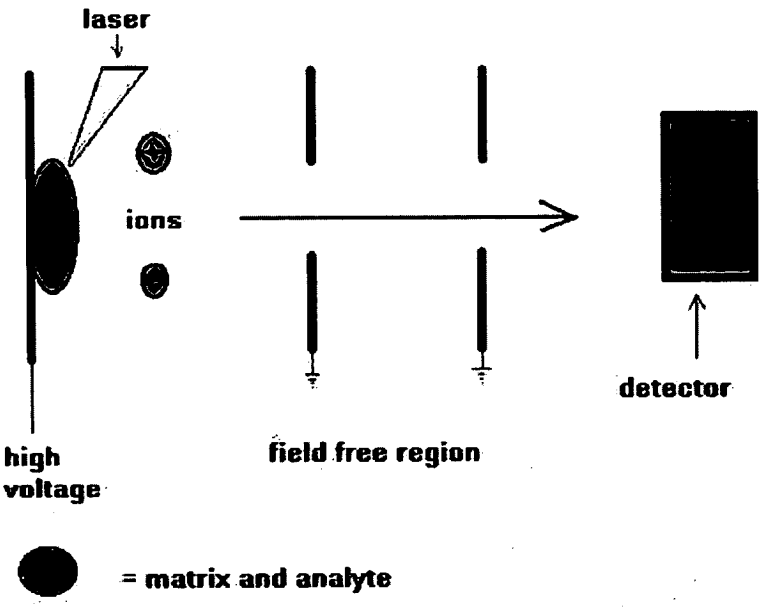

Figure 3-4 Schematic presentation of MALDI-TOF mass spectroscopy. The figure is taken from http://www.astbury.leeds.ac.uk/facil/MStut/mstutorial.htm.

The ionised analytes are usually singly-charged (+1) although multiply charged ions having +2 and +3 charges could also be present. The mass to charge ratio (m/z) for each analyte is determined using a time-of-flight (TOF) technique, in which the electric field is known. At a given detector distance, smaller ions arrive at the detector in a shorter amount of time. The time of flight t for an ion of mass m and charge z to travel this distance is proportional to $(m/z)^{1/2}$, by which one can calculate the ion's mass.

3.7.1 Full-length protein

For preparation of 10 mg/ml solution of sinapinic acid, 10 mg sinapinic acid (Sigma) was dissolved in 1 ml solvent mixture containing 400 µl water, 100 µl of 3% trifluoroacetic acid

and 500 µl acetonitrile. 0.5 µl of 2 mg/ml of AnxA1 was mixed with 0.5 µl of sinapinic acid. Each sample was spotted in duplicate on a MALDI plate. MALDI-TOF mass spectroscopy measurements were carried out using a Voyager Biospectrometry workstation (Applied Biosystems) equipped with a SCOUT ion source, operating in linear mode. Ions formed with N_2 pulse laser beam (337 nm) were accelerated to 25 kV. Protein mass peaks in the mass to charge (*m/z*) range of 5,000 to 80,000 were measured.

3.7.2 Trypsin digested peptide

3 µl of full length protein (2 mg/ml) was mixed with 27 µl of 50 mM Ammonium bicarbonate. The sample was heated for unfolding at 60°C for 30 min. Alkylation of the sulfhydryl groups of the proteins was performed by adding 1M iodoacetamide to a final concentration of 15 mM, and left in dark for 30 min at room temperature. Trypsin (Promega) was added to the protein solution at a trypsin to protein ratio (w/w) of 1:50 to 1:20. Samples were incubated at 32°C for overnight. 10 mg/ml of matrix α-cyano-4-hydroxycinnamic acid (CHCA) was prepared using the same solvent composition for sinapinic acid. Mixture of 0.5 µl of peptide solution and 0.5 µl of CHCA was applied onto a MALDI plate. Mass to charge (m/z) spectra were measured in a range of 500 to 4000. Tryptic mapping was conducted using protein identification search engine Mascot (*82*) and peptide sequence mining database MS-fit of ProteinProspector (*93*).

3.8 Differential Scanning Calorimetry (DSC)

DSC is a thermoanalytical technique to detect the difference of heat (enthalpy) required to increase the temperature of sample and reference cells. The two cells are heated or cooled uniformly and the heat is supplied or withdrawn to maintain the temperature in both cells the same. In the process of heating or cooling, the differential enthalpy is measured as a function of temperature. As the sample undergoes a physical transformation such as phase transition

in the progress of heating, more (or less) heat is required for the sample cell to maintain the same temperature as reference cell. The difference of heat flow is shown as a peak in DSC scan. An upward peak represents an endothermic process, whereas a downward peak shows an exothermic process.

There are two major types of differential scanning calorimeters in common use, heat flux DSC and power compensation DSC. In heat flux DSC, sample and reference are placed in two low-resistance alloy discs enclosed in a single furnace. The instrument measures the temperature difference upon heat capacity changes occur between sample and reference. The temperature difference is recorded to calculate differential heat flow. In power compensation DSC, sample and reference are enclosed in separated chambers with individual but identical heat sources. The temperature of sample and reference are maintained identically by adjusting heat input to the two furnaces. The difference in heat flow is a measure of enthalpy changes of sample relative to reference. DSC has been applied to study the thermal transition characterisation for polymers, purity of drugs and oxidation stability of samples. It has also been used to evaluate folding properties of proteins and molecular ordering of phospholipid bilayer.

In this study, differential heat capacity scans were performed using a PerkinElmer Pyris-1 instrument. Multilamellar vesicle solution was prepared using buffer containing 50 mM NaCl and 10 mM HEPES (pH 8.0) and the initial solution concentration was adjusted to 50 mg/ml. Appropriate amounts of His_4-Anx(Gh1) (lipid/protein mol 500:1 ~ 1000:1) or $CaCl_2$ (final concentration: 0 ~ 50 mM) were added to a final liposome concentration of 25 mg/ml. 40 µl of sample was loaded into a stainless steel capsule. Thermograms were obtained by heating from 10 °C to 90 °C with scan rate of 10 K/min. Three repetitions were

accomplished to ensure the consistency of results. Data were analysed and plotted using the programme *Pyris*^{TM} (PerkinElmer, Inc.) provided with the instrument.

3.9 Isothermal titration calorimetry (ITC)

ITC is also a thermodynamic technique, used to determine the interactions between two molecules. In biochemistry, the instrument has been used to study the ligand-binding activity of macromolecules such as DNA and proteins. The instrument contains two identical cells for sample and reference equipped with sensitive thermocouple to detect the temperature between sample and reference cells. An injection syringe with rotating propeller titrates ligand into the sample cell with known amount of aliquots, resulting in heat changes compared to reference cell. As the name implies, ITC maintains the isothermic serial titration of ligand by varying the heat input to sample cell.

For an exothermic reaction, the temperature in sample cell increases upon ligand injected leading reduction in input power to sample cell in order to maintain the constant temperature between the two cells. However, in an endothermic reaction, the temperature decreases upon ligand binding, causing increase in heat input to sample cell. ITC measures the heat flow of the serial ligand titration as a function of time in seconds. Each ligand injection causes a heat change and reveals a series of spikes (upward or downward) in the raw data. The area under the spikes is then integrated and replotted as a function of the ligand to sample molar ratio. The titration curve can be analysed using a fitting process to determine the binding constant K_a, enthalpy change ΔH, and binding stoichiometry in the reaction, allowing one to calculate ΔG and ΔS.

In order to evaluate the accuracy of ITC experiments, Wiseman et al. (*94*) proposed a parameter "*c*",

$c = nK_a[M]_t$, **Equation 3-2**

where n is the number of binding sites per macromolecule M, $[M]_t$ is the and concentration of the macromolecule in the calorimeter cell, and K_a is the association constant. It has been demonstrated that the experimental window of c is in the range of 10 ~ 500 (*94-97*). The fitting process may not be feasible for cases if $c < 10$ and definitely erroneous if $c < 1$ (*97*). For c value higher than 10, the plot of integrated heat change versus ligand molar ratio reveals a clearly sigmoid curve.

In studying the heat change upon calcium binding to Anx(Gh1), isothermal titration calorimetry measurements were performed with Microcal VP-ITC instrument (Mcirocal, LLC., Northampton, MA). The reference and sample cells were washed thoroughly with 10% Decon-90 (Decon laboratories) and rinsed with distilled water and buffer containing 20 mM Tris (pH 8.0), 100 mM NaCl. To eliminate residual Ca^{2+} ions in water and buffer, strong Ca^{2+} chelator CHELEX (Sigma) was added and then separated by using the 0.45 μm filter. All buffers were degassed before measurements. For experiments in the absence of vesicles, the sample cell was loaded with 1.4 ml of 75 μM protein, while only buffer was loaded in the reference cell. Control experiments were conducted using titration of buffer with Ca^{2+} to eliminate the enthalpy change caused by Ca^{2+} dilution. For measurements of protein-Ca^{2+} affinity in the presence of DMPC/DMPS (mol 3:1) SUVs, the sample cell was loaded with 1.4 ml of 25 μM protein and 7.5 mg/ml SUVs mixed with buffer. The reference cell contained 1.4 ml of 7.5 mg/ml SUVs and buffer. Blank measurements were also performed to evaluate the enthalpy change of the interaction of Ca^{2+} with vesicles. 5 mM $CaCl_2$ solution was injected into the sample cell with thirty times of serial titrations of 5 μl aliquots. Thirty injections were performed at 400 s intervals with stirring speed of 400 rpm. Net enthalpy change was determined by subtracting enthalpy change of experimental data from control

data. Enthalpy changes were analysed and plotted against Ca^{2+} to protein ratio using the *Origin 5.0* software (MicroCal, LLC).

3.10 Neutron diffraction

3.10.1 Sample preparation and data collection

Multibilayers of phospholipids and peptides were prepared following a published protocol (*98, 99*). 20 mg of DMPC/DMPS mixture (mol 3:1) were co-dissolved with 1% (mol) peptide AnxA1 2-26 in chloroform:methanol (v/v 2:1) and airbrushed onto quartz microscope slides using nitrogen as the propellant. For sample preparation containing full-length protein, 20 mg of DMPC/DMPS (mol 3:1) SUVs were mixed with a lipid:protein molar ratio = 800:1, in 1 ml of buffer containing 1 mM MES (pH 6.0), 5 mM NaCl and 7 mM Ca^{2+}. The procedure requires some patience and care, since aqueous buffer is less volatile than organic solvents. The slides were placed under vacuum for 12 h to remove the excess solvent, followed by rehydration in sealed sample cans for 12 h at 30 °C to achieve full equilibration. The sample cans contained saturated solutions of KCl, K_2NO_3, or K_2SO_4 in $^2H_2O/H_2O$ mixtures to maintain a relative humidity at 85%, 92% or 97%, respectively (*99, 100*). The ^2H_2O concentration was set to 8% (v/v) in the presence of each of the three salts, and set to 50% (v/v) in the presence of saturated K_2NO_3 alone. Diffraction data sets, consisting of five diffraction orders, were collected for each of the four conditions, using membrane diffractometer instruments at V1 at the Berlin NeutronScattering Center, Hahn-Meitner-Institut, Berlin, Germany. For diffraction experiments performed at D16 at the Institut Laue-Langevin, Grenoble, France, the relative humidity was adjusted by changing the temperature of the water bath. Relative humidities were set at 85%, 90% or 95%. The scanning protocol consisted of θ - 2θ scans at ± 2° around the predicted Bragg angle of the first five diffraction orders.

3.10.2 Data analysis

The diffraction intensity was obtained from the detector counts, corrected for pixel response, and each set of frames was then collapsed into a linear spectrum for each scan using the V1 instrument software *CARESS* (*101*), and the D16 instrument software *LAMP* (*102*). Baseline correction and peak-fitting, using the Lorentz function, were performed using *PeakFit*™ (AISN Software Inc.). The diffraction angles and intensities determined by the peak fitting were then transferred to *Excel* (Microsoft Corporation) spreadsheets for geometric correction. The data collected at 8% ^2H_2O were combined to construct continuous transform functions, from which sets of structure factors were read, for use in the calculation of neutron scattering density maps. Each map, representing a one-dimensional bilayer profile, was constructed using Fourier summation, in which the diffraction data in each order contribute a frequency cosine function. The square-roots of the intensities were taken to produce the structure factor amplitudes. The phase angle of the structure factors was determined on the basis of the three sets of 8% ^2H_2O data, corresponding to three different *d*-repeat spaces. The phase angles for each diffraction order were adjusted to allow the observed points of three data sets to fit a continuous transformation, using a least-squares minimisation procedure (*98*). Water profiles of the stacked bilayer systems were calculated by subtracting the scattering profile at 8% ^2H_2O from the profile at 50% ^2H_2O. Scaling of data sets to each other was performed using an absolute scale based on the neutron scattering lengths of known component molecules, i.e. phospholipids.

3.11 Small angle neutron scattering

3.11.1 Sample preparation and data collection

20 mg of a mixture of DMPC/DMPS (mol 3:1) or ^{2}H54-DMPC/DMPS (mol 3:1) was mixed with chloroform:methanol (v/v 2:1) in 10 ml tubes. Nitrogen stream gas was applied to

evaporate any residual traces of organic solvent. The thin film was dried under vacuum for 12 hours and then hydrated with ^2H_2O or ^1H_2O buffer containing 20 mM Tris (pH 8.0), 100 mM NaCl. 2 mM Ca^{2+} was added if full-length AnxA1 was present. 0.2 % (mol) of full-length AnxA1 or AnxA1 2-26 peptide was then added to the mixtures, up to a total volume of 1 ml, followed by vortexing for a few minutes and allowed to equilibrate in a waterbath at 35°C. The procedure produced protein/peptide-containing multilamellar vesicles (MLVs). The lipid/protein or lipid/peptide mixtures were ready for small angle neutron scattering (SANS) measurement.

The SANS measurements were performed in the instrument LOQ at ISIS, CCLRC Rutherford Appleton Laboratory, UK. The protein and vesicle mixture solutions were placed in 4 mm path-length quartz cuvettes for 1 h under ambient conditions, before measurements were taken. The measurements were made using the white beam time-of-flight method, in a scattering vector, Q, range of 0.007-0.287 $Å^{-1}$.

3.11.2 Data analysis

The scattering data were corrected for background scattering, detector response, and the spectral distribution of the incident neutron beam to obtain an absolute scattering cross-section (I(Q) in cm^{-1}), by the instrument software, *COLETTE* . The scattering profiles were plotted as the function of the scattering vector Q against scattering intensity I(Q), where Q is defined as

$$Q = 4\pi sin\theta/\lambda, \qquad \textbf{Equation 3-3}$$

where 2θ is the scattering angle, and λ is the neutron wavelength. As MLVs form a lattice-like conformation, the Bragg diffraction peak is notable from the SANS profiles (*103*). Therefore, Q can be written as $Q = 2\pi/d$, according to Bragg's law, $n\lambda = 2d\sin\theta$, where d is

the repeating space of two adjacent phospholipid lamellae. The Bragg peaks were positioned quantitatively using *PeakFit*™ (AISN Software Inc.).

4 Characterisation of human AnxA1 and N-terminal peptides

4.1 Introduction

Trp12 is the unique tryptophan residue harboured in the N-terminal tail of AnxA1. Therefore, numerous experiments using fluorescence spectroscopy have been performed to study the conformational changes of the N-terminal domain of AnxA1 at different Ca^{2+} concentrations (*42, 104, 105*). Porte et al. (*104*) reported that a high concentration of Ca^{2+} (10 mM) results in red-shift of maximum emission wavelength and decrease of emission intensity compared to low concentration of Ca^{2+} (10 μM) or without Ca^{2+}. The authors suggested that in the condition of low concentration of Ca^{2+} or no Ca^{2+}, the Trp12 is buried in the core domain and less accessible to solvent. This corresponds well with the Ca^{2+}-free X-ray structure of AnxA1, which shows the N-terminal domain is inserted into the C-terminal core (*11*).

Fluorescence emission of Trp12 was also used to investigate the interaction with phospholipids. Meers (*105*) demonstrated that the intensity of tryptophan fluorescence increases upon addition of phospholipid vesicles and 100 μM Ca^{2+}, but the peak shifts to a longer wavelength. In addition, membrane-bound spin-labels at various depth of bilayer did not quench the fluorescence intensity of Trp12, suggesting the tryptophan residue is not involved in the hydrophobic interaction with the phospholipid vesicles. However, as the author described, they added very low concentration of Ca^{2+} (100 μM) to avoid vesicle aggregation. Therefore, the protein conformation at the Ca^{2+} concentration cannot reflect its active status. Seemann et al. (*42*) observed the interaction between the N-terminal 13 amino acids of AnxA1 and S100A11, which is a member of EF-hand Ca^{2+}-binding protein family.

The fluorescence emission spectrum indicated that the tryptophan residue has a hydrophobic interaction with S100A11. The complex structure of S100A11 with the AnxA1 N-terminal peptide composed of the first 14 residues shows that the peptide adopts an amphipathic α-helical structure (*106*). The hydrophobic residues of peptide contact with the C-terminal helix of S100A11.

It is known that AnxA1 mediates membrane aggregation in the presence of calcium. However, the mechanism is still not well understood. The X-ray structure of AnxA1 shows that the amphipathic α-helix in the N-terminal domain is expelled when Ca^{2+} is coordinated at the primary membrane binding site on its convex surface (*12*). Furthermore, it has been demonstrated that membrane-bound AnxA1 via its primary membrane-binding site possesses a secondary membrane binding ability (*74*). Interestingly, the secondary binding shows a Ca^{2+}-independent interactions with membrane. According to the observations, the most possible scenario of membrane aggregation is that the C-terminal core of AnxA1 serves as the primary membrane binding site in the presence of Ca^{2+}. The exposed N-terminal domain binds to second membrane via a hydrophobic interaction.

The study aims to investigate the secondary membrane-binding ability of the AnxA1 N-terminal domain. Various biophysical experiments have been used to assess the conformational changes at different pH values and calcium concentrations. Additionally, domain movement of the AnxA1 N-terminal tail was monitored at the membrane-aggregated state. The mechanism of membrane aggregation induced by AnxA1 was investigated using liposome-based turbidity assay. The work characterising the membrane binding activities of AnxA1 N-terminal peptides has been published (*107*).

4.2 Results

4.2.1 Lateral surface pressure measurement

Previous studies showed that AnxA1 can penetrate the phospholipid monolayer in the absence of Ca^{2+} under acidic conditions (*73*). It has been assumed the Ca^{2+}-independent membrane interaction is caused by the N-terminal domain. Langmuir phospholipid monolayer was employed to monitor the penetration kinetics of AnxA1 N-terminal peptides in the absence of Ca^{2+}. The surface pressure of DMPC/DMPS monolayers (mol 3:1) after injection of proteins (human AnxA1, AnxA5 and chimeric $AnxA1_N$-$A5_C$) and AnxA1 N-terminal peptides (rat AnxA1 1-50 S27A, S45A and rat AnxA1 2-26) were recorded as a function of time (Figure 4-1a). As the traces show, full-length human AnxA1 induced a dramatic surface pressure increase of 3 mN/m in the initial 200 s. Chimera annexin $AnxA1_N$-$A5_C$ also mediated an increase in surface pressure (approx. 2 mN/m), although to a lesser extent than human AnxA1. As expected, human AnxA5 lacking the functional domain in its N-terminus showed no increase in surface pressure. Generally, increases in surface pressure of lipid monolayer have been interpreted as a penetration of protein molecules into the membrane (*108*). Rosengarth et al. have shown that the Ca^{2+}-independent interaction of AnxA1 with monolayer is due to the N-terminal domain based on hydrophobic interactions regardless of the charge nature of headgroup of phospholipid (*73*). The increase in surface pressure induced by chimeric $AnxA1_N$-$A5_C$ provides evidence that the N-terminus plays a regulatory role in monolayer penetration. It also proves that the core has no specific role in this particular model of binding. However, the AnxA5 C-terminal conformation may change the functional behaviour of AnxA1 N-terminal tail and attenuate the penetration interaction.

In order to validate the function of N-terminal domain in monolayer penetration, several rat AnxA1 N-terminal peptides were used to examine if the peptides can mediate surface

pressure increase in the absence of Ca^{2+} (Figure 4-1b). Rat AnxA1 N-terminal 1-50 S27A and S45A peptides revealed a similar level of surface pressure increase compared to full-length human AnxA1 (about 2 – 3 mN/m). Rat AnxA1 2-26 peptide also revealed a Ca^{2+}-independent interaction with phospholipid monolayer albeit the pressure increase is less intense than with the other two mutant peptides.

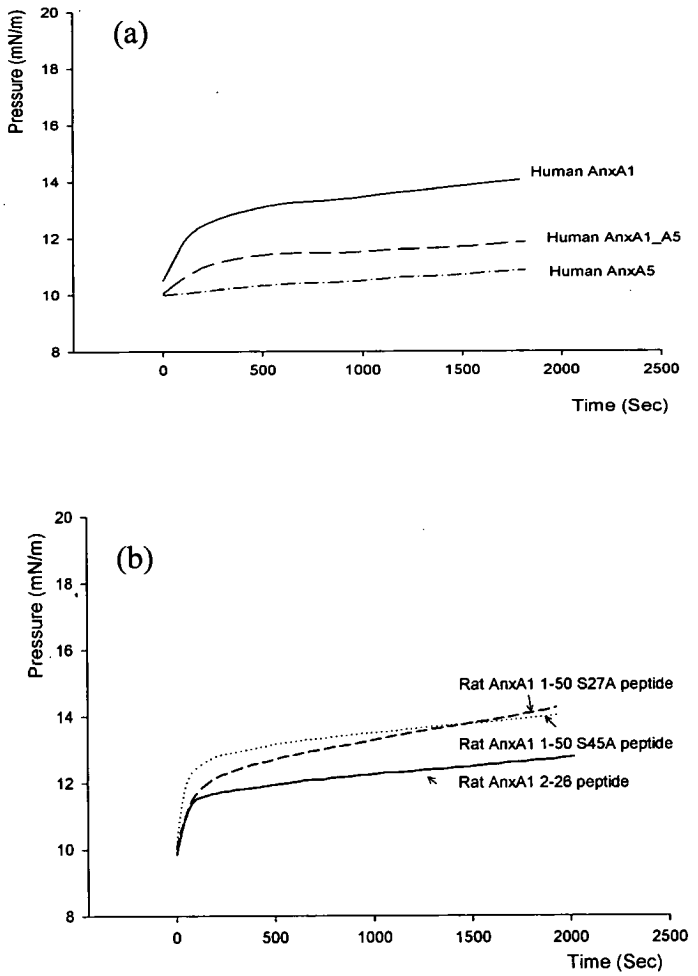

Figure 4-1 Phospholipid monolayer surface pressure measurements after injection of (a) full-length human annexin proteins: AnxA1, AnxA5 and chimera protein AnxA1_A5 and (b) rat AnxA1 N-terminal peptides AnxA1 1-50 S27A, AnxA1 1-50 S45A and AnxA1 2-26 in the absence of Ca^{2+}. All the traces have been subtracted by the baselines collected without any injection of peptides or proteins.

4.2.2 CD spectroscopy

4.2.2.1 Full-length human AnxA1

Different concentrations of Ca^{2+} and pH values did not cause significant changes in CD spectra of AnxA1 (data not shown). However, the subtle differences in secondary structure can be monitored by the two minimal peaks at 208 nm and 222 nm. The ratio between molar ellipticities at 222 nm and 208 nm ($[\theta]_{222}/[\theta]_{208}$) is greater than 1 for an α-helix (*109*). The ratio has been used to assess the folding properties of AnxA11 and AnxA13 (*110, 111*). Herein, the $[\theta]_{222}/[\theta]_{208}$ ratio of each spectrum is plotted against different Ca^{2+} concentrations and pH values (Figure 4-2). The plots reveal the ratio remain unchanged during serial Ca^{2+} titration, despite an unusually high value observed at 5 mM Ca^{2+}, pH 7.4 (Figure 4-2a). This suggests that AnxA1 maintains constant secondary structure components at different Ca^{2+} concentrations. Interestingly, plotting the ratio values against pH, the ratios show an ascendant tendency as pH value increases although the changes are not significant (approx. 5 %) (Figure 4-2b). The results indicate that the folding of AnxA1 in the absence of vesicles remains unchanged at different Ca^{2+} and pH conditions.

CD spectra of full-length AnxA1 were also compared in the presence and absence of vesicles at pH 6.0 (Figure 4-3). The $[\theta]_{222}/[\theta]_{208}$ ratio obtained from the CD spectrum of AnxA1 alone at pH 6.0 is 0.9857 (data not shown). Addition of SUVs did not cause significant changes in secondary structure composition ($[\theta]_{222}/[\theta]_{208}$ = 1.001). However, addition of 0.5 mM Ca^{2+} to the vesicle-containing mixture slightly altered the CD spectrum of AnxA1 ($[\theta]_{222}/[\theta]_{208}$ = 1.2739). Secondary structure prediction shows a 3% increase of α-helical structure upon Ca^{2+} addition in the presence of SUV. Interestingly, after EDTA was added to the AnxA1-Ca^{2+}-SUV mixture, the spectrum showed a similar CD profile ($[\theta]_{222}/[\theta]_{208}$ = 0.9817) to pure AnxA1.

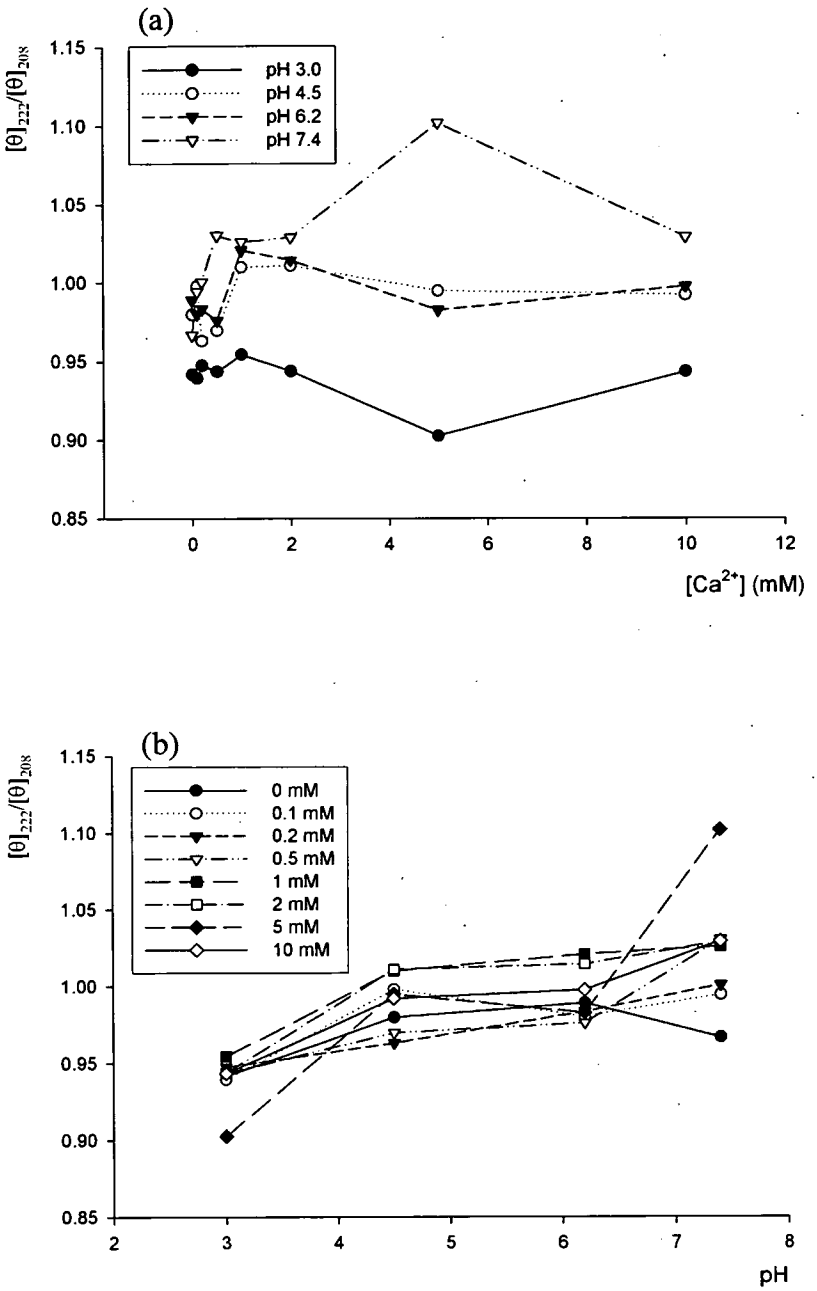

Figure 4-2 $[\theta]_{222}/[\theta]_{208}$ ratio derived from the CD spectra collected at different Ca^{2+} concentrations (0 ~10 mM) and pH values (pH 3.0, 4.5, 6.2 and 7.4). (a) $[\theta]_{222}/[\theta]_{208}$ ratio plotted against Ca^{2+} concentrations. (b) $[\theta]_{222}/[\theta]_{208}$ ratio plotted against pH values.

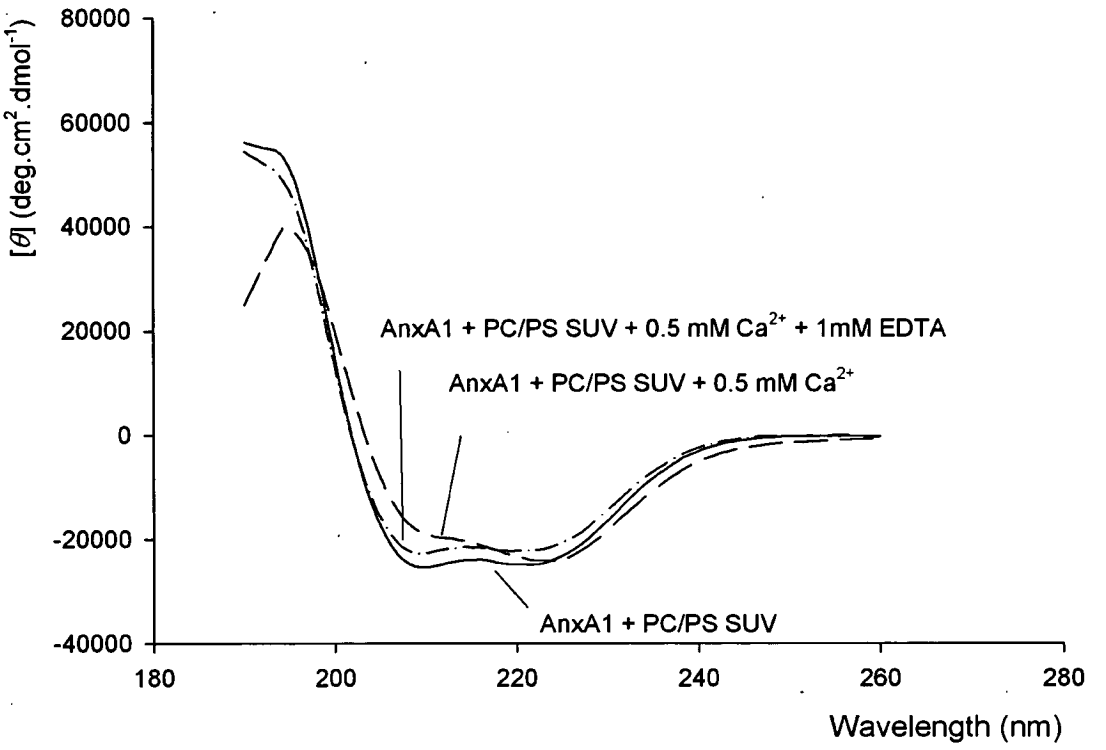

Figure 4-3 CD spectra of full-length human AnxA1 in the presence of DMPC/DMPS (mol 3:1) SUVs, in the absence of Ca^{2+} (solid line), in the presence of 0.5 mM Ca^{2+} (dashed line), and in the presence of 0.5 mM Ca^{2+} followed by addition of 1 mM EDTA (dashed-dotted line)

4.2.2.2 Rat AnxA1 N-terminal peptide

The X-ray structure of human AnxA1 in the absence of Ca^{2+} has shown the folding of the N-terminal domain is α-helical and it inserts into the core domain (*11*). The amphipathic helix conformation also suggests a direct interaction of the N-terminal domain with membrane. However, in the Ca^{2+}-bound AnxA1 structure, the N-terminal domain is not visible due to its flexibility (*12*). Surface pressure balance experiments in 4.2.1 reveal that AnxA1 N-terminal peptides have the ability to interact with phospholipid monolayer in the absence of Ca^{2+}, suggesting the peptides have a special folding, which is suitable for direct interactions with membrane (Figure 4-1). To investigate the folding of the N-terminal domain of AnxA1 in the

presence of vesicles, the secondary structure of rat AnxA1 2-26 peptide were compared with/without DMPC/DMPS SUVs (mol 3:1) at 20 °C using CD spectroscopy (Figure 4-4).

In aqueous buffer, the CD spectrum of rat AnxA1 2-26 showed a strong negative peak at 200 nm indicating a predominantly random-coil conformation. However, in the presence of SUVs, the CD spectrum revealed a positive peak at 190 nm and two minima at 208 and 222 nm. Secondary structure prediction indicates an 11% increase in α-helix structure. The conformational changes of AnxA1 2-26 peptide show that the vesicles help in the formation of a helical structure of the peptide. This helical structure is more favourable in hydrophobic interactions with membranes.

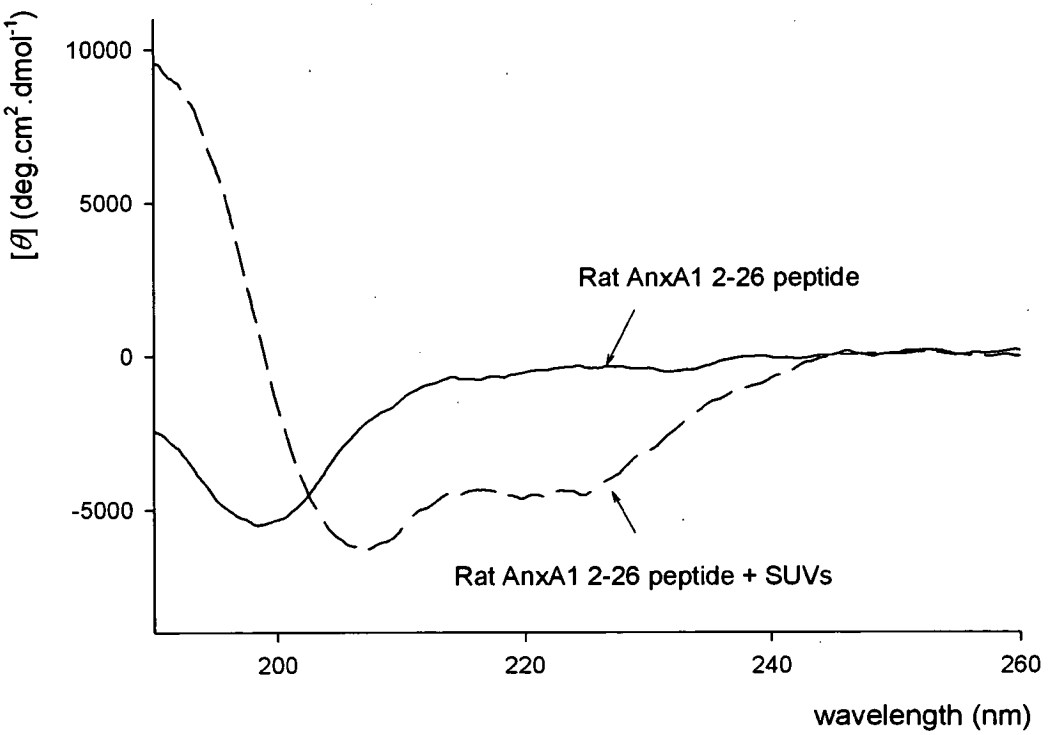

Figure 4-4 CD spectra of rat AnxA1 2-26 N-terminal peptides in the absence (solid line) and presence (dashed line) of DMPC/DMPS (mol 3:1) SUVs.

4.2.3 Fluorescence emission measurements of human AnxA1

Fluorescence emission spectra of AnxA1 with excitation wavelength of 295 nm were collected in a series of Ca^{2+} titrations at pH 6.0 and pH 8.0 (Figure 4-5a, b). The fluorescence intensity and emission maximum wavelength for each Ca^{2+} concentration were plotted in Figure 4-5c, d. A significant increase in fluorescence intensities was observed as calcium concentration increases (Figure 4-5c). In the absence of Ca^{2+}, the fluorescence emission intensity at pH 8.0 is about 80% of the intensity at pH 6.0. However, as Ca^{2+} concentration increases to 1 mM, the quantum yield differences between the two pH values start to become negligible. Interestingly, AnxA1 shows higher quantum yield at pH 6.0 in the absence of Ca^{2+} and low Ca^{2+} concentrations (up to 0.5 mM) compared to pH 8.0. A small red shift of emission maximum was detected as Ca^{2+} concentration increases (Figure 4-5d). The emission maximum wavelength is 355 nm in the absence of Ca^{2+}, and 356.5 nm in the presence of 2 mM Ca^{2+}.

In the closed form of AnxA1 crystal structure (*11*), the N-terminus is deeply inserted in the C-terminal core. Helix D in repeat III is disturbed by the inserted helix. In the adjoining region of Trp12 on the N-terminal helix, Met248 is located at the unfolded helix D in repeat III with a distance of 4 Å, and acts as a tryptophan quencher (Figure 4-6). It has been known that methionine can quench tryptophan fluorescence due to electron donation from tryptophan to methionine (*112*). The Ca^{2+}-dependent increases in quantum yield (Figure 4-5c) can be explained by the weaker quenching effect of Met248 on Trp12 upon Ca^{2+} addition. The results indicate that the N-terminal domain of AnxA1 is expelled and becomes more solvent accessible upon Ca^{2+} binding. The red shift of maximum wavelength (Figure 4-5d) reflects Trp12 becoming more exposed to the solvent, as Ca^{2+} ions trigger the N-terminal domain expulsion from the C-terminal core. The discrepancy of fluorescence intensities at

pH 6.0 and pH 8.0 values suggests AnxA1 may adopt slightly different conformations at different pH values.

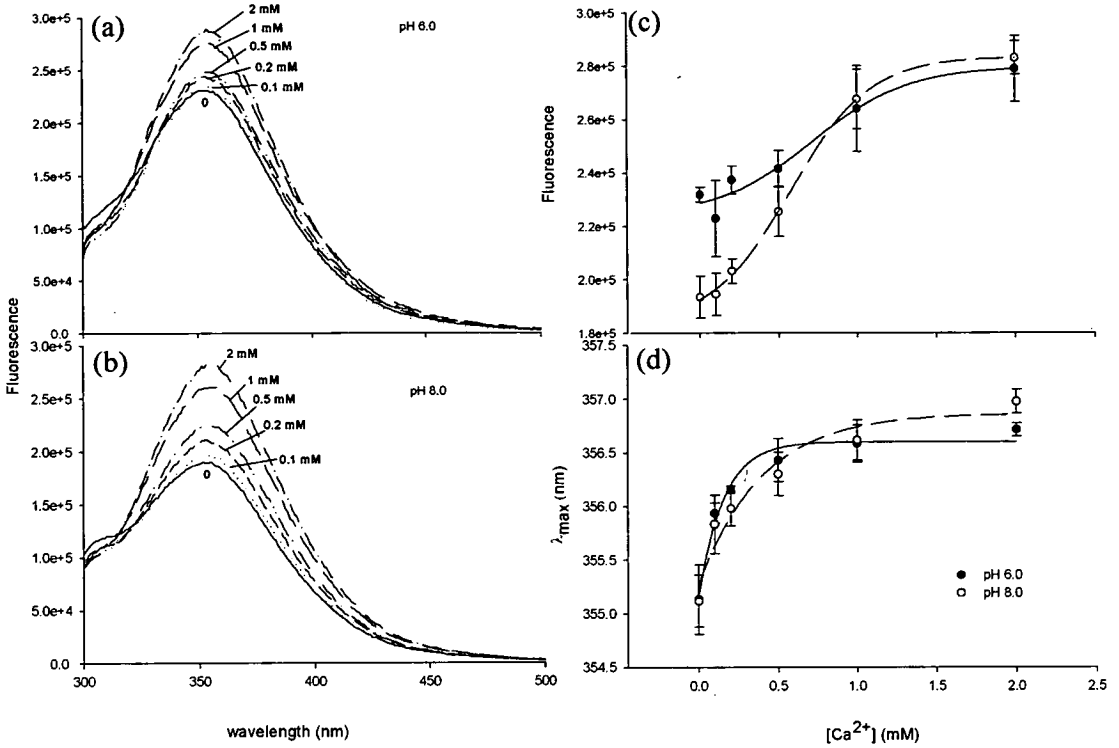

Figure 4-5 Fluorescence emission spectra of human AnxA1 at different Ca^{2+} concentrations (0 ~ 2 mM) measured at (a) pH 6.0 and (b) pH 8.0. (c) Fluorescence intensities and (d) emission maxima wavelength of human AnxA1 at different Ca^{2+} concentrations. Data were collected at pH 6.0 (filled circles) and pH 8.0 (open circles).

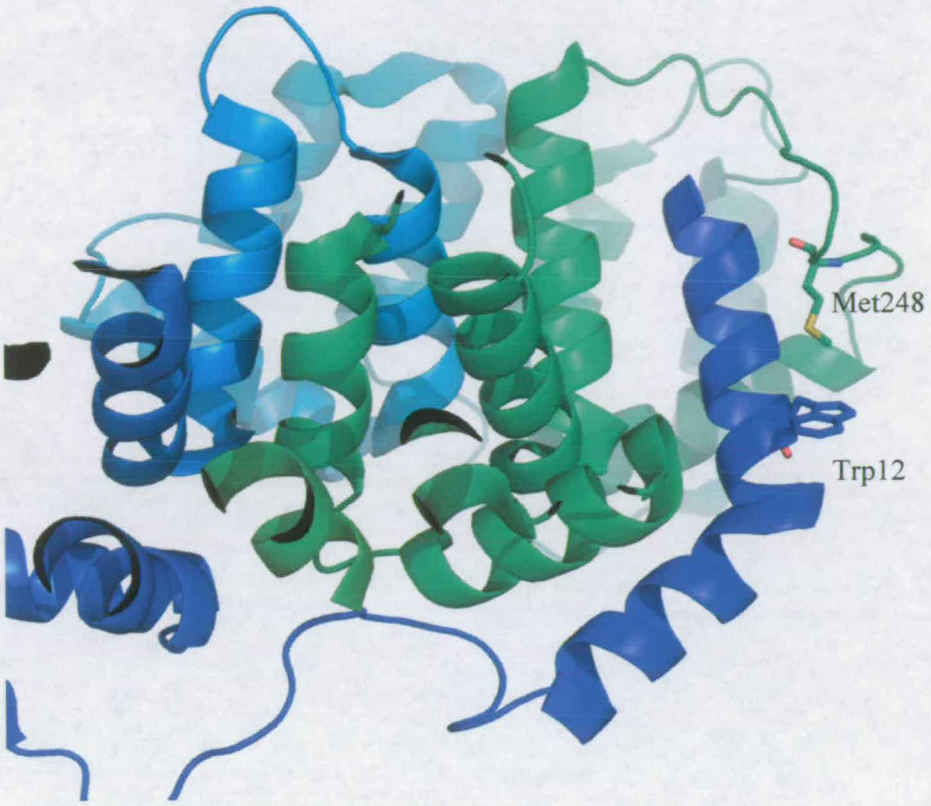

Figure 4-6 X-ray structure of the N-terminal domain inserted into the C-terminal core of AnxA1. The side chains of Trp12 and Met248 are present in stick form.

4.2.4 Vesicle aggregation induced by human AnxA1

To compare membrane aggregation activity of AnxA1at different Ca^{2+} concentrations and pH, AnxA1-induced vesicle turbidity at pH 6.0 and pH 8.0 was measured at an absorbance of 450 nm. SUVs composed of DMPC/DMPS (3:1) were prepared at a lipid/protein ratio of 800:1 (mol). The absorbance was plotted against Ca^{2+} concentrations at the two pH conditions (Figure 4-7). It is shown that vesicle turbidity increases as more Ca^{2+} ions are present in solution. These results confirm the Ca^{2+}-dependent nature of AnxA1 membrane aggregation. However, it has been shown that the vesicle binding ability of AnxA1 is much stronger in acidic environment than in basic environment: Lee et al. have used PS liposomes to study the membrane aggregation activity of AnxA1 (*51*). They observed that AnxA1 has

the highest vesicle aggregation ability at pH 6.0. Their data are correspondent with the results in the studies, despite the vesicles being composed of DMPC/DMPS mixture. The Ca^{2+}-dependent vesicle turbidity measurements were performed in the presence of up to 1 mM Ca^{2+}, because higher Ca^{2+} concentrations caused vesicle aggregation even without the presence of AnxA1. Pure DMPS SUVs are not suitable for high [Ca^{2+}] titration experiments because pure DMPS SUVs started to self-aggregate at 0.2 mM Ca^{2+} and disturbed the measurements of vesicle turbidity induced by AnxA1 (data not shown).

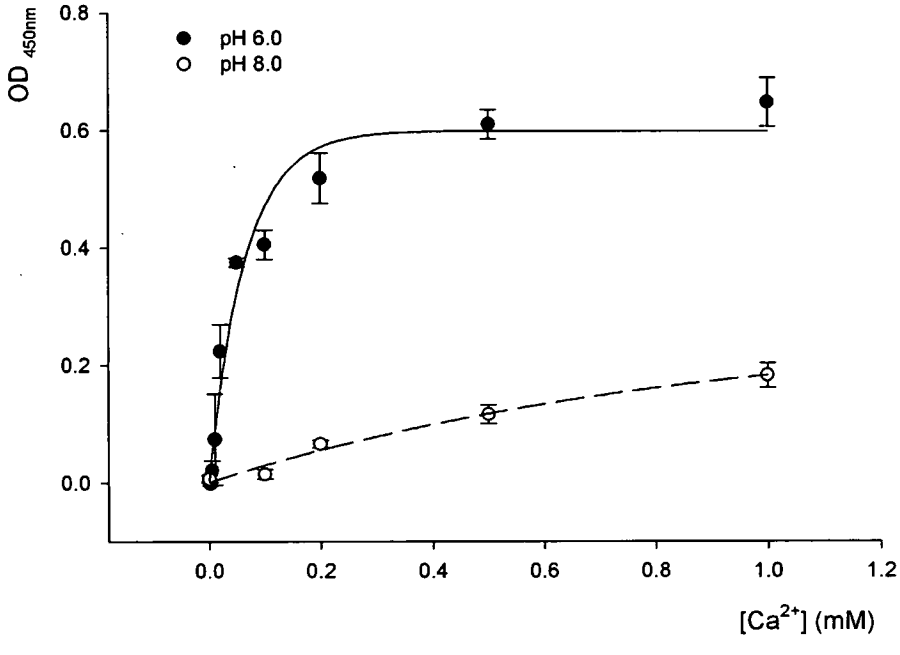

Figure 4-7 Liposome turbidity assay performed by mixing DMPC:DMPS (mol 3:1) SUVs and human AnxA1 at pH 6.0 (filled circles) and pH 8.0 (open circles), in the absence of Ca^{2+} and presence of Ca^{2+} (0.1 ~ 1.0 mM).

4.2.5 Fluorescence emission of human AnxA1 in the presence of vesicles

Fluorescence emission spectra of AnxA1 in the presence of unilamellar vesicles were measured at different Ca^{2+} concentrations and pH values (Figure 4-8). The emission spectrum of Trp12 after addition of SUVs shows a slight increase in fluorescence intensity at pH 6.0 (dotted line in Figure 4-8a). However, the quantum yield of Trp12 reveals a 30% increase after addition of vesicles at pH 8.0 (dotted line in Figure 4-8b). Interestingly, after Ca^{2+} addition, an alternative peak at an emission wavelength of 340 nm became pronounced at pH 6.0. In contrast, at pH 8.0, addition of Ca^{2+} causes no extra fluorescence peak can be detected at 340 nm and the fluorescence intensities were weaker compared with pH 6.0. It has been demonstrated aggregated SUVs cause non-specific scattered light and contribute to the emission signal (*113*). The Ca^{2+}-dependent tendency of the extra peak at pH 6.0 implicates AnxA1 induces more vesicles to aggregate as Ca^{2+} concentrations increase. These measurements might have benefited from the use of fluorescence polarisation (not accessible in the department). Nevertheless, a notable blue shift of tryptophan emission peak maximum upon addition of Ca^{2+} can be observed at pH 6.0: the maximum wavelength is fitted at 355.1 nm in the absence of Ca^{2+}, 349.1 nm in the presence 0.1 mM Ca^{2+} and 349.8 nm in the presence 2 mM Ca^{2+}. By contrary, at pH 8.0, addition of Ca^{2+} causes a slightly red shift or no change of the maximum wavelengths. Fluorescence intensity ratios at 350 nm and 380 nm were thus plotted against Ca^{2+} concentrations (Figure 4-8c). A significant increase of the I_{350}/I_{380} ratio is shown as Ca^{2+} concentrations increases at pH 6.0. The Ca^{2+}-dependent increase in the I_{350}/I_{380} ratio reaches saturation (about 1.55) in the presence of 0.1 mM Ca^{2+}. On the other hand, at pH 8.0, the ratio remains nearly unchanged upon Ca^{2+} addition. The results show that more Trp12 species are in a more hydrophobic environment as membrane aggregation occurs.

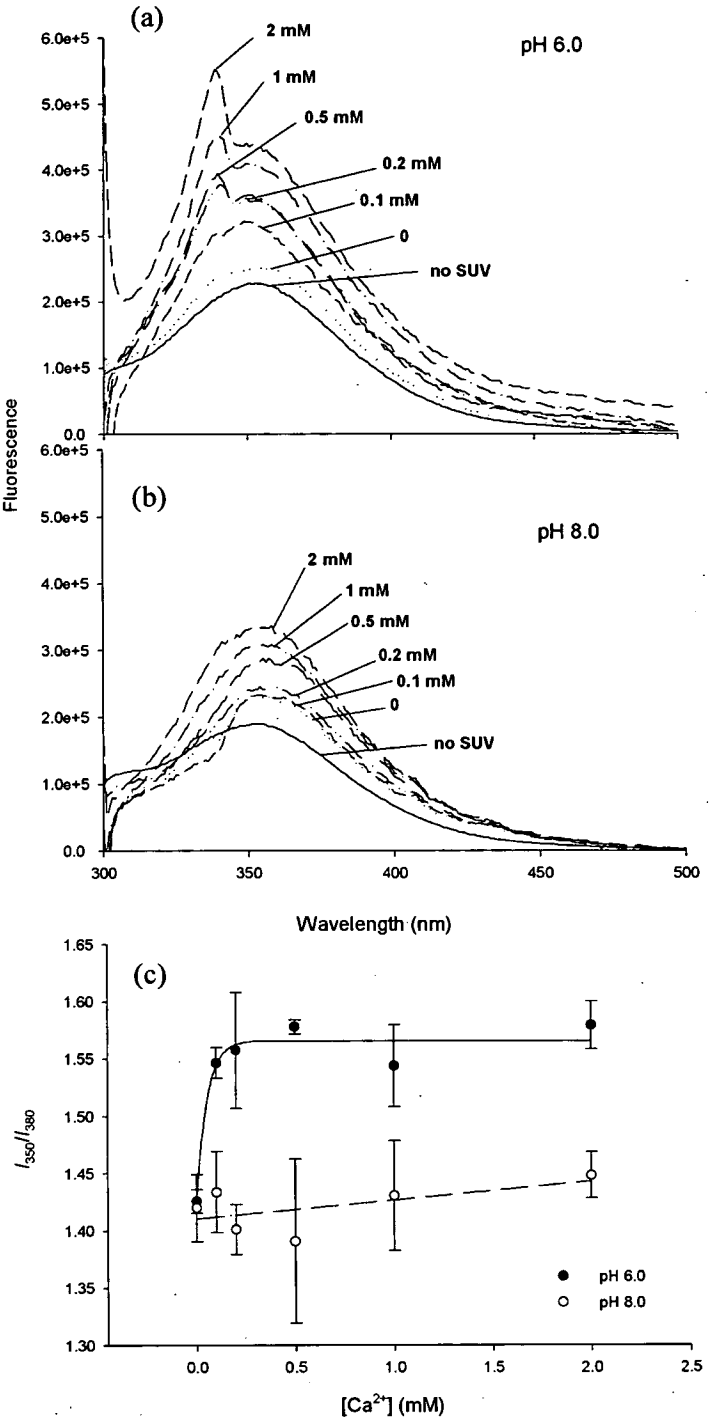

Figure 4-8 Fluorescence emission spectra of human AnxA1 at different Ca^{2+} concentrations (0 ~ 2 mM) in the presence and absence of DMPC:DMPS SUVs (mol 3:1) The spectra were collected at pH 6.0 (a) and pH 8.0 (b). (c) Fluorescence intensity ratios at 350 nm and 380 nm (I_{350}/I_{380}) at pH 6.0 (filled circles) and pH 8.0 (open circles).

4.2.6 Mechanisms of membrane aggregation induced by human AnxA1

Liposome turbidity assays reveal that AnxA1 possesses a strong ability to induce vesicle aggregation at pH 6.0 in the presence of Ca^{2+} (Figure 4-7). Fluorescence spectroscopy demonstrates that the N-terminal domain of AnxA1 is in a more hydrophobic environment upon membrane aggregation (Figure 4-8). However, these results cannot provide direct evidence for either of the AnxA1-mediated membrane aggregation models. An indirect method might provide another perspective to examine the membrane aggregation mechanism. A copelleting assay has been employed in the study to monitor the membrane-binding ability of annexin proteins induced by Ca^{2+}. Theoretically, the binding behaviour should be reversed if a chelator, such as EDTA, strips off the calcium ions. As a result, proteins which cannot be recovered by the chelation are considered to be involved in an irreversible membrane interaction involving the hydrophobic residues of and the phospholipid membrane. To examine if the AnxA1 N-terminal domain is involved in membrane aggregation, a copelleting assay followed by addition of a chelator seems feasible.

As described in chapter 3.4, supernatant and pellet were carefully separated after adding EDTA. Figure 4-9 shows the percentage of proteins in the supernatant and pellet compared to a reference sample. Ideally, proteins found in the supernatant would represent the fraction of AnxA1 reversibly bound to the membrane. In contrast, proteins found in the pellet would show an irreversible interaction with the membrane. For proteins found in supernatant, AnxA1 reveals a Ca^{2+}-dependent membrane binding and reaches the maximal membrane binding to 80% of protein at 0.5 mM Ca^{2+} (shown as filled circles). Interestingly, AnxA1 was also found within the pellet, representing the protein species cannot be recovered by EDTA. The irreversible membrane-bound AnxA1 also shows a Ca^{2+}-dependent tendency and reaches a maximum of 17% membrane binding at 0.5 mM Ca^{2+} (shown as open circle). This

suggests the secondary membrane-binding behaviour involves Ca^{2+}, and the proteins found in the pellets are not just the residual supernatant protein on pellets after centrifuge separation.

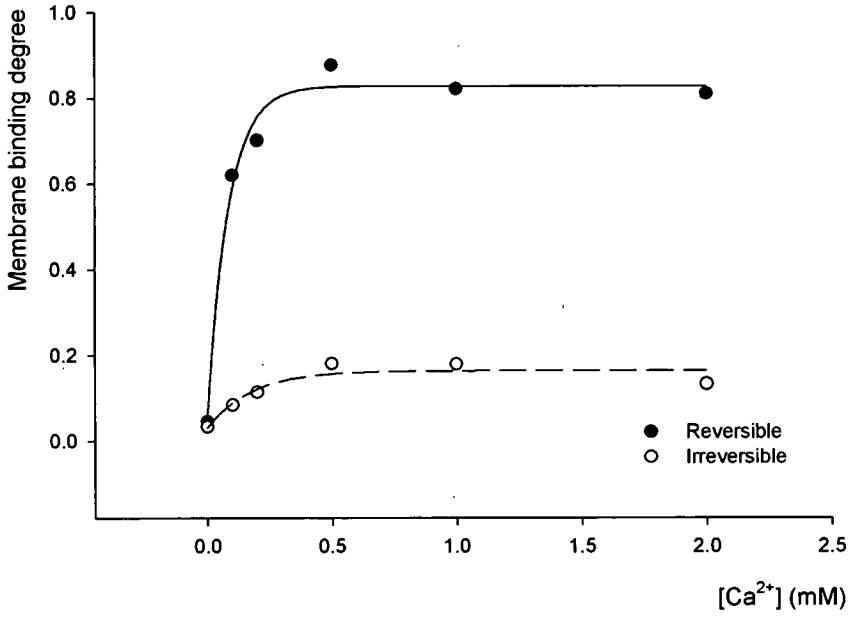

Figure 4-9 Reversible (filled circles) and irreversible (open circles) membrane-binding degree of human AnxA1 derived from a conventional copelleting assay followed by addition of EDTA.

4.3 Discussion

AnxA1 exhibited an invariant structure at different Ca^{2+} concentrations and pH values (Figure 4-2). The CD spectra are in good agreement with an earlier secondary structure study measured at pH 3.8, 4.5, 5.0, 6.0, 7.0 and 8.0 (*114*). However, DSC studies on AnxA1 using Ca^{2+} in a range from 0 to 100 mM caused the transition temperature shift from 62.6°C to 72.3°C (*115*). The transition temperature also revealed a small shift from 58.5°C to 62.3°C at a pH range from 8.0 to 4.5 (*114*). The increase in transition temperature indicates that Ca^{2+}

ions and an acidic environment do stabilise the conformation of AnxA1 although they do not significantly help the protein folding into α-helical structure.

The membrane-induced refolding of the rat AnxA1 2-26 peptide (Figure 4-4) is very consistent with the CD results of human AnxA1 N-terminal peptide (residues 1-26) (*75*) and human AnxA2 peptide (residues 1-31) (*76*). The present CD results show the AnxA1 peptide adopts an α-helical conformation in the presence of vesicles, which adds support to a direct membrane-binding property of the AnxA1 N-terminal domain. Interestingly, full-length AnxA1 exhibited an increase in α-helical content upon Ca^{2+}-dependent membrane aggregation (Figure 4-3). From the closed-form crystal structure, it is known that the N-terminal domain of AnxA1 inserted in the C-terminal core adopts an α-helical structure in the absence of Ca^{2+} (*11*). Unfortunately, the exposed form of AnxA1 in the presence of Ca^{2+} does not provide any structural information of the N-terminus (*12*). However, the X-ray structure has proved the refolding of the helix D in the repeat III when the N-terminus is expelled (Figure 1-3). Therefore, the increase in α-helical component is potentially due to the refolding of the C-terminal domain during membrane binding in the presence of Ca^{2+}. Intriguingly, it is still not well characterised whether the N-terminus adopts a helical conformation when it is expelled, as the AnxA1 N-terminal peptides reveal a random coil structure in the absence of membrane (Figure 4-4). In addition, the X-ray structure of closed-form AnxA1 shows the residues from Ser28 to Asn43 form a random coil, so one cannot rule out the possibility that membrane facilitates the region to fold into a helical structure.

The membrane interaction of AnxA1 has been studied by monitoring its single tryptophan on the N-terminus using fluorescence spectroscopy (*105*). AnxA1 revealed an increase in tryptophan fluorescence intensity and a small red shift at 100 μM Ca^{2+} and pH 7.4 in the presence of PS/PC (mol 1:1) LUVs. The author claimed AnxA1 was at a membrane-binding state (instead of membrane aggregation state) using its primary binding site at the relatively

low Ca^{2+} concentration (100 μM). There appears to be no interaction between the N-terminus and membrane, as no fluorescence quenching effects were observed when using spin-labelled phospholipids at varying depths. Interestingly, a small red shift of fluorescence emission has been reported upon Ca^{2+} addition to the AnxA1 solution in the absence of membrane (*104*). In agreement with the fluorescence data (Figure 4-5), AnxA1 shows a Ca^{2+}-dependent domain movement of the N-terminus in the absence of vesicles. The results suggest that when Ca^{2+} ions bind the surface of the AnxA1 C-terminal core, either in the presence or absence of vesicles, the buried N-terminal domain is less tightly inserted into the C-terminal core and becomes more solvent-accessible. Upon membrane aggregation, the blue shift of the tryptophan emission peak (Figure 4-8) implicates that the exposed N-terminus might make contact with a membrane via hydrophobic interactions.

The monolayer lateral surface pressure measurements of AnxA1 and AnxA5 are in very good agreement with previous reported data (*73*), indicating that AnxA1 can interact with membrane in the absence of Ca^{2+}. However, AnxA5 does not possess this property (Figure 4-1a). The results gave good positive and negative controls for the following measurements with AnxA1 N-terminal peptides. Rat AnxA1 shares 80 % similarity in the N-terminal domain with human AnxA1, and has been shown to be able to cause liposome aggregation (*116*). The two mutant peptides S27A and S45A were originally synthesised to block the phosphorylation sites on the N-terminal domain. The results shown here suggest rat AnxA1 N-terminal peptides are able to interact with membrane directly without the assistance of Ca^{2+} ions. The p*I* values for rat AnxA1 2-26, 1-50 S27A and 1-50 S45A are 4.7, 4.8 and 4.8 respectively. At pH 6, the interactions between the peptides and acidic phospholipid molecules are not simply electrostatic in nature. Instead, hydrophobic interactions might thus play a key role in the membrane binding behaviour. It has been shown that planar bilayer-bound AnxA1 reveals no preference to for the predominantly negatively charged PS

liposomes (*74*). The chimeric protein composed of the N-terminus of AnxA1 and the C-terminal core of AnxA5 revealed a requirement for an anionic phospholipid bilayer for its primary membrane binding and ability to bind pure PC vesicles (*52*). X-ray structure data of human AnxA1 provided the detailed information that the long N-terminal domain is in an amphipathic α-helical conformation (*11*). The surface pressure increase caused by AnxA1 N-terminal peptides (Figure 4-1b) suggests a Ca^{2+}-independent interaction between membrane and the N-terminal domain of AnxA1. However, for characterising fine detail of the binding interactions, structural studies at molecular level are essential. In chapter 5, it will be discussed about the membrane-binding behaviour of AnxA1 N-terminal peptides using neutron diffractometry.

The mechanism of membrane aggregation induced by AnxA1 is a controversial issue because no conclusive model exists. What conformation does AnxA1 adopt during membrane aggregation? The fluorescence data demonstrating a blue shift of fluorescence peak are not sufficient to draw a conclusion that the expelled N-terminal domain interacts directly with membrane (Figure 1-2, model A). This is because the 'tail to tail' dimer model shows the two N-termini of the AnxA1 dimers interact with each other (Figure 1-2, model B), which could potentially result in an increase hydrophobicity surrounding Trp12. This would also result in a blue shift in the fluorescence data. However, it is important to note that if AnxA1 adopts the 'tail to tail' dimer conformation during membrane aggregation, the dimer formation should be also detectable upon Ca^{2+} addition in the absence of vesicles. This is because the expelled N-terminal domain driven by Ca^{2+} ions should be able to form a dimer in solution. The red shift of fluorescence in the absence of vesicles shown in Figure 4-5 apparently contradicts this assumption.

It has been reported that the Ca^{2+}-dependent membrane binding of annexins is reversible after EDTA addition (*45, 105, 117*). It has also been shown that AnxA1 in the presence of

PS liposome and low Ca^{2+} concentrations (50-100 μM) is at non-aggregated state, and can mediate aggregation of additional PS liposome at higher Ca^{2+} concentrations (0.5 -1 mM). The aggregation can be reversed upon EGTA addition (*71*). The copelleting assay reveals that both reversible and irreversible membrane-binding behaviours are related to Ca^{2+} concentrations (Figure 4-9). The phenomenon can be perfectly explained by model A in Figure 1-2, where the aggregation mechanism is mediated by two membrane binding sites on AnxA1 monomer. Firstly, Ca^{2+} ions assist the association between the primary membrane and protein C-terminal core, and secondly, the bound Ca^{2+} ions trigger the exposure of the N-terminal helix, which interacts with the secondary membrane. The unrecoverable proteins attached on vesicles after Ca^{2+} chelation is potentially due to the hydrophobic interactions between the AnxA1 N-terminal helix and secondary membrane. If membrane aggregation were initiated based on model B, however, it would be unlikely to observe irreversible membrane binding of AnxA1. This is because EDTA should be able to dissociate the dimer from two adjacent membrane leaflets and no protein should be observed in vesicle pellets.

Previous studies on membrane aggregation mediated by AnxA1 (*45, 53, 74, 118*) support this hypothesis. Meers et al. discovered that EDTA does not allow complete disaggregation of vesicles induced by AnxA1 (*45*). Kastl et al. found that AnxA1 form a two-dimensional cluster on solid-supported membranes and the N-terminal region plays a key role in binding to the second membrane (*118*). Additionally, Bitto et al. demonstrated that AnxA1 functions as a protein monolayer in membrane aggregation, and the lateral protein association is mediated by the C-terminal core of AnxA1 (*74*). They also demonstrated the hydrophobic nature of secondary membrane interactions, and that it does not require acidic lipids to mediate membrane aggregation. Nevertheless, conflicting results were observed by Lambert et al. (*72*), suggesting membrane aggregation is mediated by an axial dimer. They proposed a model based on the observed number of stripes in DOPG-DOPC liposome junctions by cryo-

electron microscopy. It should be noted that they observed the proteins and liposomes mixture in a buffer at pH = 7.4. The findings correspond to the small angle neutron scattering results in chapter 5 indicating the multilamellar vesicle *d*-spacing at pH 8.0 is 146 Å (Table 5-6). The distance is comparable with their finding that bilayer thickness = 114 Å in the presence of AnxA1 and Ca^{2+} (*72*). The liposome turbidity assays demonstrate that AnxA1 exhibits a weaker activity in membrane aggregation in basic conditions (Figure 4-7). It has been demonstrated that AnxA1 shows its highest vesicle aggregation ability at pH 6.0 and only 20% aggregation ability at pH 7.5 (*51*). Therefore, the membrane junction distance observed at pH 7.4 by electron microscope may not reflect optimally-mediated membrane aggregation.

It is presumed that, in basic environments, the interactions of AnxA1 with membrane are different from that in acidic environments, and the membrane aggregation ability is thereby altered. Although pH value plays a key role in AnxA1-induced membrane aggregation, model A seems to be the most reasonable scenario for AnxA1-mediated membrane aggregation at acidic pH. The mechanism of membrane aggregation induced by AnxA1 will be further discussed using small angle neutron scattering in chapter 5.

5 Neutron diffraction and small angle neutron scattering

5.1 Introduction

It has been shown in chapter 4 that the N-terminal domain of AnxA1 is in a more hydrophobic environment when the protein is in a membrane-aggregated state (Figure 4-8). CD measurements showed that the presence of phospholipid vesicles enhances the α-helical component of the rat AnxA1 N-terminal peptide (residues 2-26) (Figure 4-4). All the results suggest a direct interaction of AnxA1 N-terminal domain with a second membrane without the assistance of Ca^{2+} ions. This argument is supported by the amphipathic nature of the N-terminus (*11*) and its ability to bind to zwitterionic phospholipids after primary membrane binding to an acidic phospholipid-containing membrane (*74*). The purpose of the experiments described in this section, is to study the interactions of AnxA1 N-terminal peptides with a phospholipid bilayer using neutron diffraction. In addition, the model of Ca^{2+}-dependent membrane aggregation induced by full-length AnxA1 has been studied by measuring the *d*-spacing of a multilamellar bilayer system using the Bragg's peaks observed in small angle neutron scattering profiles.

5.2 Neutron diffraction

Neutrons are located in the atomic nucleus and they can be produced from two sources: a nuclear reactor and a process called nuclear spallation. In a nuclear reactor, numerous

neutrons are set free in the process of nuclear fission in a nuclear chain reaction. In a nuclear spallation source, neutrons are produced when high-energy proton pulses strike mercury, tantalum or other heavy metal targets. Although nuclear spallation is a more expensive way to produce neutrons, its proton pulse makes it easier to control the reaction.

X-rays are diffracted by the electron cloud surrounding an atom. Therefore, X-ray diffraction power for an atom with a large atomic number will be stronger than that with a small atomic number. However, neutrons are diffracted by the nucleus of an atom, not by electrons. The feature provides an advantage of neutron diffraction to locate hydrogen atoms, which are not visible in X-ray diffraction. Hydrogen and its isotope deuterium diffract neutrons very effectively, but with opposite phase angle. Therefore, in a neutron scattering map, hydrogen gives a negative peak, while deuterium gives a positive peak. Neutrons are non-destructive and can penetrate deep into matter, allowing them an ideal probe for biological materials and samples. Neutrons behave as either particles or waves, and their wavelength can range from 0.1 Å to 1000 Å, making them a useful tool to study biological macromolecules at an atomic level.

Neutron diffraction is a structural method, which is also based on Bragg's law. The technique has been applied to study structure of membrane bilayers using lamellar phospholipid preparations. Phospholipid molecules normally form an ordered multilayer on solid substrates upon evaporation of solvent from solution (*119*). The multilayer can be thousands of sheets thick and the periodic multilayer is like a one-dimensional crystal along an axis perpendicular to the membrane plane. Therefore the diffraction conditions are determined based on Bragg's law

$$n\lambda = 2d\sin\theta, \qquad \textbf{Equation 5-1}$$

where n is any integral, λ is the wavelength of the neutron beam, d is the distance of multilayer spacing and θ is the incident angle. When the incident neutron beam with angle θ and wavelength λ, as well as the d-spacing of the lattice plane satisfy Bragg's law, neutron particles are diffracted and collected on a detector positioned at an angle of 2θ (Figure 5-1a). As the sample rotates to a larger θ angle, another order of diffraction occurs with shorter d-spacing and provides finer structural information (Figure 5-1b). The process of data collection is called θ-2θ scan. With several orders of diffraction, one can obtain a set of the structure factor amplitudes, which can be utilised in Fourier transformation to regenerate a neutron scattering density profile of the phospholipid bilayer.

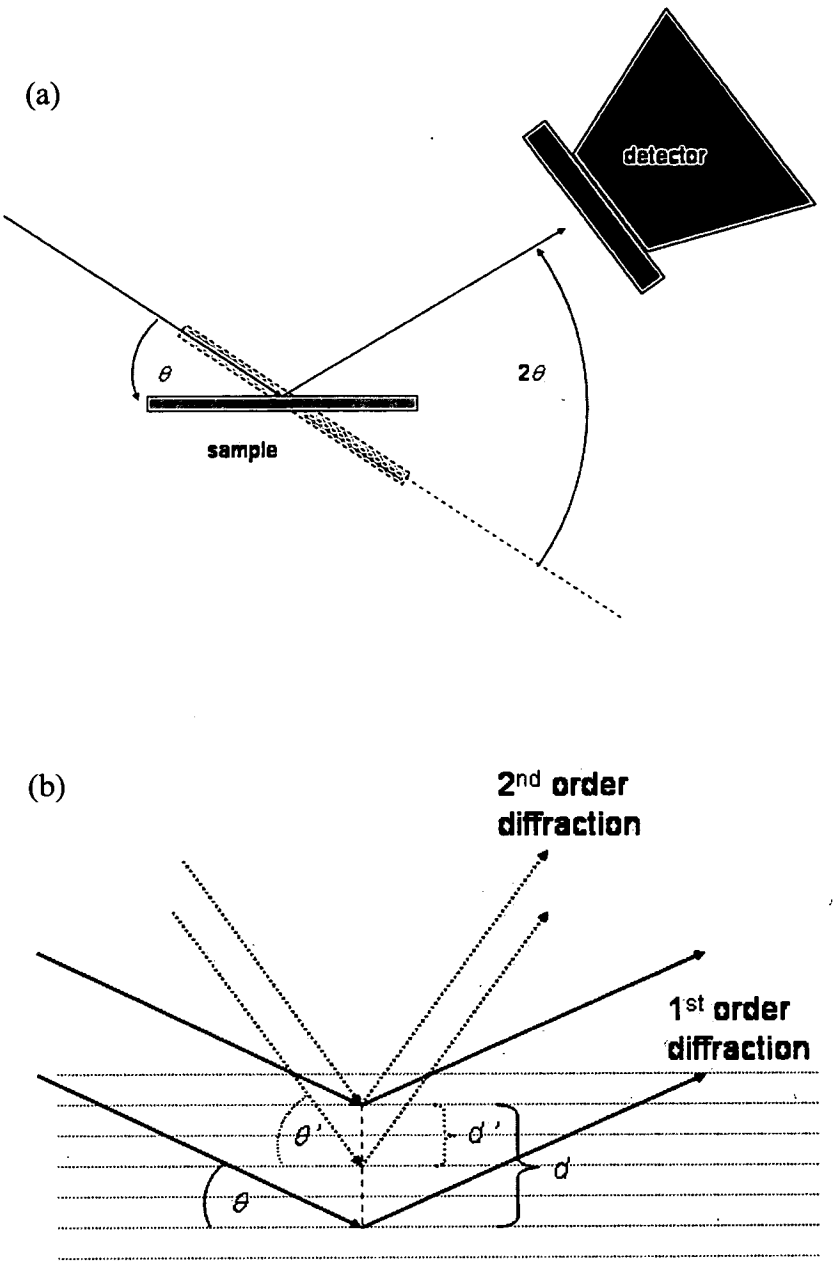

Figure 5-1 (a) A schema of the neutron diffractometer, where Bragg's law is satisfied when sample is rotated with an angle θ. The detector is moved to the position with an angle 2θ to collect the diffracted neutron particles. (b) The thick black lines represent the 1st order neutron diffraction from the parallel multilayer spaced a distance of d apart with the incident angle θ. The dotted lines represent the 2nd diffraction from the parallel multilayer spaced a distance of d' apart with the incident angle θ'.

Like X-ray crystallography, amplitudes are easily obtained from the diffracted spots on the detector, whereas phase angles are missing. The structure factor for each order can described using the relation

$$F_{obs}(h) = S(h)\sqrt{I_{obs}(h)}\,, \qquad \textbf{Equation 5-2}$$

where h is the order number and $S(h)$ is a phase factor which can be determined by swelling-series experiment (*98, 120*). As the structures of multilayer phospholipids are centrosymmetric, the phase angles are either 0 or 180°. Therefore $S(h)$ is equal to either +1 or -1 (*121*). Swelling experiments are composed of a set of samples with different lamellar spacings, accomplished by controlling the relative humidity of the atmosphere (*122*). Sample slides are placed in a sealed can and the bilayers swell by absorbing water from the atmosphere. θ - 2θ scans are performed in different relative humidities. The structure factors for each scan will shift slightly and thereby have correspondingly different amplitudes.

It has been demonstrated that the structure factors collected at 8% ^2H_2O solution may be simultaneously fitted to a single continuous transform (*98, 122*). The continuous transform $C(z)$ can be calculated using

$$C(z) = \sum_{h=0}^{h_{max}} F_{obs}(h)\frac{\sin(\pi dz - \pi h)}{(\pi dz - \pi h)}, \qquad \textbf{Equation 5-3}$$

where h is the order number, $F_{obs}(h)$ are the structure factors, d is the lamellar spacing, and z is the coordinate normal to the plane of the membrane (*98, 122*). Because water with 8% ^2H_2O composition has a net neutron scattering density of zero, the water molecules with the isotopic composition are invisible in neutron scattering density map. As humidity increases, more water molecules are absorbed by the samples, but the zero-scattering-density water will not cause any effect on the scattering structure of the bilayer. The sets of structure factors

collected at 0% ^2H_2O and 8% ^2H_2O are compared in Figure 5-2. The square roots of observed intensities are plotted against spatial frequencies. For correct assignment of phase angles, the observed structure factors should be fitted to a smooth continuous transform curve. The swelling series produces oscillations of Bragg peaks, which enhance the accuracy of curve fitting and phase angle determination (*123*).

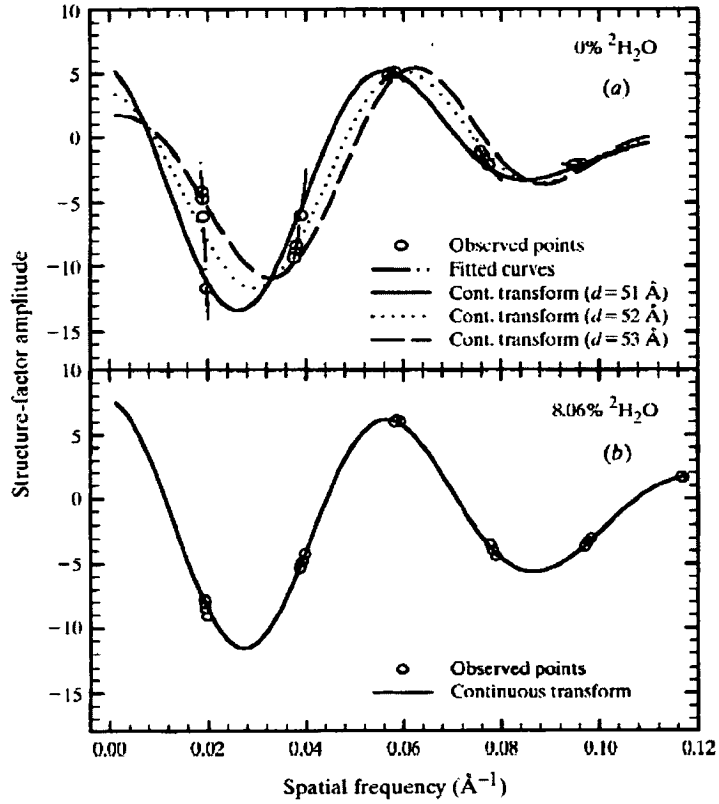

Figure 5-2 Plots of structure factor amplitudes against spatial frequency of observed data points collected by swell-series experiments. Diffraction data were collected at (a) 0% ^2H_2O and (b) 8% ^2H_2O solution. Data from Darkes & Bradshaw (*98*).

The neutron scattering length density for the bilayer can be described as a one-dimensional dissection profile, using a Fourier series of the summation of cosine terms,

$$\rho(z) = (2/d)\sum_{h=1}^{h_{max}} F(h)\cos(2\pi z h/d) \quad (121, 123). \qquad \textbf{Equation 5-4}$$

Diffraction data may be placed by a "relative absolute" scaling approach using the known mean scattering length of the introduced peptide (*124, 125*) to scale the data sets absolutely, with respect to the unit cell contents. Data sets of pure lipids and peptide-incorporated lipids are adjusted relatively, with different scaling factors, until their difference transform meets the calculated scattering length of peptide per unit cell. The "relative absolute" method scales the profiles with respect to the unit cell contents, instead of the whole bilayer system. Therefore, knowledge of the molar ratio of peptide to lipid is required. The neutron scattering density profile represents a unit cell containing two phospholipid molecules. Therefore, at 1% peptide to lipid ratio, the density map intensity of the added peptide in the unit cell actually accounts for only 2% of its original scattering intensity.

5.3 Small angle neutron scattering (SANS)

Small angle neutron scattering (SANS) has been developed with its sister technique, small angle X-ray scattering (SAXS) and light scattering (LS). The scattering technique has been employed to study the size and shape of biological macromolecule, such as protein (*126*), membrane (*127*) and virus (*128*). As mentioned in 5.2, hydrogen atoms have a negative neutron scattering length, whereas deuterium atoms have a positive scattering power. The neutron scattering strength is an inverse function of the degree of hydrogenation of the molecules. As a result, SANS provides a higher scattering contrast to differentiate biological macromolecule (*129*).

In SANS experiments, crystalline structure of a material can be detected as a Bragg diffraction peak in SANS scattering profiles. Therefore, the diffraction peaks provide important information of the crystalline distance. The major advantage of SANS is that the measured samples can be in solution or in their native status. The technique has been widely applied to study fibre orientation (*130*) and multilamellar biomembrane (*103*). In this study, MLVs have been used to monitor the *d*-spacings of the periodic structure of multiple membrane stacks after addition of full-length human AnxA1. From the calculated *d*-spacing of the aggregated membranes, one would extrapolate a possible model of membrane aggregation induced by AnxA1.

5.4 Results

5.4.1 Neutron diffraction

The neutron diffraction experiments of multilamellar phospholipid containing AnxA1 N-terminal peptides were performed at the D16 instrument at ILL, France. The lamellar spacings (*d*-repeats) of the DMPC/DMPS (mol 3:1) bilayer at 90% relative humidity were determined by least squares fitting to the five orders of neutron diffraction. As Table 5-1 shows, the *d*-repeats do not change significantly after addition of 1% (mol) AnxA1 N-terminal peptides. Also, human and rat AnxA1 N-terminal peptides reveal no significant differences in lamellar spacings. The almost unchanged unit cell in the *Z*-direction upon addition of the peptides rules out the possibility of superficial interaction of peptide and lipid. The results correspond to the monolayer lateral surface pressure measurements, suggesting a penetration of AnxA1 N-terminal peptides into the phospholipid monolayer (Figure 4-1). However, the orientation of the peptides interacting with phospholipid monolayer (i.e. perpendicular penetration or parallel annealing) remains unclear. To accommodate the peptides, there are two possible explanations: either the peptides lie parallel to the bilayer surface, or they insert vertically into the bilayer. Knowledge about the amphipathic conformation of the N-terminal helix of human AnxA1 derived from the X-ray structure suggests that the former mechanism is more likely.

	d-repeat (Å)
DMPC/DMPS (mol 3:1)	54.45
DMPC/DMPS (mol 3:1) + 1% (mol) human AnxA1 1-21	54.52
DMPC/DMPS (mol 3:1) + 1% (mol) rat AnxA1 2-26	54.45

Table 5-1 Lamellar spacings (*d*-repeats) of the DMPC/DMPS (mol 3:1) bilayer in the presence or absence of AnxA1 N-terminal peptides.

Neutron structure factors for each diffraction order calculated using Equation 5-2 are shown in Table 5-2. Neutron scattering density profiles of the DMPC/DMPS bilayer, in the presence or absence of the peptides, are shown in Figure 5-3 by calculating with the structure factors in Table 5-2 using Equation 5-4. As described earlier, at 8% ^2H_2O composition, the mean neutron scattering length of the water mixture is zero (*121*). The trace shown with a solid line represents the transection of the neutron scattering length density profile of the phospholipid bilayer along the *Z*-axis, perpendicular to the surface of the lipid bilayer. The two maximal peaks of the profiles arise from a combination of the phosphate-containing headgroups and the hydrogen-poor glycerol groups, whereas the minimum in the centre indicates the hydrogen-rich methyl groups at the bilayer centre. The short dash trace (Figure 5-3), obtained by subtracting structure factors for lipid bilayer containing peptide from structure factors for pure lipid followed by Fourier transformation, describes the difference profile of human AnxA1 1-21 and rat AnxA1 2-26 peptides.

As shown in Figure 5-3, both peptides appear at the interface of phospholipid headgroup and alkyl chains. To obtain more quantitative measurements of the changes induced by AnxA1 N-terminal peptides in the bilayer structure, the peaks of the difference profiles were fitted to a single pair of Gaussians in reciprocal space (diffraction data) thereby determining the

position of the peptides in lipid bilayers. This is due to the high order of diffraction data are always missing, which results in errors in the neutron scattering profiles (calculated by Fourier synthesis of the diffraction data). These errors would affect the Gaussian fitting process. However, Gaussian fitting in reciprocal space based on the observed diffraction avoids the errors, and gives accurate Gaussian fitting to the Angstrom level (*123*). The parameters are summarised in Table 5-3. Note that, in each case, the difference was adequately described by a single pair of Gaussians, indicating that the minor peaks located at the bilayer centre are artefacts, produced by termination error. Each of the peptides appears at the interface of phospholipid headgroup and alkyl chains, the narrow width suggesting a parallel orientation relative to the bilayer surface. The Gaussian peaks characterising human AnxA1 1-21 and rat AnxA1 2-26 are positioned at 19.05 Å and 19.36 Å respectively, very close to the maxima representing the headgroups and glycerol groups of the phospholipids.

	F(1)	*F*(2)	*F*(3)	*F*(4)	*F*(5)
DMPC/DMPS (mol/mol 3:1)	-20.59	-5.76	8.68	-6.04	-2.14
DMPC/DMPS (mol/mol 3:1) + human AnxA1 1-21	-22.83	-6.31	10.56	-5.89	-1.98
DMPC/DMPS (mol/mol 3:1) + rat AnxA1 2-26	-22.96	-6.38	10.17	-6.91	-2.50

Table 5-2 Neutron structure factors $F(h)$ of the AnxA1 N-terminal peptides in the bilayer DMPC/DMPS (mol 3:1). h stands for the diffraction order. Data were collected at 90% relative humidity, 8% ^2H_2O, 26 °C.

(a)

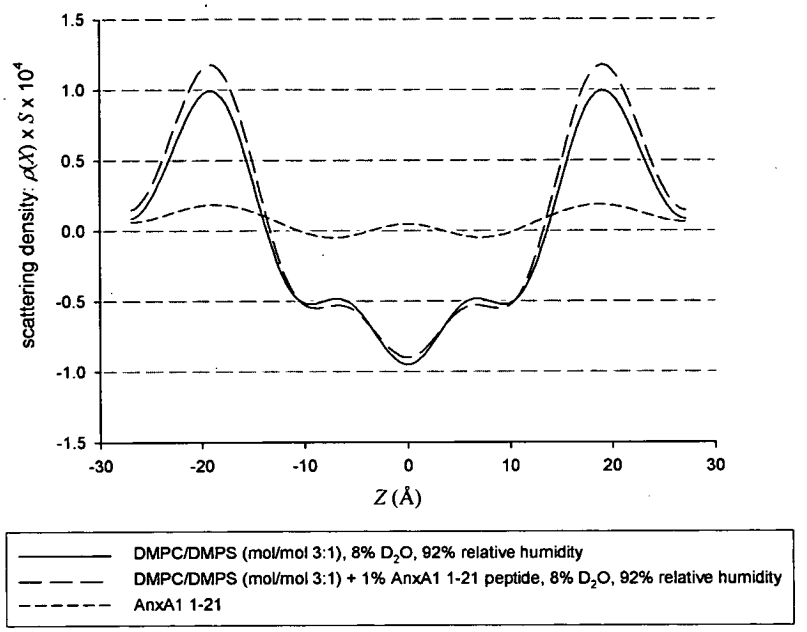

(b)

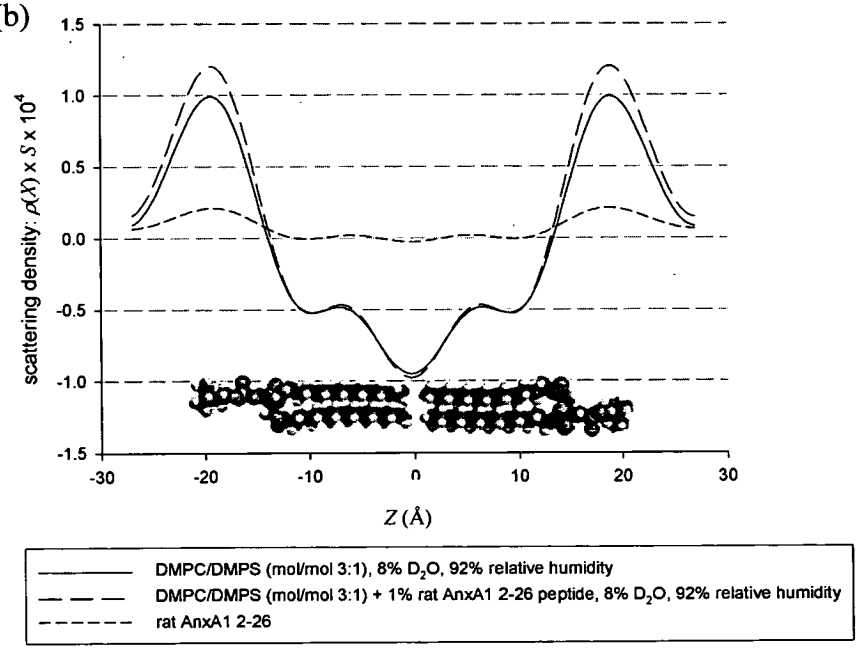

Figure 5-3 Neutron scattering profiles of DMPC/DMPS (mol 3:1) in the presence of (a) human AnxA1 1-21 and (b) rat AnxA1 2-26 peptides. The pair of lipid molecules shown in the bottom is shown for orientation.

	Scattering length (10^{-13} cm)	Position (Å)	Width (Å)
Human AnxA1 1-21	1.24	19.05	9.42
Rat AnxA1 2-26	1.29	19.36	8.56

Table 5-3 Parameters of the Gaussian fits of the peptide difference profiles in reciprocal space. The position is expressed as the distance from the centre of the bilayer. Width is the full-width at half height of the fitted Gaussian distribution.

The water distribution in the stacked bilayer system was obtained by subtracting the scattering profile at 8% ^2H_2O from that at 25 % ^2H_2O sample hydration. Figure 5-4 shows the water distribution profiles in the pure lipid bilayer and in the presence of human AnxA1 1-21 and rat AnxA1 2-26. The split peaks at the ends of the figure (can be seen as a single peak for continuous extension of unit cells) represent the water between two adjacent lipid bilayers. The three difference profiles are very similar to each other, apart from minor features in the lipid core region, in the two peptide-containing samples. In order to determine whether or not these are artifactual, Gaussian peaks were fitted in reciprocal space. The results, shown in Table 5-4, clearly indicate that the features at 10 – 11 Å are real, though a minor component, accounting for only 1 – 1.5% of the total water. The peak located at the bilayer centre (at $Z = 0$) does not fit to a Gaussian (in reciprocal space fitting), indicating that it results from termination error. The minor peaks are readily explained in terms of exchanged protons on the hydrophobic surface of the amphipathic α-helix bound parallel to the bilayer surface and the deuterium atoms on the hydrophobic face caused by hydrogen/deuterium exchange from solvent leading to higher scattering length (*131, 132*). However, the minor peaks shown here cannot be explained by a transmembrane model where the peptide forms a channel-like structure, lying perpendicularly to the bilayer, and ^2H_2O diffuses freely through the bilayer (*133*). The perpendicular insertion model should appear as a continuous bulge across the bilayer.

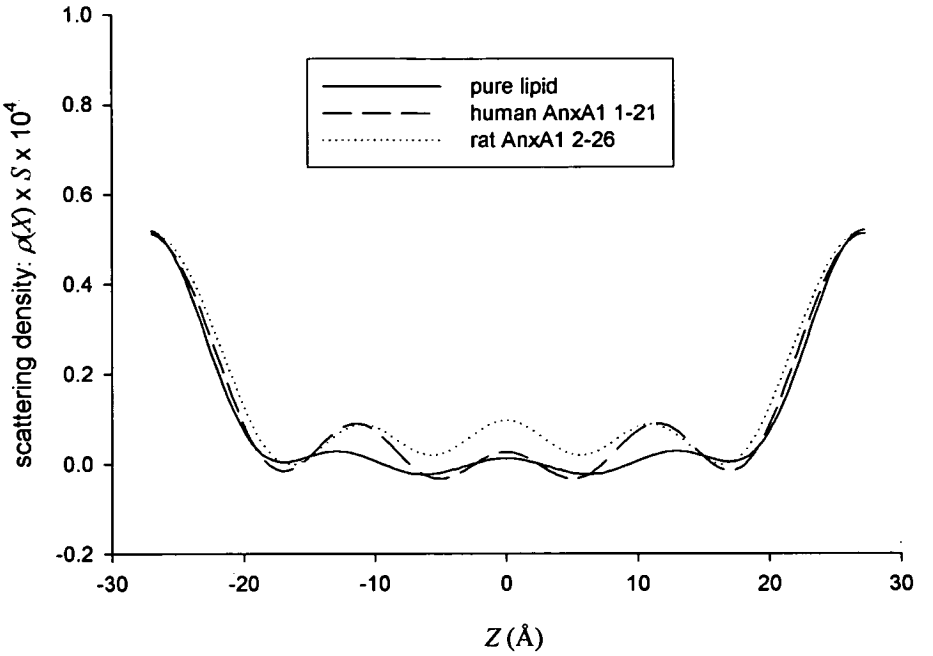

Figure 5-4 Water distribution profiles of DMPC/DMPS (mol 3:1) in the presence and absence of human AnxA1 1-21 peptide.

	Scattering length (10^{-13} cm)	Position (Å)	Width (Å)
Pure lipid	2.35	25.17	7.06
Human AnxA1 1-21			
1st Gaussian	2.75	25.05	7.18
2nd Gaussian	0.37	11.64	5.46
(Peak difference)		(13.41)	
Rat AnxA1 2-26			
1st Gaussian	2.46	24.76	8.26
2nd Gaussian	0.25	10.66	5.32
(Peak difference)		(14.1)	

Table 5-4 Parameters of the Gaussian fits of the water distribution in reciprocal space. The position is expressed as the distance from the centre of the bilayer. Width is the full-width at half height of the fitted Gaussian distribution.

Using the data in Table 5-3 and Table 5-4, and taking the bilayer centre as the origin, a straightforward calculation shows that the peptide peaks (full-width at half height) span from 14.34 – 23.76 Å (human) and 15.08 – 23.64 Å (rat). Similarly, the inner edges of water at half height lie at 21.46 Å (human) and 20.63 Å (rat). This means that each of the peptides lies in a region of steep hydrophobic gradient, ranging from the alkyl chains to the solvated headgroups, similar to other amphipathic α-helical peptides (*100, 134*). Although the outer edge of each peptide lies at a similar depth in the bilayer (23.76 Å and 23.64 Å for human and rat, respectively), it should be noted that the width of human AnxA1 1-21 peptide (9.42 Å) is larger than rat AnxA1 2-26 (8.56 Å). The X-ray structure of porcine AnxA1 in the absence of Ca^{2+} (*11*) shows that the N-terminal helical domain has a kink at Glu17. The human AnxA1 1-21 peptide has identical sequence compared to the porcine counterpart except the residue for Asp17. If it is assumed that the human AnxA1 peptide also adopts similar folding to the porcine protein, then this would explain its greater width in neutron scattering profiles.

The neutron diffraction experiments of multilamellar phospholipid containing full-length human AnxA1 protein were conducted using the V1 instrument at HMI, Berlin. The *d*-spacing of the full-length protein-containing sample, at 92% relative humidity, is 69.35 Å, which is much wider than that of the pure lipid sample which has a *d*-spacing of 58.28 Å. Table 5-5 shows the structure factors of the bilayer mixed with full-length AnxA1 in 8% and 25% ^2H_2O. The structure factor $F(4)$ for 8% ^2H_2O and $F(3)$ for 25% ^2H_2O are not detectable. Bragg peaks are less intense in comparison to data collected in chloroform:methanol mixture dispersion (see Table 5-2). Because the samples prepared here are dissolved in aqueous buffer, one can speculate that the phospholipid molecules are packed in a less order format, compared to samples prepared in organic solvent. Therefore, the less orderly-packed bilayer stacks attenuate the neutron diffraction. Additionally, an increase in mosaic spread upon full-

length protein addition was observed by rocking curve analysis (data not shown), indicating that the protein disrupts the lattice orientation in the multilamellar bilayer system. The phase angles are not properly assigned due to missing of structure factors at certain orders of diffraction, which makes it difficult to fit a continuous transform. A lack of fine structure information derived from the high diffraction orders means that the position of the phospholipid bilayer in the neutron scattering profile remains elusive.

	F(1)	*F*(2)	*F*(3)	*F*(4)	*F*(5)
8 % ^2H_2O	0.570	-0.586	NA	-0.171	0.086
25 % ^2H_2O	1.376	-0.749	0.090	-0.050	NA

Table 5-5 Neutron structure factors *F*(*h*) of full-length human AnxA1 in bilayers of DMPC/DMPS (mol 3:1). *h* stands for the diffraction order. Data were collected in 8% and 25% ^2H_2O mixture collected at 92% relative humidity, 30 °C.

5.4.2 Small angle neutron scattering

Figure 5-5a shows SANS data for deuterated d54-DMPC:DMPS MLVs (mol 3:1) with and without addition of full-length human AnxA1, in the presence of 2 mM Ca^{2+} at pH 8.0. For pure lipid MLV, the Bragg peak is positioned at $Q = 0.033$ A^{-1}. Addition of protein shifts the Bragg peak to a higher Q value of 0.043 A^{-1}. Thus, the *d*-spacing for pure lipid MLVs is 190 Å, whereas the spacing shrinks to 146 Å in the presence of AnxA1 (Table 5-6), suggesting membrane bilayers in the multilamellar vesicle system are more compact in the presence of Ca^{2+} and AnxA1. To evaluate the effects of the AnxA1 N-terminal domain on the *d*-spacing of multilamellar vesicles, rat AnxA1 N-terminal peptide 2-26 was monitored using normal DMPC:DMPS MLVs (mol 3:1). Figure 5-5b reveals that the Bragg peaks remain almost the same, in the presence and absence of the peptide, and *d*-spacings for MLVs in the presence and absence of the peptide are 233 Å and 217 Å, respectively (Table 5-6). The results reveal that rat AnxA1 2-26 peptide cannot induce membrane aggregation. Instead, the increase in *d*-spacing implies a membrane surface interaction requiring extra room in the water area, in the multilamellar bilayer system, to accommodate the peptides.

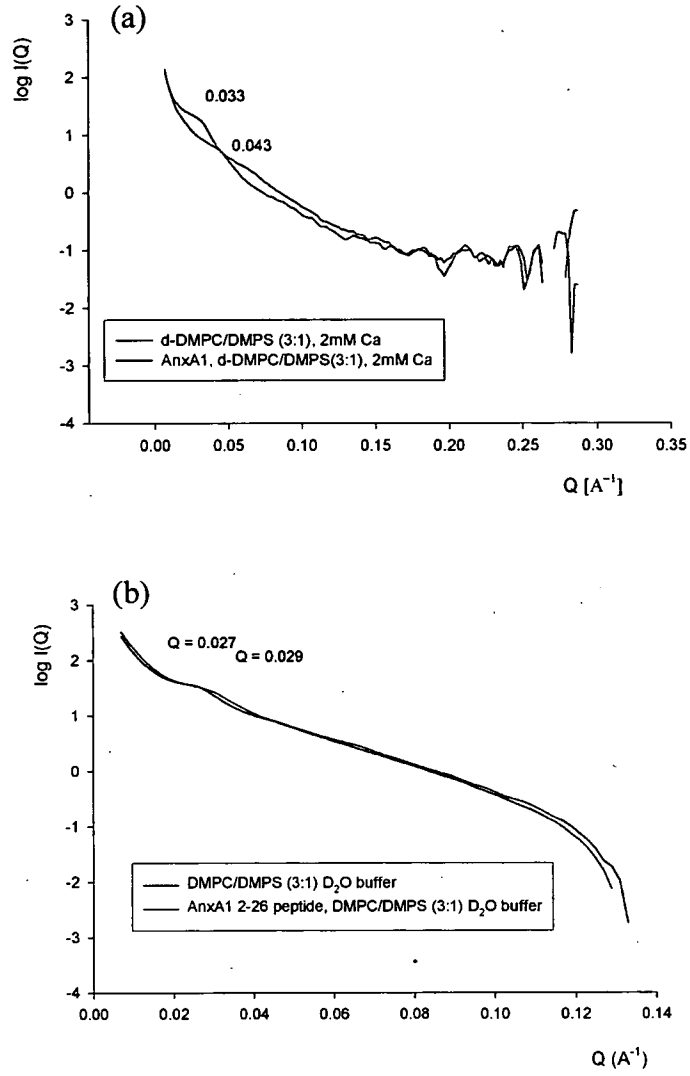

Figure 5-5 The dependence of SANS intensity *I(Q)* on the scattering *Q* for DMPC/DMPS (3:1) liposomes in the presence and absence of (a) full-length AnxA1 and (b) AnxA1 N-terminal peptide, AnxA1 2-26.

Sample	Q (Å^{-1})	*d*-spacing(Å)
d-DMPC/DMPS (3:1), 2 mM Ca^{2+}, H_2O buffer	0.033	190
d-DMPC/DMPS (3:1), 2 mM Ca^{2+}, H_2O buffer, AnxA1	0.043	146
DMPC/DMPS (3:1) D_2O buffer	0.029	217
DMPC/DMPS (3:1) D_2O buffer, rat AnxA1 2-26	0.027	233

Table 5-6 The effects of full-length human AnxA1 and rat AnxA1 N-terminal peptide, AnxA1 2-26, on the positions of the Bragg diffraction peaks (Q) and their converted lattice distances (d).

5.5 Discussion

An NMR study has shown that residues from Val4 to Glu19 of the human AnxA1 2-26 peptide adopt a mainly α-helical conformation in a membrane-mimetic system (*75*). The peptide adopts an amphipathic structure at its N-terminal end (Val4 to Trp12) and forms a hydrophobic cluster ranging from Ala11 to Ile14. Although the interactions between the peptide and the membrane mimic are not well-defined, the authors proposed that membranes help the refolding and stabilisation of the α-helical structure of the AnxA1 N-terminal peptide. Another study using X-ray crystallography showed a structure of the complex of human AnxA1 2-15 peptide and S100A11, which is an E-F hand calcium binding protein (*106*). The peptide adopts an amphipathic helix conformation and the hydrophobic residues of the peptide, are buried within the complex, in contact with the C-terminal helix of S100A11. The hydrophilic residues are involved in the hydrogen-bond with the N-terminal helix of S100A11. The two structural studies have clearly characterised that (1) the human AnxA1 N-terminal peptides adopt an α-helical conformation in the presence of membranes or a binding partner, and (2) the folding into α-helix of the peptides enables them to present an amphipathic feature. These observations support our hypothesis that human AnxA1 1-21 peptide lies parallel to the surface of lipid bilayer. The interfacial position of the peptides in the bilayer system, as inferred from our neutron diffraction data, also upholds the role of the N-terminal domain of AnxA1 in membrane binding.

Although little is known about the membrane-binding ability of the rat AnxA1 N-terminal domain, the rat AnxA1 N-terminal peptide does exhibit a similar behaviour to the human counterpart in refolding and membrane binding. The CD spectrum profiles (Figure 4-4) and monolayer lateral surface pressure measurements (Figure 4-1) show that the rat AnxA1 N-terminal peptide can interact with the phospholipid monolayer in the absence Ca^{2+}, and forms an α-helical conformation in the presence of vesicle. The neutron scattering

experiments also demonstrated that the rat AnxA1 2-26 peptide adopts a very similar membrane binding orientation compared to the human AnxA1 1-21 peptide.

It has been suggested that the N-terminal tail of AnxA1 serves as a second membrane-binding domain (*74, 118*). The neutron scattering maps clearly show that the peptides lie parallel to the membrane surface at a shallow depth, which is supported by the amphipathic feature of the two peptides, presented as a two-dimensional axial projection (Figure 5-6). Furthermore, the AnxA1 N-terminal peptides can induce surface pressure increases of phospholipid monolayer in the absence of Ca^{2+} (Figure 4-1). It is therefore presumed that the hydrophobic side of the α-helix inserts the membrane, and causes surface pressure increases. One review paper proposed that amphipathic peptides are involved in reversible membrane association (*135*). The copelleting assay (Figure 4-9) shows that approximately 80% of membrane-bound AnxA1 can be recovered after addition of excess EDTA, whereas 17% of protein can not. Assuming that AnxA1 adopts a monomeric conformation in mediation of membrane aggregation, the N-termini serve as the secondary membrane binding site. The reversibility of amphipathic peptides accounts for the fact that the membrane-bound N-terminal domain of AnxA1 may dissociate from the membrane, upon Ca^{2+} ion chelation at the primary binding site. Although there is no direct evidence to conclude the mechanism of membrane aggregation mediated by AnxA1, the neutron scattering profiles indicate a direct interaction with membrane, and seem to satisfy the membrane aggregation model A (Figure 1-2).

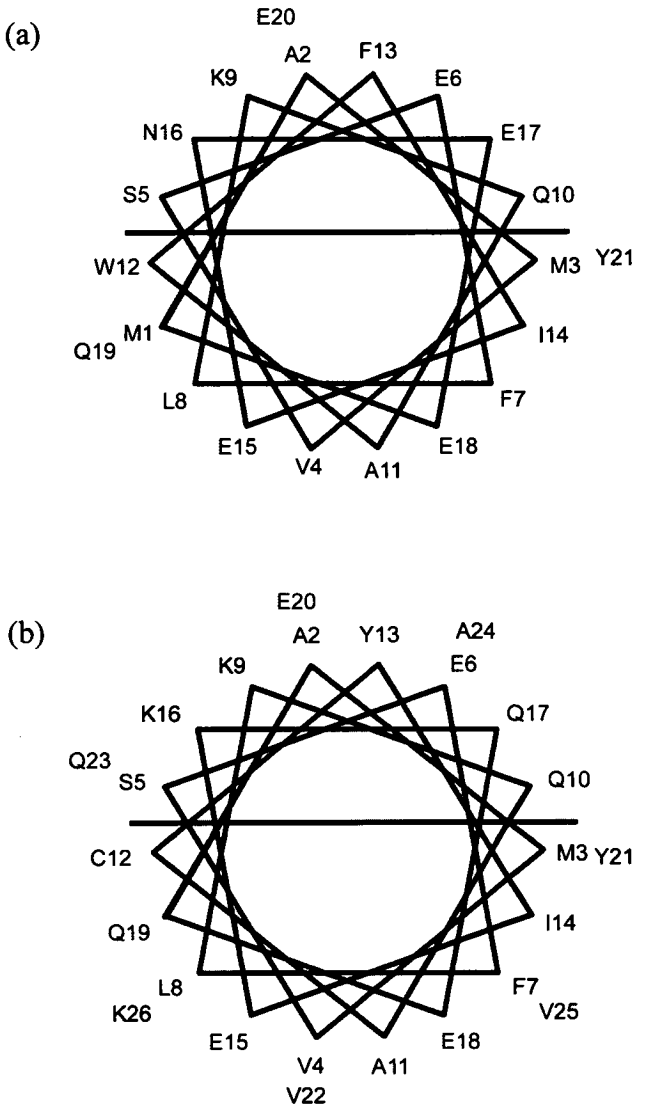

Figure 5-6 Helical wheel presentation of the N-terminal domains of (a) human and (b) rat AnxA1 showing the amphipathic character of the α-helix. The horizontal lines indicate the separation of hydrophobic (down) and hydrophilic (up) faces. The diagrams were produced with *WinPep v3.01* (*136*).

The SANS data (Table 5-6) are in full agreement with previous knowledge that AnxA1 can mediate membrane aggregation in the presence of Ca^{2+}. Although the experiments were performed at pH 8.0, a decrease in *d*-spacing was still visible upon addition of AnxA1: from 190 Å to 146 Å. The results are also in line with the liposome turbidity measurements shown

in Figure 4-7: despite the fact that the Ca^{2+}-dependent membrane aggregation ability of AnxA1 is abolished at basic environment (pH 8.0), liposome turbidity is still detectable at high Ca^{2+} concentration (above 1 mM). The SANS experiments of full-length AnxA1 were performed in the presence of 2 mM Ca^{2+}. The Ca^{2+} concentration should allow the multiple membrane stacks to adopt an aggregation-like status. A cryo-electron microscopy observation of a liposome aggregation junction induced by AnxA1 performed at pH 7.4, show a thickness in the centre of two adjacent bilayers is 114 Å (*72*). According to the liposome turbidity assay (Figure 4-7), AnxA1 does not display its highest membrane aggregation ability at the neutral pH. Therefore, the distance observed by cryo-electron microscopy may not reflect the spacing of fully aggregated liposome induced by AnxA1.

Upon addition of rat AnxA1 2-26 peptide, the *d*-spacing of the multilayer of MLVs measured by SANS does not decrease, suggesting the AnxA1 N-terminal peptide does not possess the ability of membrane aggregation. Instead, the *d*-spacing increase slightly: from 217 to 233 Å. The expanded *d*-spacing is not observed in neutron diffraction, upon addition of the peptides (Table 5-1). The reason of this discrepancy remains unclear. It is possibly due to the more compact packing of the rehydrated multiple-stack bilayers in neutron diffraction experiments. On the other hand, MLVs are prepared in solution, allowing more flexible packing of multiple bilayers.

As mentioned in chapter 4 that the pH value might play a key role in regulating membrane aggregation. Rosengarth et al. reported that AnxA1 displayed membrane penetration at pH 6.0, in the absence of Ca^{2+}, using monolayer lateral surface pressure measurements (*73*). At pH 7.4, they found that Ca^{2+} is required to induce a similar increase in surface pressure. The calculated p*I* value of human AnxA1 is 6.62 implying that, at pH 6.0, the slightly positively-charged protein can interact with the membrane on the basis of electrostatic nature without the assistance of Ca^{2+}. On the other hand, at basic pH, AnxA1 becomes a negatively-charged

molecule and thus produces a repulsive force towards acidic phospholipids. Thus, it is assumed that the comparatively weaker membrane aggregation ability at basic pH is probably due to the fact that fewer AnxA1 monomeric molecules can bind to the membrane containing acidic phospholipid, through their C-terminal cores. As a consequence, there are fewer protein molecules with expelled N-terminal domains available to bind to the secondary membrane.

It has been reported that the membrane-binding behaviours of several annexins are affected by pH. Hoekstra and coworkers (*137*) reported that AnxA5 can induce calcium-dependent unilamellar vesicle aggregation at mildly acidic pH. They also observed the leakage of vesicle contents in the absence of Ca^{2+}, at neutral and mildly acidic pHs, which suggests a direct interaction between AnxA5 and phospholipids. Another report demonstrated that AnxA5 and AnxB12 become more hydrophobic in acidic conditions, as detected by their binding ability to a liposoluble reagent, (3-trifluoromethyl)-3-(m-iodophenyl)diazirine (TID), at pH 5.0 (*39*). At neutral pH, the proteins can not be labelled with TID. The authors presumed that a low pH gives rise to protonation of carboxylate switch residues, which leads to the insertion of the annexins into the membrane, and a corresponding conformational change to form a transmembrane ion channel. The CD measurements show that the secondary structure components of AnxA1 do not vary significantly at different pH values or Ca^{2+} concentrations (Figure 4-2), indicating that AnxA1 may have a considerably more rigid domain conformation compared to AnxA5. However, the CD experiments were performed in the absence of vesicles: whether AnxA1 will exhibit a conformational change in contact with the membrane at different pH values is as yet uncertain.

The *d*-spacing calculated by the Bragg peak in SANS profiles indicates the distance between the two adjacent membrane bilayers is 146 Å at membrane aggregated status. Therefore, one can apply different models to fit the *d*-spacing. Figure 5-7 shows several possible models of

membrane aggregation mediated by AnxA1. The *d*-spacing defines the space including two phospholipid leaflets and solvent area. The average length of DMPC and DMPS are about 27 Å. The thickness of the AnxA1 core domain is about 30 Å if it binds to the membrane using it primary binding site. It is clear shown that AnxA1 dimer (Figure 5-7a) interacting the individual N-terminal domain fits the gap very well. However, in terms of AnxA1 monomer, it does not seem to be possible if it remains a closed form (Figure 5-7b). However, it is not exclusively impossible that AnxA1 extends its N-terminal tail and contacts the second membrane (Figure 5-7c), because the length of the random coil linker between the N-terminal helix and C-terminal core is at least 32 Å calculated by the linear distance of the two ends of the linker (*11*).

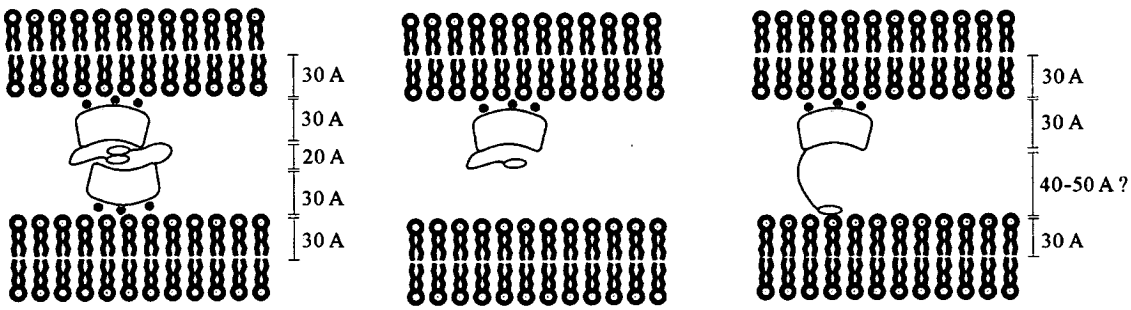

Figure 5-7 Schematic presentation of possible models of membrane aggregation induced by AnxA1. The models are proposed on the basis of the observed *d*-spacing obtained by SANS. The vertical bars flanking the models depict the lengths of the corresponding components. (a) Two AnxA1 molecules conjugated by their N-terminal domain. The dimer induces membrane aggregation via the Ca^{2+}-dependent binding sites. (b) The closed or unextended AnxA1 does not fit the observed *d*-spacing. (c) An AnxA1 monomer is likely to fit the spacing if its N-terminal domain is fully-extended.

The membrane aggregation mechanism of AnxA1 is still not well defined by the SANS measurements, because both of the models can fit the observed spacing reasonably well. The SANS data collected here was at pH 8.0. However, LOQ neutron beam time was not

sufficient to collect data at acidic pH. Whether the *d*-spacing can represent the fully-aggregated membrane stacks is not certain. Therefore, no conclusions can be confidently drawn at the current stage. However, because the *d*-spacings of MLVs can be easily calculated using the Bragg's peaks generated by SANS, the aggregation induced by AnxA1 can be monitored using that technique. A series of SANS measurements at acidic pH is therefore required to obtain the *d*-spacing at fully-aggregated status and to evaluate the possible aggregation model.

6 Membrane binding activities of plant annexins

6.1 Introduction

The Ca^{2+}-dependent membrane interaction of animal annexins has been studied for over two decades. However, the membrane binding behaviour of plant annexins is still not well understood. Sequence comparisons have shown that the canonical calcium binding motif is well conserved in repeat I in plant annexins (*23*). X-ray structures of cotton Anx(Gh1) and bell pepper Anx24(Ca32) also suggest that repeats I and IV harbour a favourable geometry for calcium coordination (*23, 24*). Interestingly, both of the plant annexins harbour well conserved aromatic and positively charged residues, stalking out of their convex surface. The sequential and structural conservation of these residues causes speculation that plant annexins might possess both Ca^{2+}-dependent and -independent membrane binding behaviour. This study aims to investigate the membrane binding behaviour of plant annexins using a liposome-based assay and monolayer lateral surface pressure measurements. The role of the aromatic and positively-charged residues of plant annexins in membrane binding and their effects on phospholipid packing upon membrane binding, were studied using differential scanning calorimetry. The work characterising the membrane binding activities of plant annexins has been published (*89*).

6.2 The mechanisms of membrane binding of plant annexins

6.2.1 Lateral surface pressure measurements of phospholipid monolayer

The membrane binding behaviour of plant annexins was characterised by surface pressure measurements, using AnxA5 as a control. Measurements with AnxA5 as reported in the present study qualitatively, agree with the results from a more detailed investigation of AnxA5 in this context, which used DMPA monolayers and different experimental parameters (*138*), they also agree with an earlier study by Mukhopadhyay and Cho (*88*). Results for the binding of 100 nM AnxA5 (1 mM $CaCl_2$) to a DMPC/DMPS (mol 3:1) monolayer exhibit an anticipated binding behaviour with an immediate onset at π_0 = 19 mN/m and π_0 = 20 mN/m (Figure 6-1D,E). Saturation level is reached after approximately 30 min, and the increase in surface pressure is $\Delta\pi$ = 3 mN/m (π_0= 19 mN/m) and $\Delta\pi$ = 2.5 mN/m (π_0 = 20 mN/m). In contrast, the increase in lateral surface pressure for His_6-Anx24(Ca32) under similar conditions (150 nM protein, 3 mM $CaCl_2$) is not significant (data not shown). However, increasing the protein concentration to 1.5 µM resulted in a binding curve albeit at a much slower rate (Figure 6-1B, C). Irrespective of the initial pressure, π_0 = 16 mN/m or π_0 = 20 mN/m, the level of saturation is only reached after approximately 85 min. However, the increase in lateral surface pressure is much more pronounced, about $\Delta\pi$ = 5 mN/m, than that observed with the AnxA5 control. Compared to the hexa-His-fusion protein, wild type annexin 24(Ca32) has a less effective membrane adsorption. While the level of saturation is reached after about 45 min, the increase in lateral surface pressure elicited by the untagged protein is only $\Delta\pi$ = 1.3 mN/m.

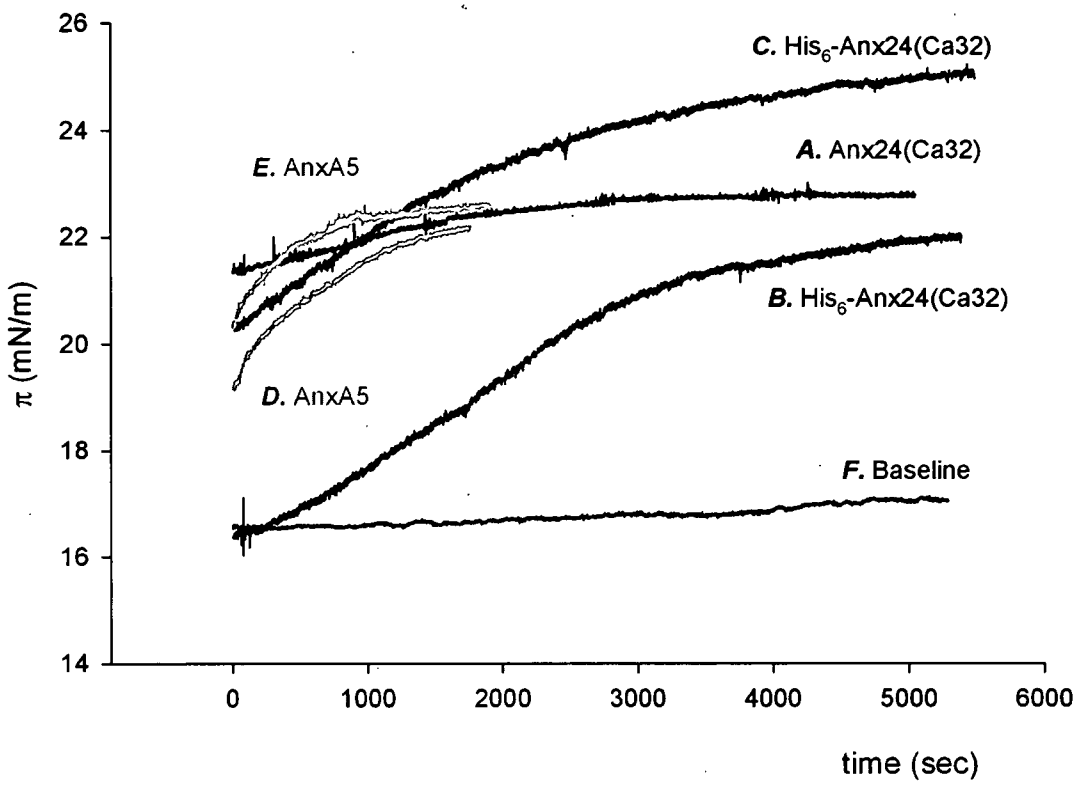

Figure 6-1 Surface film balance measurements with DMPC/DMPS (3:1) monolayers. In all experiments, the subphase contained 160 mM NaCl, 10 mM HEPES (pH= 7.4). *A* 1.5 µM Anx24(Ca32), 3 mM $CaCl_2$, π_0 = 20 mN/m. *B* 1.5 µM His_6-Anx24(Ca32), 3 mM $CaCl_2$, π_0 = 16 mN/m. *C* 1.5 µM His_6-Anx24(Ca32), 3 mM $CaCl_2$, π_0 = 20 mN/m. *D* 100 nM AnxA5, 1 mM $CaCl_2$, π_0 = 19 mN/m. *E* 100 nM AnxA5, 1 mM $CaCl_2$, π_0 = 20 mN/m. *F* Control experiment without protein, π_0 = 16 mN/m.

6.2.2 Copelleting assay

As shown in Figure 6-2a (and also in Table 6-1), the His-tagged wild type plant annexins display a calcium-dependent membrane binding behaviour with $c_{1/2}(Ca^{2+})$ 0.03 – 0.1 mM using PC/PS (3:1) vesicles. The range is on the high side compared to that for mammalian annexins (0.6 µM - 0.3 mM, (*47*)). In contrast to mammalian annexins, about 20% of His-tagged and untagged wild type plant annexins bind to the lipid vesicles even in the absence of calcium. This calcium-independent membrane binding differs significantly from the

behaviour of the mammalian orthologues. Qualitatively, this behaviour is also observed from the preparation of untagged plant annexins using the liposome-affinity protocol (Figure 2-7), as a fraction of the protein can not be released even in the presence of an excess of metal chelators (EDTA and CHELEX).

Compared to His_6-Anx24(Ca32), the untagged wild type Anx24(Ca32) (Figure 6-2a dotted line) requires slightly more calcium for half-maximal membrane binding ($c_{1/2}(Ca^{2+})$ 0.7 mM). This indicates that the artificial elongation of the N-terminal domain of these plant annexins does affect their membrane binding properties to a certain extent.

To identify key residues for membrane binding, several mutant proteins with altered surface residues were tested. The mutant series was constructed with the bell pepper annexin 24 and all mutants carry the N-terminal His_6-tag. The mutant His_6-Anx24(Ca32)-W35G was subjected to the copelleting assay to elucidate the effects of the conserved tryptophan residue within repeat I. As is evident from Figure 6-2b, this mutant shows a significantly reduced calcium-dependent membrane binding activity. Furthermore, it has also lost the ability to attach to membranes in a calcium-independent manner. A double mutant, His_6-Anx24(Ca32)-W35A/W88F, originally constructed to perform fluorescence experiments using the remaining Trp107 as an intrinsic probe, was also tested in the copelleting assay and found to behave in a similar manner to His_6-Anx24(Ca32)-W35G (Figure 6-2b).

Disabling the second surface-exposed tryptophan residue, Trp107, yields a mutant with similar membrane-binding activity as W35G and W35A/W88F. All three tryptophan mutants lack calcium-independent binding ability and the saturation levels are between 50% and 70% with W107G at the high end of this range (Figure 6-2b). Other residues identified from the X-ray structures as potentially important for membrane-binding behaviour include Lys190 in repeat III, and Arg262 and Arg263 in repeat IV (Figure 6-2c). The effect of the latter

residues was investigated with a double mutant His_6-Anx24(Ca32)-R262A/R263A which displays a membrane-binding behaviour akin to that of the wild type His-tagged protein. The saturation level at 5 mM calcium is 92% as compared to 94% for His_6-Anx24(Ca32). Interestingly, the level of calcium-independent membrane-binding is about twice as high as that of the wild type protein. In contrast, changing Lys190 to glycine severely disrupts the membrane-binding activity of the protein. This mutant protein possesses the highest half-maximum calcium concentration among all the mutants tested within this study, at about 4 mM. Furthermore, the calcium-independent membrane-binding is decreased to about 10%.

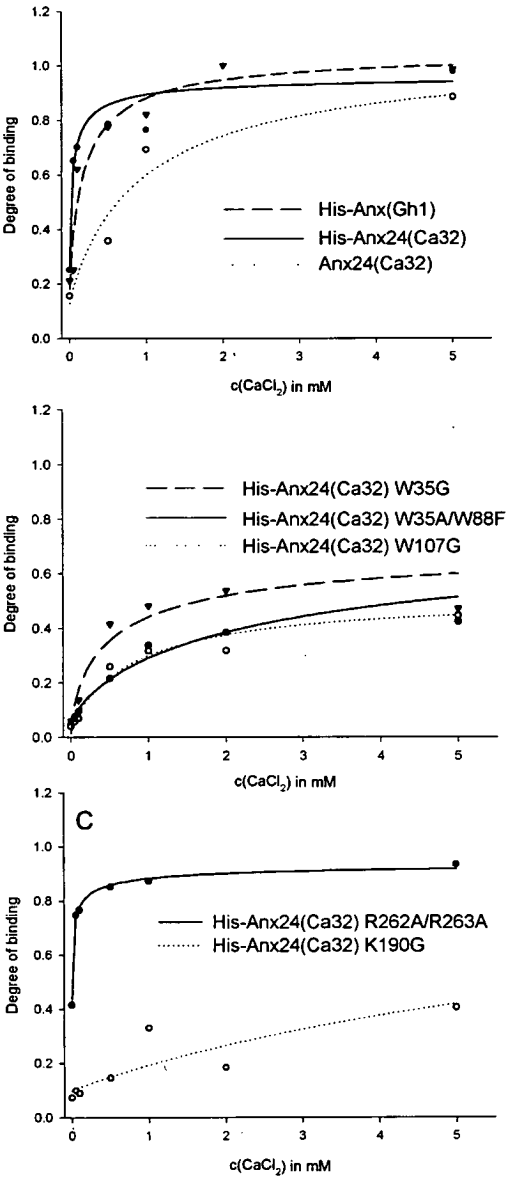

Figure 6-2 Copelleting assay of Anx24(Ca32) and Anx(Gh1). Data points represent the average of at least three independent experiments; error bars have been omitted for clarity. Data were fitted with a standard binding equation (Hill coefficient n= 1). (a) Calcium-dependent membrane-binding curves for wild type annexins: His_6-Anx24(Ca32) (closed circles, solid line), untagged Anx24(Ca32) (open circles, dotted line), His_4-Anx(Gh1) (closed triangles, dashed line). (b) Calcium-dependent membrane-binding curves for tryptophan mutant bell pepper annexins: His_6-Anx24(Ca32)-W35A/W88F (closed circles, solid line), His_6-Anx24(Ca32)-W35G (open circles, dotted line), His_6-Anx24(Ca32)-W107G (closed triangles, dashed line). (c) Calcium-dependent membrane-binding curves for basic surface residue mutants: His_6-Anx24(Ca32)-R262A/R263A (closed circles, solid line), His_6-Anx24(Ca32)-K190G (open circles, dotted line).

Protein	$c_{1/2}(Ca^{2+})$	Binding at $c(Ca^{2+})$ = 0 (%)	Maximum binding (%)
Anx24(Ca32)	0.65 mM	13	99[b]
His_6-Anx24(Ca32)	0.03 mM	27	94[a]
His_6-Anx24(Ca32)-W35A/W88F	0.4 mM	4	67[b]
His_6-Anx24(Ca32)-W35G	0.7 mM	4	53[b]
His_6-Anx24(Ca32)-W107G	0.4 mM	3	72[b]
His_6-Anx24(Ca32)-R262A/R263A	0.1 µM	42	92[a]
His_6-Anx24(Ca32)-K190G	3.9 mM	10	74[b]
His_4-Anx(Gh1)	0.11 mM	18	100[a]

[a]Determined at $[Ca^{2+}]$ = 5 mM. [b]Determined at $[Ca^{2+}]$ = 20 mM.

Table 6-1 Results of copelleting assay of plant annexins and mutants.

6.2.3 Differential scanning calorimetry (DSC)

Since His_6-Anx24(Ca32) and His_4-Anx(Gh1) show similar membrane binding behaviour (Figure 6-2), here His_4-Anx(Gh1) is chosen as a testing model to evaluate the thermodynamic change of membrane in the presence of the plant annexin. The effects of calcium ions alone and His_4-Anx(Gh1), in the presence or absence of calcium, on phase transition temperature of DMPC/PMPS MLVs (mol 3:1) are shown as thermograms in Figure 6-3 . Transition temperatures determined by the peak maximum and peak onset are summarised in Table 6-2. The heating thermogram of DMPC/DMPS vesicles alone shows a gel to liquid crystalline phase transition at 23.7 °C (Figure 6-3a). As Ca^{2+} ions were added to the vesicle solutions, the phase transition peaks shifted to higher temperatures progressively (from 23.7 °C in the absence of Ca^{2+} to 26.5 °C in the presence of 50 mM Ca^{2+}). Thermogram peaks broaden upon Ca^{2+} addition and a shoulder positioned at about 30°C was detected in the presence of 50 mM Ca^{2+}. The phenomena are comparable with the results of

Jacobson and Papahadjopoulos, who examined the effects of bivalent cations on PS/DPPC (Dipalmitoyl-phosphatidylcholine) mixed liposomes (*139*). Adding 1.5 or 3 nmol of His_4-Anx(Gh1) to vesicles in the presence of 10 mM Ca^{2+}, caused increases of the phase transition peaks to higher temperatures, 25.8 °C, compared to the thermogram of the sample with 10 mM Ca^{2+} only (24.5 °C) (Figure 6-3b). The DSC profile reveals a shoulder in the presence of 1.5 nmol protein. The shoulder became more pronounced when the amount of protein was doubled. Interestingly, in the absence of Ca^{2+}, adding His_4-Anx(Gh1) produced an opposite effect on phase transition temperature. The transition temperature did not change significantly upon 1.5 nmol His_4-Anx(Gh1) addition, but a visible decrease in transition temperature (ΔT_m = 0.4 K) was observed in the presence of 3 nmol His_4-Anx(Gh1) in the absence of Ca^{2+} (Figure 6-3c).

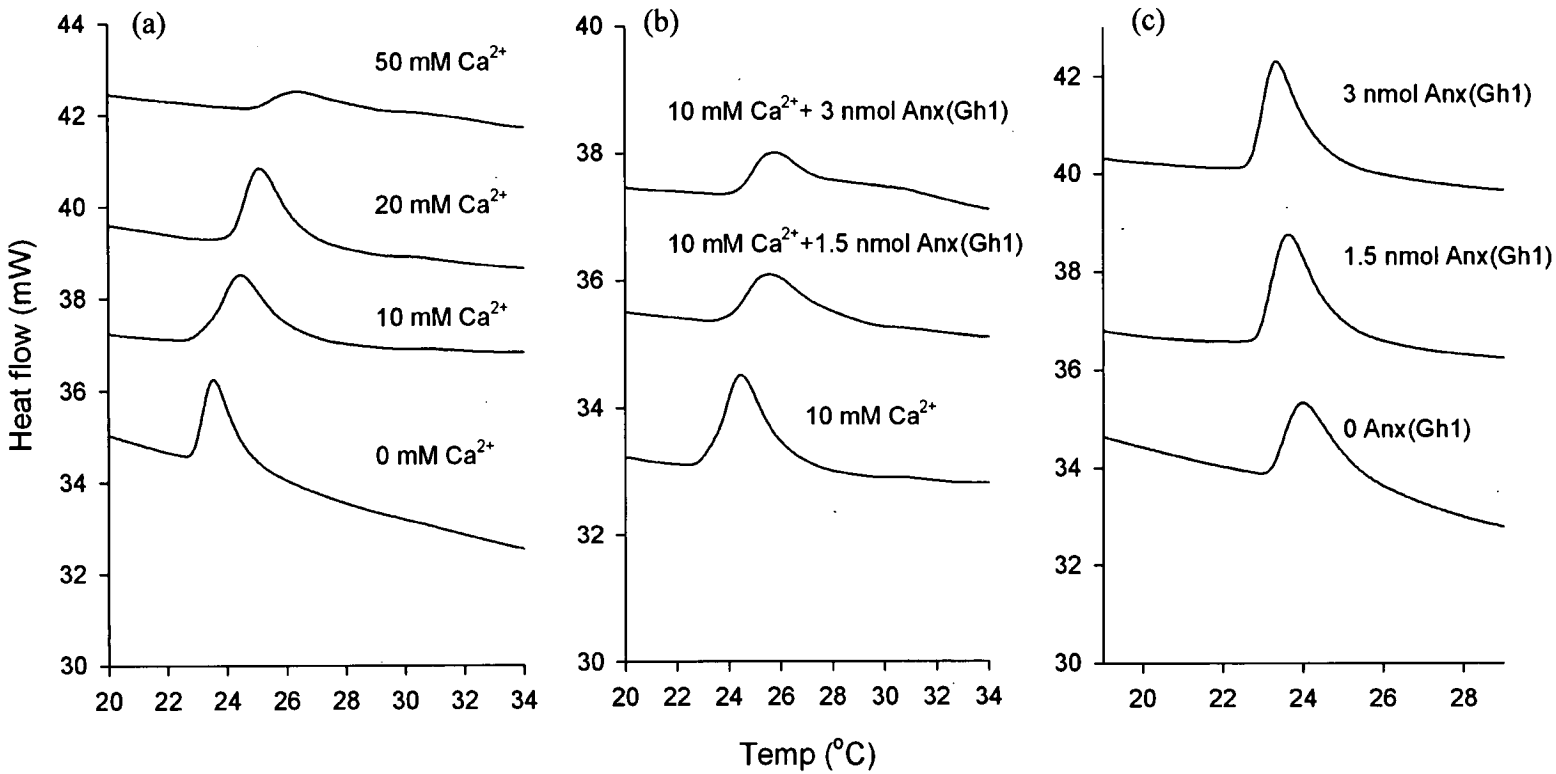

Figure 6-3 Differential scanning calorimetry thermograms show the change of gel to liquid-crystalline transition temperature of DMPC/DMPS (mol 3:1) MLVs. From lower to upper traces: (a) MLVs at different concentrations of Ca^{2+} (0, 10, 20 and 50 mM). (b) MLVs at different amounts of His_4-Anx(Gh1) (0, 1.5 and 3 nmol) in the presence of 10 mM Ca^{2+}. (c) MLVs at different amounts of His_4-Anx(Gh1) (0, 1.5 and 3 nmol) in the absence of Ca^{2+}.

	Liposome (25mg/ml)	Liposome (25mg/ml) + Ca^{2+}			Liposome (25mg/ml) + Ca^{2+} (10 mM) + His_4-Anx(Gh1)		Liposome (25mg/ml) + His_4-Anx(Gh1)	
		10 mM	20 mM	50 mM	1.5 nmol	3.0 nmol	1.5 nmol	3.0 nmol
onset (°C)	23.0	23.3	24.3	25.0	24.2	24.4	23.1	22.9
peak (°C)	23.7	24.5	25.4	26.5	25.8	25.8	23.8	23.5

Table 6-2 Effect of Ca^{2+}, His_4-Anx(Gh1) (with 10mM Ca^{2+} or without Ca^{2+}) concentrations on the phase transition temperature of DMPC/DMPS (mol 3:1) liposomes.

6.3 Discussion

From the results of the present investigation, it is evident that the membrane binding behaviour of plant annexins is indeed very different from that of their mammalian counterparts. The comparison of the Langmuir surface film balance measurements for bell pepper Anx24(Ca32) and human AnxA5, reveals that for comparable calcium concentrations, a lot more plant protein is required to elicit a similar increase in the lateral surface pressure. At the same time, the adsorption kinetics indicate a much slower association of the plant protein.

It is clearly noted that a major part of this study has been conducted with N-terminally His-tagged annexin proteins. A comparison of the membrane binding behaviour of the His-fusion proteins with their wild-type counterparts reveals that the N-terminal modification does affect the membrane-binding behaviour quantitatively. This is evident from the half-maximum calcium concentrations, which are one order of magnitude lower for the fusion proteins (Table 6-1), as

well as from the lateral surface pressure measurements, which show a four fold increase (Figure 6-1). At the same time, wild type and fusion proteins qualitatively show the same binding behaviour with similar features, distinct from those of the non-plant annexins. With respect to the identification of critical surface residues, therefore, the results obtained with His-tagged annexin 24 mutants may be extrapolated to be valid for the untagged protein. Nevertheless, the N-terminal domain of plant annexins plays an important role with respect to membrane interaction, similar to the phenomenon observed with mammalian annexins (*140-142*).

In contrast to their mammalian counterparts, the two plant proteins investigated in this study have the distinct property of binding with their C-terminal cores to acidic phospholipid membranes, in the absence of calcium, at neutral pH. This calcium-independent binding is severely impaired when Lys190 is replaced by glycine, and is completely abolished when either Trp35 or Trp107 are disabled. Therefore, it is most likely that the concerted action of (at least) these three surface-exposed residues is responsible for the calcium-independent membrane binding. Importantly, while Trp35 and Lys190 are strictly conserved, Trp107 is conserved in most, but not all, plant annexins. One could therefore speculate that plant annexins lacking this residue possess a reduced calcium-independent membrane-binding activity, although this hypothesis awaits experimental proof. In this context, a second aspect seems to merit some consideration. The maximum degree of binding, as estimated from the level of saturation, is much lower for mutants W35G, W35A/W88F, W107G and K190G than for the wild type annexin 24. This suggests that the calcium-independent binding is essential for the calcium-dependent binding of these proteins. Since annexin-membrane binding has been described to be highly sequential and displays cooperativity with respect to calcium (*143, 144*), it is difficult to resolve the exact order of events in the membrane-bound state. However, this study undoubtedly

reveals two different binding modes for the tested plant annexins, a calcium-independent and a calcium-dependent mode, which are probably interconnected. The situation is further complicated by the existence of plant annexin oligomers in solution (*145*) which will affect the equilibrium between the soluble and membrane-bound states.

The calcium requirements for membrane binding observed in the present study are rather high and thus separate the tested plant annexins from other members in the plant annexin family whose membrane interactions seem to be affected by nanomolar concentrations of calcium (*146*). Notably, these latter experiments have been carried out in intact plant cells. The K190G mutant differs significantly in the calcium-dependent binding behaviour, as its half-maximum calcium concentration is one order of magnitude higher than that of the other proteins tested. Since Lys190 is not directly involved in any calcium-binding event, we believe that this effect is either due to the interplay of conformations on the convex surface, or an involvement of this residue in protein-protein interactions that might also affect the calcium-binding ability.

Based on the crystal structure, a role for residues Arg262 and Arg263 in membrane binding has been anticipated, but results from this study indicate otherwise. The double mutant R262A/R263A has a membrane-binding behaviour qualitatively similar to the wild type molecule. However, the level of calcium-independent membrane binding is twice as high as that of the wild type protein and the half-maximal calcium concentration is decreased by three orders of magnitude. With respect to calcium-dependent binding, the presence of two positively charged residues presents a repelling force that may restrict the binding of a calcium ion in the IVAB loop. This scenario adds to the fact that the IVAB loop is also capable of coordinating a calcium ion. It remains unclear at this point why the calcium-independent binding of this mutant

is enhanced, since a rather favourable interaction of the arginine side chains with either the phospholipid head groups or the glycerol backbone of the lipid membrane is lost in the mutant. One can speculate that the two arginine residues could be involved in protein-protein interactions and their mutation might give rise to a functionally different moeity, which interacts with membrane surfaces more readily than the wild type molecule. The hypothesis merits particular attention, since plant annexins exist as multiple oligomeric species in solution (*145*) and Daley et al., unpublished data. Also, in contrast to the other wild type and mutant proteins tested in this study, the R262A/R263A mutant readily forms high-molecular weight aggregates (Daley & Hofmann, unpublished result). Therefore, the binding of this protein to membrane vesicles might be enhanced by non-specific interactions, due to the size of the aggregates. It is obvious from the crystal structure of annexin 24 (*23*) that Arg262 and Arg263 are located in a positive patch on the convex surface of repeat IV which apparently regulates annexin-annexin repulsion.

Differential scanning calorimetry (DSC) was used to measure the thermodynamic stability of multilamellar vesicles and to study the effects of His_4-Anx(Gh1) membrane binding on phospholipid molecule packing. The DSC measurements of DMPC/DMPS (mol 3:1) MLVs at different Ca^{2+} concentrations (Figure 6-3a) are in good agreement with previously published data, which show that a broadened peak, or two separate peaks on DSC thermogram, produced upon Ca^{2+} addition to PS/DPPC mixed vesicles (*139*). This suggests that Ca^{2+} ions would induce phase separation in mixed lipid vesicles. The authors postulated that the phase separation was caused by the segregated PS domain, induced by the presence of Ca^{2+} ions. The transition temperatures for DMPC and DMPS, are 23 °C and 35 °C, respectively. The DSC data show a shoulder positioned at 30 °C, in the presence 50 mM Ca^{2+}, accounting for the formation of the DMPS-

Ca^{2+} domain. Phase separation of mixed vesicle induced by Ca^{2+} has been widely studied using various biophysical techniques (*147-150*), and the cluster of acidic phospholipids is believed to be stabilised by electrostatic interactions with bivalent ions. After addition of His_4-Anx(Gh1), in the presence of 10 mM Ca^{2+}, the shoulder becomes more noticeable in comparison to liposomes at 10 mM Ca^{2+} (Figure 6-3b). This indicates that the protein molecules favour the formation of a segregated DMPS domain. It is speculated that membrane-bound His_4-Anx(Gh1), via its canonical Ca^{2+}-binding site on the convex surface, is involved in the stabilisation of the acidic phospholipid domain and thus promotes the phase separation.

In contrast, in the absence of Ca^{2+}, His_4-Anx(Gh1) shows a different effect on the transition temperature of the liposome. A moderate shift of the transition peak to lower temperature (0.2°C), was detected when the lipid to protein ratio is 370:1 (Figure 6-3c), indicating that His_4-Anx(Gh1) perturbs the packing of phospholipid molecules and increases the fluidity of the membrane. A similar effect was also discovered from a DSC study on a membrane-active insecticide containing a hydrophobic ester group (*151*). Although a reduction in transition temperature of the mixed vesicle was observed, incorporation of His_4-Anx(Gh1) in the absence of Ca^{2+} did not broaden the thermogram peak. This is probably because the scattering hydrophobic residues on the convex surface do not totally agitate the packing order of the phospholipids. Additionally, the positively-charged residues interacting with the head groups of acidic phospholipids may not reach the hydrophobic core of the membrane.

Like Anx24(Ca32), Anx(Gh1) shows both Ca^{2+}-dependent and -independent membrane association (Figure 6-2a). Differential scanning calorimetry profiles for the DMPC/DMPS mixed MLVs with His_4-Anx(Gh1) in the presence and absence of Ca^{2+} ions, provide solid evidence of

the twofold membrane-binding behaviours of plant annexins. Lateral surface pressure measurements also show that plant annexins exhibit distinct membrane interaction kinetics compared to animal annexins, suggesting that the protein family displays evolutional differences in both structural and functional aspects.

7 X-ray structure of cotton Anx(Gh1) in a calcium-bound state

7.1 Introduction

The structures of a number of annexins in a Ca^{2+}-bound state have been solved in the past two decades. The three-dimensional data provide valuable information of Ca^{2+}-dependent membrane binding activity of annexins. The geometry of Ca^{2+}- coordination and the types of binding sites (type II, III, AB' and IIIb) observed in annexins are summarised in Appendix.

Although plant annexins possess a different membrane binding behaviour than their animal orthologues, Ca^{2+} ions do play a role in the membrane interaction of plant annexins. Sequence alignments reveal that plant annexins might contain Ca^{2+}-binding sites similar to animal annexins in IAB and IVAB loops (*23*). The structures of Ca^{2+}-free bell pepper Anx24(Ca32) and cotton Anx(Gh1) showing a favourable Ca^{2+}-binding geometry in IAB loop (Figure 1-4) (*23, 24*). In order to characterise the effect of Ca^{2+} binding on plant annexins at atomic level, structural data in a Ca^{2+}-bound state is essential. Here, His_4-tag fusion Anx(Gh1) was used to study Ca^{2+} binding affinity and binding sites of the annexins in plant kingdom. Isothermal titration calorimetry was conducted to study the Ca^{2+} binding affinity of Anx(Gh1) in the presence and absence of membrane. The three-dimensional crystal structure of Ca^{2+}-bound Anx(Gh1) has been determined to visualise the calcium coordination in membrane-binding loops. The solved structure was compared with the Ca^{2+}-free Anx(Gh1) to evaluate the conformational changes after Ca^{2+} absorption.

7.2 Isothermal titration calorimetry (ITC)

First of all, the association of Ca^{2+} ions with cotton His_4-Anx(Gh1) in the absence of SUVs was studied using ITC. A control measurement was performed by injecting 5 mM Ca^{2+} into the sample cell containing no His_4-Anx(Gh1), in order to monitor the heat change caused by Ca^{2+} dilution. Control measurement shows a ITC profile with similar magnitude of heat change compared with the data measured in the presence of 75 μM His_4-Anx(Gh1) (Figure 7-1a, upper panel). Subtraction of control and sample data produced a thermodynamic profile of His_4-Anx(Gh1) upon addition of Ca^{2+}. The subtracted profile shows an almost unchanged heat change (Figure 7-1a, lower panel), indicating a low Ca^{2+} affinity of His_4-Anx(Gh1) in the membrane-free environment. Binding stoichiometry and dissociation constant of His_4-Anx(Gh1) and Ca^{2+} ions in the absence of phospholipid vesicles were not available due to the low affinity. The results are in good agreement with the well-known phenomenon of the low affinity of animal annexins for Ca^{2+} in the absence of vesicles (*152, 153*).

For measuring the Ca^{2+} binding behaviour of His_4-Anx(Gh1) in the presence of vesicles, a control experiment was performed by titrating DMPC/DMPS (mol 3:1) SUVs with Ca^{2+} in the absence of His_4-Anx(Gh1). Downward spikes were observed indicating an exothermic reaction after each titration event (upper trace in upper panel, Figure 7-1b). The enthalpy changes caused by interaction between Ca^{2+} ions and anionic phospholipid-containing vesicles can be compared with existing literatures (*152, 154*), where exothermic reaction is reported when Ca^{2+} ions are titrated into POPC/POPG SUVs. Sample data were obtained by titration of 5 mM Ca^{2+} into a cell containing 25 μM His_4-Anx(Gh1) and SUVs. Larger downward spikes were detected throughout the titration process (lower trace in upper panel, Figure 7-1b). Heat releases for sample and control data were calculated by integrating each titration spike. The enthalpy change was

obtained by subtracting the control from the sample data. The subtracted heat release was plotted as a function of molar ratio of Ca^{2+} to His_4-Anx(Gh1). The best fit was obtained by a model of one set of binding sites (lower panel of Figure 7-1b). Analysis of the His_4-Anx(Gh1) titration with Ca^{2+} shows a stoichiometry of 4.35 ± 0.154 mol of Ca^{2+} bound per mol of His_4-Anx(Gh1) monomer. ΔH for the formation of the ternary complex, vesicle-Ca^{2+}-His_4-Anx(Gh1), is -23.5 ± 1.2 kcal/mol. The dissociation constant K_d for His_4-Anx(Gh1) association with Ca^{2+} in the presence of vesicles is 11.01 μM. The *c* value for the ITC profile is 9.08, which is near the lower edge of the experimental window (see chapter 3.8). The results indicates that the association between His_4-Anx(Gh1) and Ca^{2+} becomes pronounced only in the presence of phospholipids.

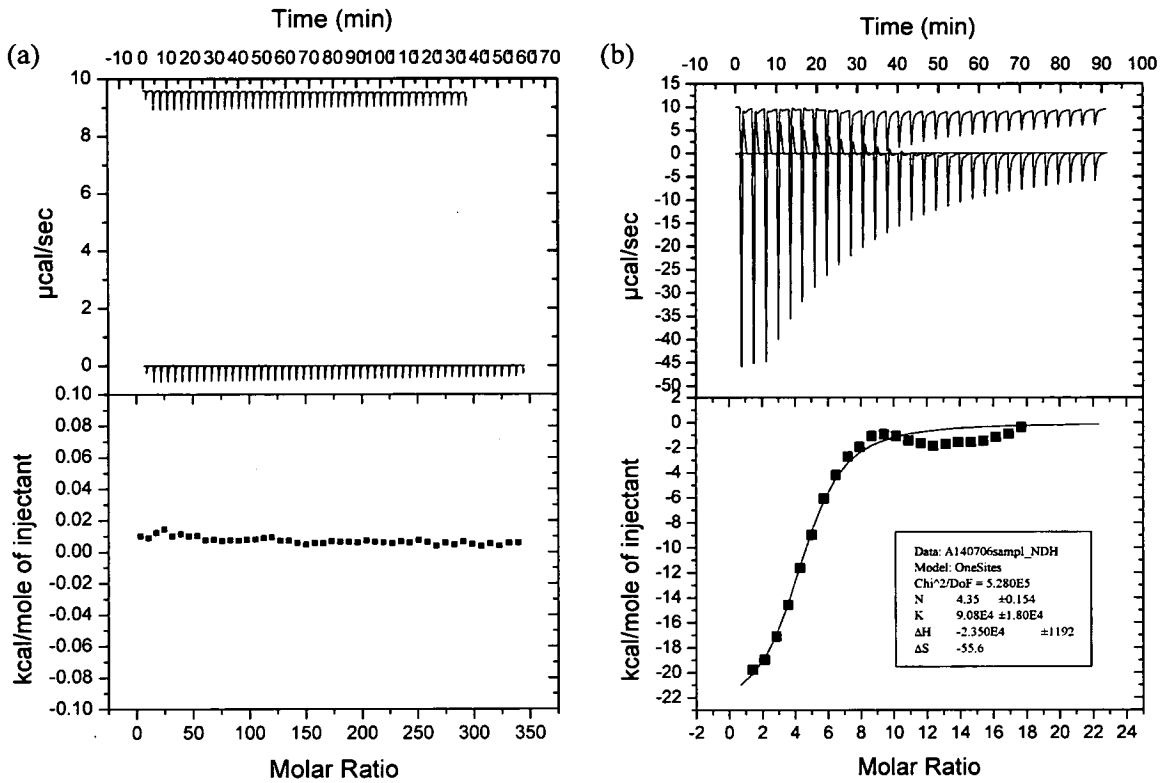

Figure 7-1 Isothermal calorimetric titration profiles of His_4-Anx(Gh1) with $CaCl_2$ in the absence of SUVs (a), and presence of SUVs (b), as described in Materials and Methods. Each titration event consisted of 5 µl addition. (a) 75 µM of His_4-Anx(Gh1) titrated with 5 mM Ca^{2+}. (b) 25 µM of His_4-Anx(Gh1) in the DMPC/DMPS (mol 3:1) vesicle-containing solution titrated with 5 mM Ca^{2+}. Ca^{2+} affinity parameters are shown in the inset box.

7.3 X-ray crystallography of Ca^{2+}-bound Anx(Gh1)

7.3.1 Protein crystallisation

Protein crystals of His_4-Anx(Gh1) in the presence of Ca^{2+} ions were obtained by mixing purified His_4-Anx(Gh1) with an appropriate concentration of $CaCl_2$. Initial cocrystallisation trials of His_4-Anx(Gh1) with Ca^{2+} used the crystallisation conditions (1.7 M $(NH_4)_2SO_4$, 0.1 M HEPES, pH 7.0) which had been reported to produce native Anx(Gh1) crystals (*24*). A fine grid search around these conditions was conduct by adjusting the concentration of $(NH_4)_2SO_4$ and buffer pH. Additionally, crystals of native His_4-Anx(Gh1) have been produced to perform soaking in mother liquor in the presence of 10-30 mM Ca^{2+}. As $CaCl_2$ and $(NH_4)_2SO_4$ form insoluble $CaSO_4$ when the concentration of added $CaCl_2$ reaches 30 mM, subsequent cocrystallisation trials with higher Ca^{2+} concentration (50 mM and 100 mM) were performed using in-house screening buffers containing no $(NH_4)_2SO_4$. Crystals were grown using the hanging-drop vapour-diffusion method. 25 mg/ml of His_4-Anx(Gh1) was mixed with $CaCl_2$ stock solution in a ratio of 4:1 (v/v). Droplets consisted of 2 µl of protein solution containing $CaCl_2$ and 2 µl of reservoir solution, equilibrated against 300 µl reservoir solution at 290 K. Crystals were obtained after four weeks. The crystallisation conditions and $CaCl_2$ concentrations that produced crystals, from which datasets were eventually collected, are summarised in Table 7-1. At low concentrations of Ca^{2+}, the crystal shape is triangular prism-like (Figure 7-2a, b, c, and d). The crystal size decreased as the Ca^{2+} concentration increased. However, at high concentration of Ca^{2+}, the crystals appear as a long tube shape (Figure 7-2e), suggesting Ca^{2+} ions cause changes in unit cell packing.

Dataset	Crystallisation condition	$[Ca^{2+}]$
Low $[Ca^{2+}]$		
GH1_17	1.7 M $(NH_4)_2SO_4$, 0.1 M MES (pH 6.5)	1 mM
GH1_20	1.4 M $(NH_4)_2SO_4$, 0.1 M MEPES (pH 7)	5 mM
GH1_21	1.7 M $(NH_4)_2SO_4$, 0.1 M MEPES (pH 7.5)	10 mM
GH1_23	1.7 M $(NH_4)_2SO_4$, 0.1 M MES (pH 6.5)	15 mM
High $[Ca^{2+}]$		
GH1_26	1.6 M KH_2PO_4/ Na_2HPO_4 (pH 6.0)	50 mM

Table 7-1 Crystallisation conditions of His_4-Ans(Gh1) in the presence of Ca^{2+}.

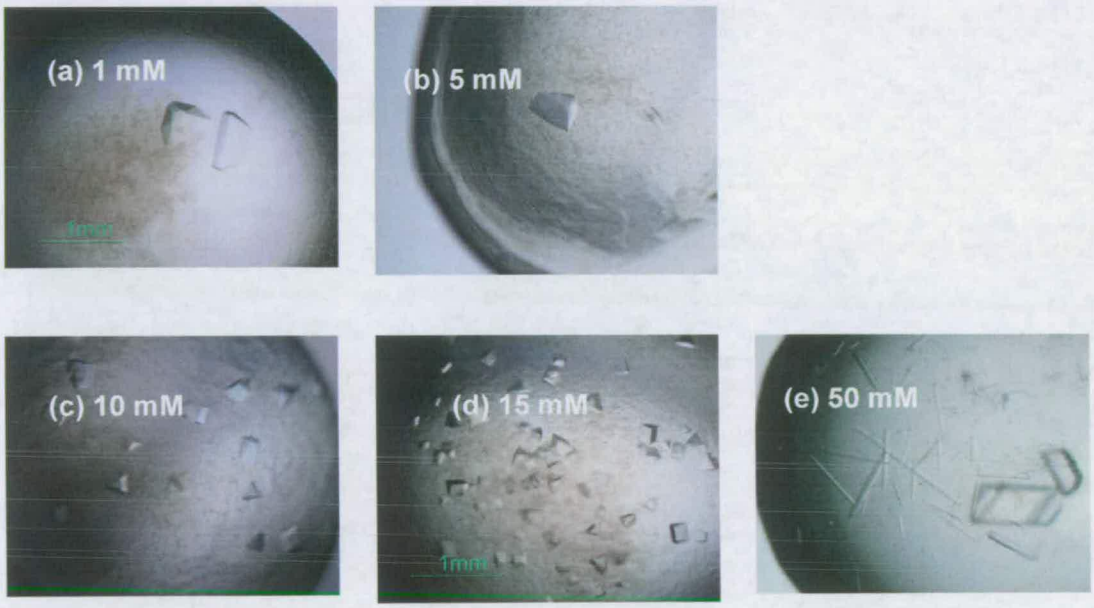

Figure 7-2 His_4-Anx(Gh1) cocrystallised at different Ca^{2+} concentrations. In the presence of 50 mM Ca^{2+}, long rod crystals were harvested and shot by X-ray beam.

7.3.2 Data collection and structural refinement

The crystals, cryo-protected with 25% glycerol, were cooled to 100 K. To visualise the Ca^{2+} ions, single anomalous diffraction (SAD) data of the low calcium-concentration (1-15 mM) crystals were collected using the tuneable synchrotron radiation source, BM14, at the European Synchrotron Radiation Facility (Grenoble, France). The theoretical values for real (*f'*) and imaginary (*f''*) anomalous scattering of calcium are shown in Figure 7-3. The anomalous scattering signal for sulphur is also noted as a positive control, due to the four cysteine and two methionine residues present in Anx(Gh1). Theoretically, the absorption edge for calcium is 3.07Å (*155*). However, that wavelength is beyond the physical limit of the synchrotron source. Therefore, the anomalous data were collected at the longest wavelength available, 1.771 Å, where the anomalous scattering signal for calcium (*f''* = ca 1.5 e^-) is stronger than sulphur (*f''* = ca 0.6 e^-). The difference in anomalous scattering would differentiate Ca^{2+} ions from other biological atoms.

Data sets were indexed using the program *MOSFLM* (*156, 157*) and the resulting intensities were scaled and merged using the program *SCALA* (*158*) from the *CCP4* package (*159*). Unit cell parameters and data collection statistics are shown in Table 7-2. The structures were solved by molecular replacement using the program *MolRep* (*160*) starting from the atomic coordinates of Ca^{2+}-free His_4-Anx(Gh1) (PDB code 1N00) as the search model where the residues at loop regions are substituted by alanine. Structure refinement was performed using the program *REFMAC 5.0* (*161*). To calculate the R_{free} values (*162*) 5% of the data were set aside prior to the refinements. Subsequently, the side chains in the loop regions could be rebuilt unambiguously using the omit map. Model building was performed with the program *Coot* (*163*). Patterson anomalous maps were generated by the program *FFT* from the *CCP4* package (*159*).

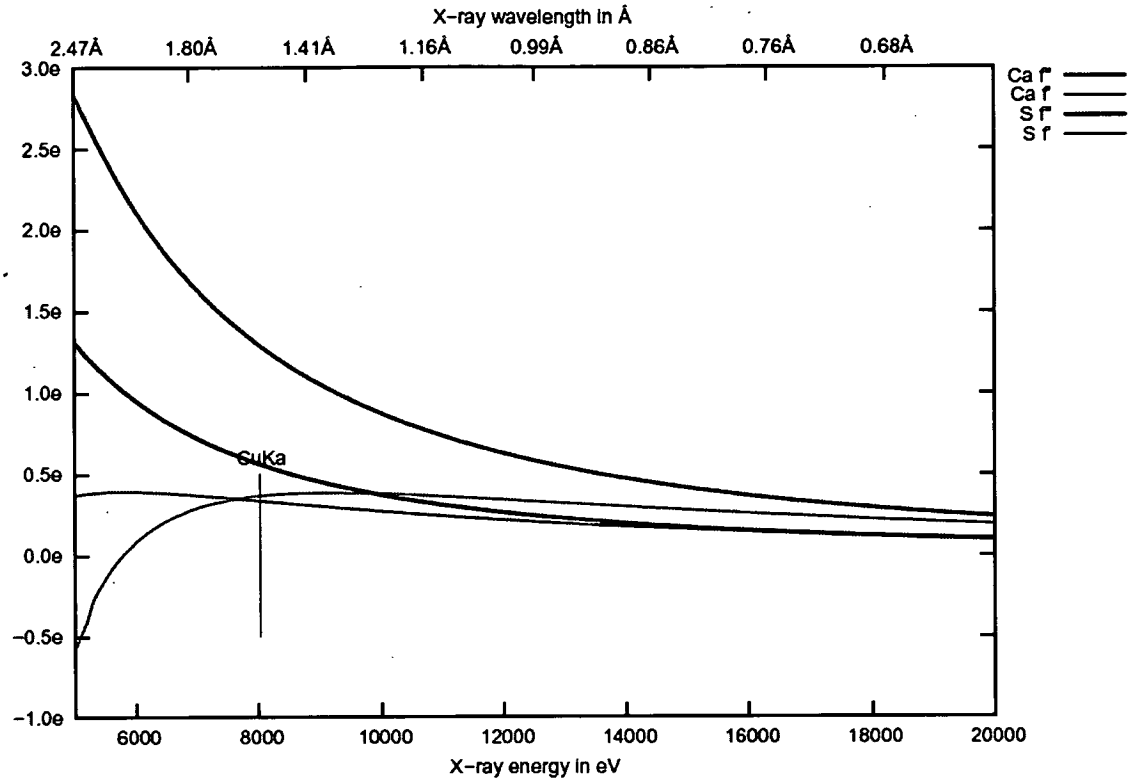

Figure 7-3 Idealized curves for the real (f') and imaginary (f'') anomalous scattering components of calcium (green) and sulphur (blue) as a function of X-ray energy (*155*). Cu$K\alpha$ wavelength (1.5418 Å) is shown for comparison.

7.3.3 X-ray structure of Anx(Gh1) at low Ca^{2+} concentration

The statistics for data collection and structural refinement of the different data sets are summarised in Table 7-2. Indexing of diffraction spots indicated that His_4-Anx(Gh1) at low calcium concentrations (1-15 mM) crystallised in space group $P3_112$ like the Ca^{2+}-free His_4-Anx(Gh1) protein. The unit cell for different Ca^{2+} concentrations are also similar to the Ca^{2+}-free

structure ($a = b = 61.1$ Å, $c = 215.4$ Å, $\alpha = \beta = 90°$, $\gamma = 120°$). The unchanged crystal packing in the presence of Ca^{2+} implies that either the bound Ca^{2+} ions do not cause drastic alteration in the unit cell, or that the Ca^{2+} ions are not bound to the protein at all.

After molecular replacement and structural refinement, the three-dimensional crystal structure of His_4-Anx(Gh1) cocrystallised with 15 mM Ca^{2+} (dataset GH1_23), showed a very similar conformation to the Ca^{2+}-free Anx(Gh1) structure (Figure 7-4a, b). The exception is a mild distortion at the AB loop region in repeat II. As proposed by previous studies on plant annexins (*23, 24*), the endonexin sequence, which functions as a calcium-binding motif, is well conserved in repeat I and showed some small modifications in repeat IV. In the structure obtained from GH1_23 dataset, IAB loop provides a suitable pocket with an adjacent bidentate residue Glu73 for Ca^{2+} binding (left panel, Figure 7-4c). In IVAB loop, however, the bidentate residue Asp303 in the IVDE loop is too far from the IVAB loop (right panel, Figure 7-4c), making the coordination of a Ca^{2+} ion less likely.

Dataset	GH1_17	GH1_20	GH1_21	GH1_23
$[Ca^{2+}]$	1 mM	5 mM	10 mM	15 mM
Data collection				
X-ray source	ESRF (BM14)	ESRF (BM14)	ESRF (BM14)	ESRF (BM14)
Wavelength (Å)	1.033	1.771	1.771	1.771
Space group	$P3_112$	$P3_112$	$P3_112$	$P3_112$
Unit cell dimension (Å)	61.1, 61.1, 215.2	61.0, 61.0, 214.8	60.8, 60.8, 214.5	61.1, 61.1, 215.3
Resolution (Å)	2.1	2.9	2.9	3.3
# measurements	106412	75858	76454	77505
# independent	23894	10540	10452	7253
Completeness	88.2 %	100 %	99.9 %	100 %
Multiplicity	4.7	7.2	7.3	10.7
R_{merge}	0.045	0.066	0.055	0.12
Refinement				
No of reflections in working set	22914 (1048)	9989 (717)	9904 (707)	6872 (507)
No of reflections in test set	1146 (48)	499 (28)	495 (44)	343 (31)
No of non-H protein atoms	2553	2553	2553	2553
No of calcium ions	0	0	0	0
Average B-factor ($Å^2$)	46.0	54.0	53.5	44.9
R/R_{free}	0.268/0.316	0.198/0.267	0.205/0.301	0.179/0.27

Table 7-2 Data collection and structural refinement statistics for data sets collected from crystals cocrystallised with low Ca^{2+} concentrations (1-15 mM). Values for the last resolution shell are given in parentheses.

R_{merge}: $\sum(I-\bar{I})/\sum I$, for all measurements

R-factor: $\sum(|F_o|-|F_c|)/\sum|F_o|$

The datasets collected at λ = 1.771 Å should give rise to a detectable anomalous difference signal for Ca^{2+} ions, if any is present. However, the anomalous density map showed that the only detectable density locates to the sulphur-containing residues, i.e. Cys22, Cys116, Cys243, Cys274, Met112 and Met170 (Figure 7-5a, b). Although there are some visible anomalous density blobs in the solvent, none of them is located in the putative Ca^{2+}-binding loop (Figure 7-5c). It is thus assumed that the density blobs in solvent area are the sites for sulphate derived from the crystallisation buffer. According to Figure 7-3, calcium generates a stronger anomalous difference signal than sulphur at the collection wavelength. If sulphur can be detected at the chosen contour level, calcium should generate a stronger signal in the anomalous difference density map. In the serial Ca^{2+}-cocrystallisation trials (Ca^{2+} concentrations from 1 mM to 15 mM), unfortunately, no significant changes were noted in crystal structure and no visible anomalous difference density blobs could be identified as Ca^{2+} ions.

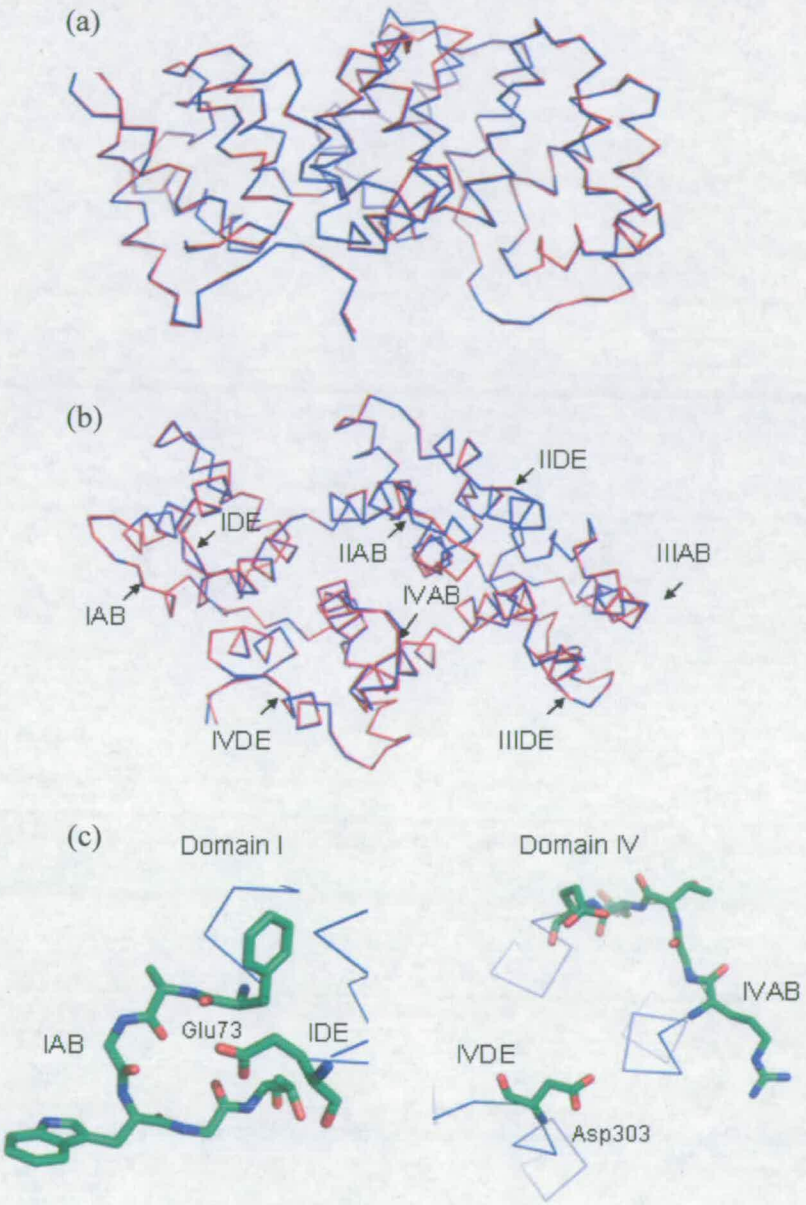

Figure 7-4 Crystal structure of His_4-Anx(Gh1) at 15 mM Ca^{2+} (dataset GH1_23). (a) Superposition of Ca^{2+}-free Anx(Gh1) (blue) (PDB code: 1N00) and Ca^{2+}-cocrystallised His_4-Anx(Gh1) (red). (b) The same superposition as in (a), viewed from the Ca^{2+}-binding sites. Loop regions in each repeat are indicated by arrows. (c) Putative Ca^{2+}-binding sites in repeats I and IV.

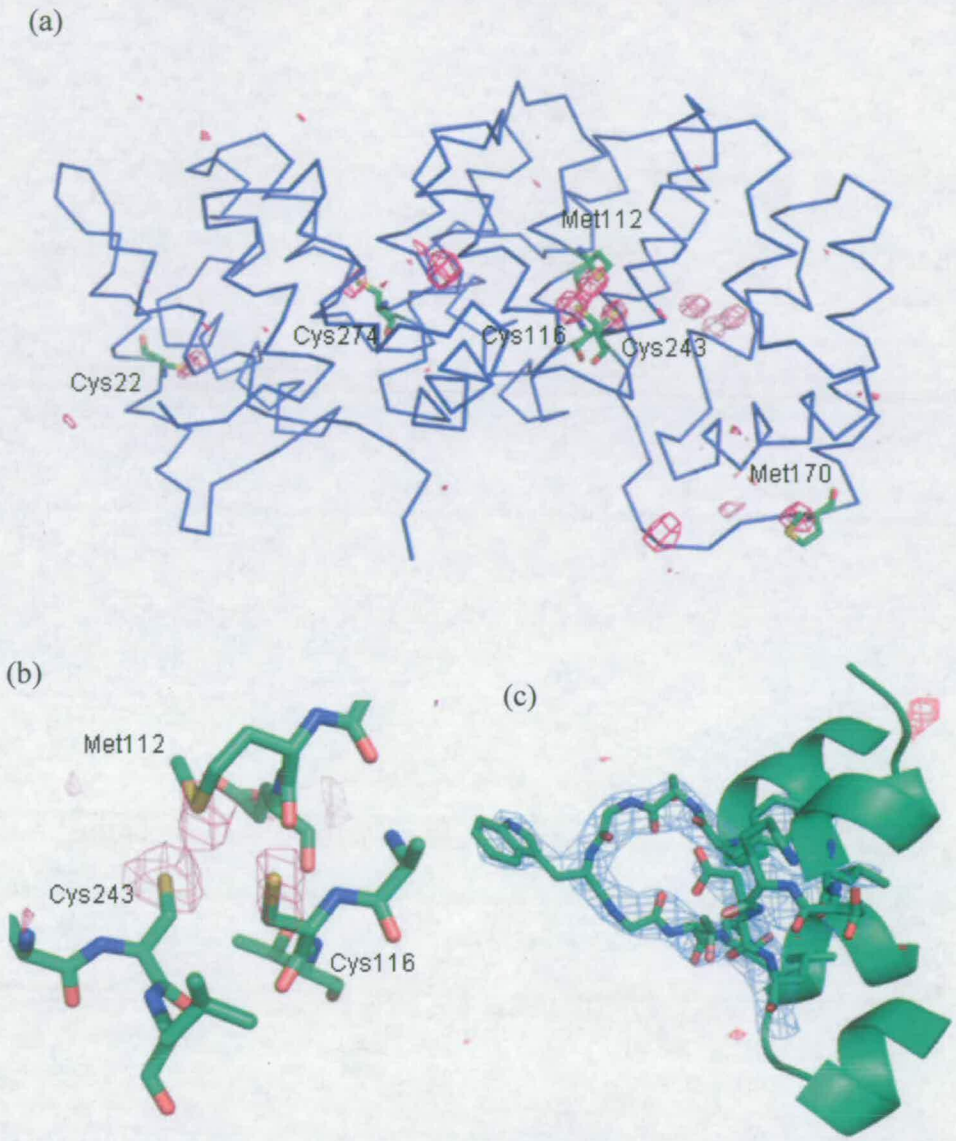

Figure 7-5 Crystal structure of His_4-Anx(Gh1) with anomalous difference Fourier density map (contoured at 3.5 σ, magenta) and 2*Fo-Fc* density map (contoured at 2 σ, blue) (dataset GH1_21). (a) Anomalous map on the scale of full-length His_4-Anx(Gh1) indicating the anomalous density blobs that are contributed by cysteine and methionine residues. (b) Stereo plot and anomalous density map of the S3 cluster composed of Met112, Cys116 and Cys243. (c) 2*Fo-Fc* (blue mesh) and anomalous density map (red mesh) showing the Ca^{2+}-binding site in repeat I.

7.3.4 X-ray structure of Anx(Gh1) at high Ca^{2+} concentration

The X-ray data of crystallised at high Ca^{2+} concentration (dataset GH1_26) was collected at λ = 0.978 Å. Data processing was performed as mentioned in 7.3.2. The initial space group determination yielded P3. Self-rotation functions were calculated with *MolRep* (*160*), indicating the existence of three 2-fold symmetry axes every 60° perpendicular to the 3-fold symmetry axis. No systematic absence of reflections intensities along the direction [00*l*] was found, showing the 3-fold symmetry axis is not a screw axis. Therefore, the space group is either P321 or P312. However, P312 could be excluded due to the poor R_{merge} value calculated by *SCALA* (*158*).

While the Matthews coefficient indicated the presence of two monomers in the asymmetric unit (2.16 $Å^3$/Da; equivalent to 43% solvent content), subsequent molecular replacement proved that only one molecule was present in the asymmetric unit. The new calculation yielded the Matthews coefficient of 4.33 $Å^3$/Da (72% solvent content). In contrast, the solvent content of Ca^{2+}-free His_4-Anx(Gh1) crystal is 62% (3.2 $Å^3$/Da). The high solvent content of His_4-Anx(Gh1) at high calcium concentration corresponds to the rather poor diffraction of the new crystals (2.5 Å). Data collection and structural refinement statistics are summarised in Table 7-3.

Dataset	GH1_26
$[Ca^{2+}]$	50 mM
X-ray source	ESRF (BM14)
Wavelength (Å)	0.978
Data collection	
Space group	P321
Unit cell dimension (Å)	132.7, 132.7, 61.3
Resolution (Å)	35.4 - 2.5
Number of measurements	120728
Number of independent reflections	21804
Completeness (%)	100 (100)
Multiplicity	5.5 (5.5)
R_{merge}	0.117 (0.397)
Refinement	
No of reflections in working set	20672 (1522)
No of reflections in test set	1116 (85)
Visible residues	5 - 321
No of non-H atoms	2832
No of water molecules/ phosphate	261/3
No of calcium ions	3
R/R_{free}	0.193/0.252
Average B-factor for all atoms ($Å^2$)	25.3
Ramachandran plot: Residues in most favoured/additionally allowed/generously allowed region/disallowed region (%)	90.5/8.8/0.7/0

Table 7-3 Data collection statistics of His_4-Anx(Gh1) cocrystallised with 50 mM $CaCl_2$. Values for the last resolution shell (2.50-2.64 Å) are given in parentheses.

R_{merge}: $\sum(I-\bar{I})/\sum I$, for all measurements

R-factor: $\sum(|F_o|-|F_c|)/\sum|F_o|$

Crystals of His_4-Anx(Gh1) in the presence of 50 mM Ca^{2+} were grown in 1.6 M KH_2PO_4/ Na_2HPO_4 (pH 6.0), which is a new condition for plant annexins. The space group of the high Ca^{2+} concentration crystal was determined as P321. The new unit cell retains the trigonal conformation, but has a longer dimension in *a* and *b* (132.7Å) and much shorter in *c* (61.3Å). The different space group gives the first indication of conformation change upon calcium binding.

The contact interface of the 3-fold symmetry is constituted by the IAB loop of one His_4-Anx(Gh1) molecule and IIAB loop of its crystallographic symmetry mate (Figure 7-6a, left panel). The interdigitating loops among the 3-fold symmetric molecules allow the three molecules to pack tightly in the same plane. The 2-fold symmetry axis produces a contact interface constructed by the helices D and E in repeat II, and helix A in repeat III of the two symmetric-related molecules (Figure 7-6a, right panel).

In general, the structure of the Ca^{2+}-bound His_4-Anx(Gh1) agrees with the native His_4-Anx(Gh1) structure solved earlier (Figure 7-6b). Superposition of the two structures using SuperPose (*164*) yields a root-mean square deviation (RMSD) of 1.29 Å. The helical regions are structurally well conserved. However, prominent structural variations are visible in the loop regions, especially in the loops IIAB and IVAB (Figure 7-6b, upper panel). The IIAB loop (Lys102-Asn108) of the new structure moves away from the IIDE loop to facilitate contact with the IAB loop of the crystallographic symmetry mate. The IVAB loop (Asn260-Gly267) moves forward to the IVDE loop, which makes the bidentate group of Asp303 lie closer to the IVAB loop, and allows canonical Ca^{2+} coordination geometry in repeat IV (Figure 7-6b, lower panel).

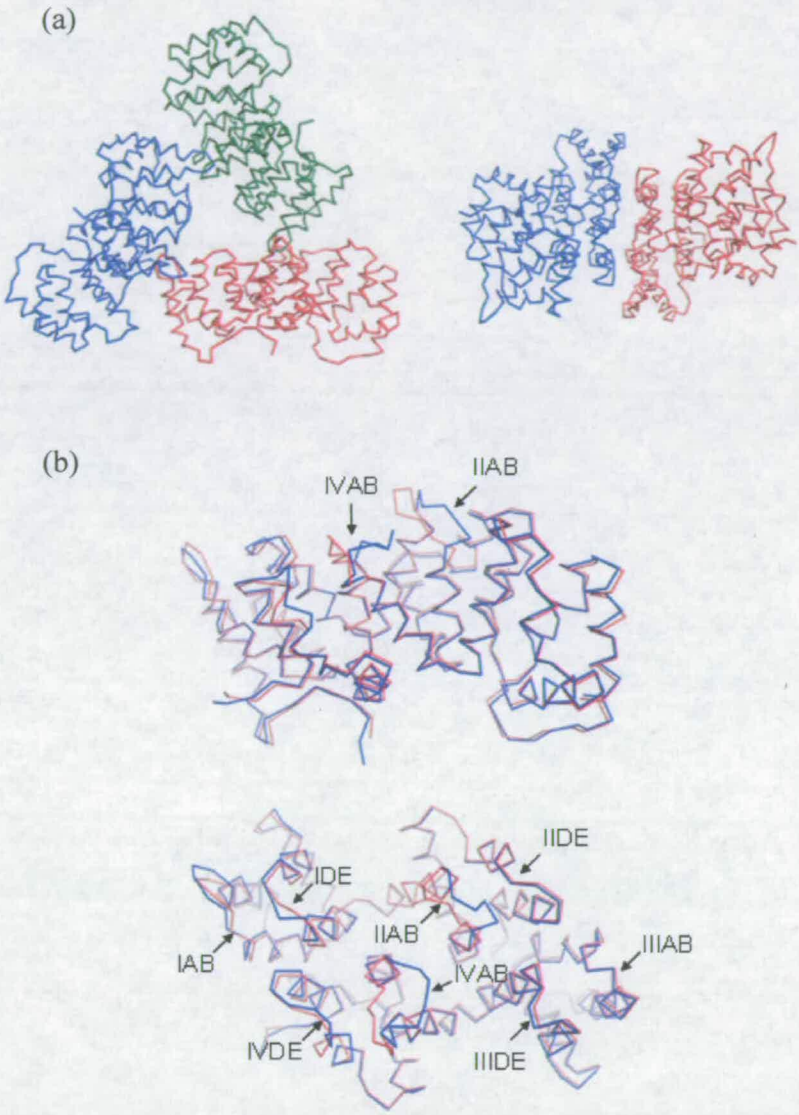

Figure 7-6 (a) The crystal packing of His_4-Anx(Gh1) in the presence of 50 mM Ca^{2+}. Left panel: view along the 3-fold symmetry axis. The IAB loop of the red molecule has a close contact with the IIAB loop of the blue molecule. The contact is also found between blue and green molecules, and green and red molecules. Right panel: view along the 2-fold symmetry axis. (b) Upper panel: superposition of the high Ca^{2+} concentration His_4-Anx(Gh1) (red) with native Ca^{2+}-free His_4-Anx(Gh1) (blue). Prominent conformational changes are found in loops IIAB and IVAB (as indicated by arrows). Lower panel: top view of the two molecules. The eight loop regions are highlighted by arrows.

In dataset GH1_26, two strong electron density peaks are found in the loops IAB and IVAB, respectively, as well as a third peak in the IVDE loop. Despite the lack of anomalous diffraction data, the 2*Fo-Fc* and *Fo-Fc* electron density maps indicate the existence of Ca^{2+} due to the satisfaction of Ca^{2+} coordination geometry. The atoms involved in the coordination of the three Ca^{2+} ions are summarised in Table 7-4. It has been shown that the IAB loop in Ca^{2+}-free His_4-Anx(Gh1) structure is suitable for Ca^{2+} coordination (Figure 7-4c, left panel). In the Ca^{2+}-bound structure, a Ca^{2+} coordination with pentagonal bipyramid geometry is found in the IAB loop as expected (Figure 7-7a). This is a typical type II Ca^{2+} binding site, where CA1 is harboured by three carbonyl oxygens (Phe29 O, Gly31 O and Gly33 O) in the IAB loop, and carboxylate oxygens of Glu73 in the IDE loop. The water molecule HOH3 serves as the fifth ligand of the pentagonal plane. The apical ligand of the bipyramid is replaced by the Trp104 carbonyl oxygen of a symmetry mate. The Trp104 located in the IIAB loop of the symmetry mate adopts an exposed conformation to donate its carbonyl oxygen for the coordination.

In comparison with the structure of Ca^{2+}-free His_4-Anx(Gh1) (Figure 7-4c, right panel), the IVAB loop reveals a "close" form, where the backbone carbonyl oxygen atoms move closer to the bidentate group in the IVDE loop (Figure 7-7b). CA2 is coordinated by three backbone carbonyl oxygens (Ile259 O, Arg261 O and Gly263 O) from the IVAB loop, and the bidentate carboxylate of Asp303 in the IVDE loop. No oxygen atoms from water molecules can be found to consolidate the coordination. Nevertheless, the coordination geometry can be regarded as a type II Ca^{2+} binding site. In several X-ray structures of AnxA5 (PDB codes 1AVH and 1SAV), the Ca^{2+} ions located in the IVAB loop were found with the same five-fold coordination (*9*). The resolution of these structures is 2.3 Å for 1AVH and 2.5 Å for 1SAV. The previously published

structures support the conclusion for GH1_26. The lack of the surrounding water molecules is presumably due to the resolution limit of the dataset.

As anticipated from amino acid sequence alignment, CA1 and CA2 occupy a conserved motif for type II Ca^{2+} binding. In contrast, CA3, harboured in the IVDE loop, binds in a geometry typically found with type III sites (Figure 7-7c). The Ca^{2+} ion is coordinated by two carbonyl oxygens (Val301 O and Thr304 O), and carboxylate oxygens of Glu309. Two water oxygens are found to construct the pentagonal plane. One phosphoryl oxygen of the phosphate serves as the oxygen ligand in the axial position of the bipyramid geometry. It has been shown that negatively charged sulphate ions are involved in Ca^{2+} coordination in rat AnxA5 (PDB code: 1ANX) (*165*). Therefore, phosphate ions in the new crystallisation condition may play a similar role in Ca^{2+} coordination.

One should note that, the mean 2*Fo*-*Fc* peak heights corresponding to the three Ca^{2+} ions are weaker than the heights of sulfur atoms. Therefore, the binding sites are not fully occupied by Ca^{2+} ions. The fact is also in agreement with low calcium binding affinity in the absence of phospholipid bilayer. However, the occupancy was not refined because of the resolution limit of the dataset.

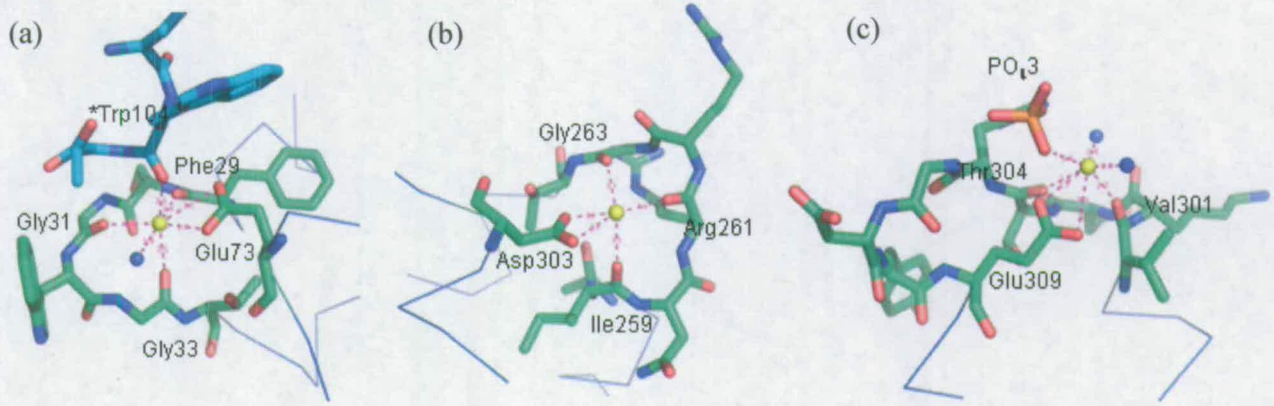

Figure 7-7 Ca^{2+} coordination observed in the structure of His_4-Anx(Gh1) in the presence of 50 mM $CaCl_2$. Ca^{2+} ions are illustrated as yellow spheres, and water molecules as blue spheres. (a) CA1 in IAB loop. (b) CA2 in IVAB loop. (c) CA3 in IVDE loop. The backbone illustrated in cyan is the symmetry-related molecule.

	Binding site	Type	Coordinaiton	Backbone carbonyls (Å)	Side-chain carboxyls (Å)	Solvent (Å)
CA1	IAB	II	7	Phe29: 2.37, Gly31: 2.58, Gly33: 2.53, *Trp104: 2.41	Glu73 OE1: 3.04, Glu73 OE2: 2.71	HOH3: 2.93
CA2	IVAB	II	5	Ile259:2.56, Arg261:2.12, Gly263:2.12	Asp303 OD1: 2.44, Asp303 OD2: 2.78	
CA3	IVDE	III	7	Val301: 2.15, Thr304: 2.67	Glu309 OE1: 2.91, Glu309 OE2: 3.00	HOH96: 2.96, HOH134: 2.38, PO_4 3 O4:2.50

Table 7-4 Ca^{2+} ions in His_4-Anx(Gh1) and the distances to the surrounding ligands. *Trp104 is from a crystallographic symmetry-related molecule.

In AnxA5, Trp187 has been demonstrated to adopt a buried form in the absence of Ca^{2+} and an exposed form in the presence of Ca^{2+} (*165, 166*). The conformational switch also correlates with the interaction with phospholipids as demonstrated by the significant increase in fluorescence emission intensity (*167*). Similarly, the strictly conserved tryptophan in the IAB loop in plant annexins has been thought to play a functional role. The crystal structure of Anx24(Ca32) (*23, 64*) shows that Trp35 adopts both loop-out and loop-in conformations between the two non-crystallographic symmetry mates. The native His_4-Anx(Gh1) structure shows that Trp32 is located halfway between the two conformations (*24*). However, Trp32 in the Ca^{2+}-bound His_4-Anx(Gh1) does not show a significant side chain movement. Instead, it nestles into the cleft between repeats I and II of the symmetry-related molecule. Intriguingly, one convex surface tryptophan (104) is buried in the Ca^{2+}-free structure. Upon Ca^{2+} binding, the IIAB loop shows a loop movement and the carbonyl oxygen of Trp104 is exposed to coordinate the Ca^{2+} ion in the symmetric IAB loop (Figure 7-8). Therefore, the Trp104 side chain inserts into a hydrophobic cleft constituted by Phe29, Lys68 and Lys72 of its symmetry mate.

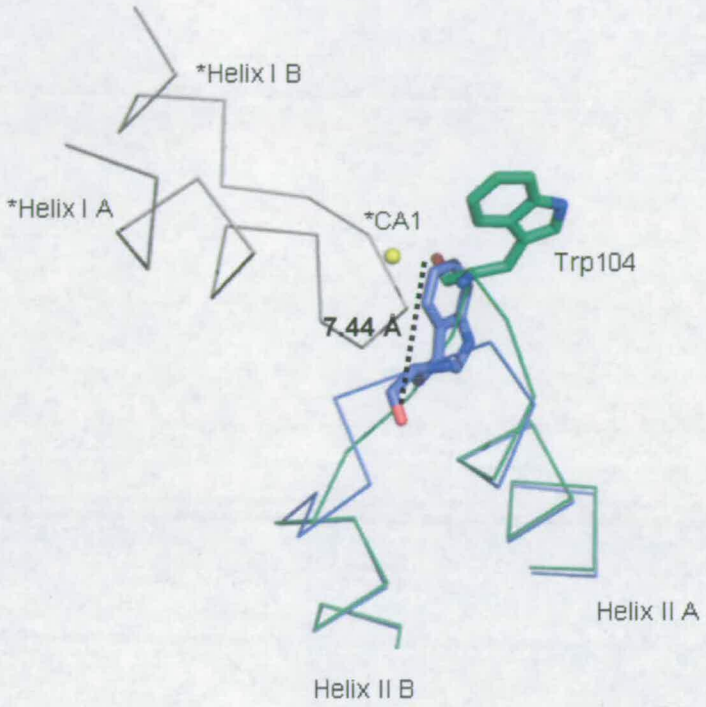

Figure 7-8 Superposition of the IIAB loop of Ca^{2+}-bound (green line) and Ca^{2+}-free (blue line) His_4-Anx(Gh1). The distance between the Trp104 CO of Ca^{2+}-bound and Ca^{2+}-free His_4-Anx(Gh1) is 7.44 Å. *The IAB loop from the symmetry-related molecule is shown in grey.

7.4 Discussion

It is generally thought annexins bind to Ca^{2+} ions with considerably low affinity in the absence of phospholipid (*9, 26*). This can be supported by the overall dissociation constant for Ca^{2+}-binidng of AnxA2 in the absence of phospholipid has been quantified as 0.5 mM (*168*). Patel et al. used ITC to evaluate Ca^{2+}-dependent membrane binding properties of AnxA1, AnxA2, AnxA5 and AnxB12, and demonstrated an undetectable calorimetric signal, when Ca^{2+} was titrated into the proteins in the absence of vesicles (*152, 153*). The low Ca^{2+} affinity is in agreement with the ITC study of His_4-Anx(Gh1). Downward spikes were observed in the blank when Ca^{2+} was titrated into buffer in the absence of vesicles. Similarly, the ITC measurements with a sample containing His_4-Anx(Gh1) showed similar profiles, and almost no heat release was observed after blank subtraction. Therefore, the enthalpy change

shown in the blank experiment should be caused by dilution of $CaCl_2$. In contrast, annexins show a much higher affinity to calcium ions in the presence of membrane (*4, 152, 153, 168-170*). AnxA1 and AnxA2 in the presence of phospholipid show Ca^{2+} affinity with a dissociation constant of 75 and 4.5 μM, respectively (*171, 172*). The numbers are comparable to the dissociation constant of His_4-Anx(Gh1) (K_d = 11.01 μM). The pronounced enthalpy change of the Ca^{2+}-His_4-Anx(Gh1) complex, in the presence of vesicles, is reminiscence of the behaviour of its animal and invertebrate counterparts.

The Ca^{2+}-binding stoichiometry of AnxA1, AnxA2, AnxA5 and AnxB12 calculated by ITC measurements indicates 4.1 ± 0.2, 2.0 ± 0.1, 12.0 ± 0.5 and 11.0 ± 0.5, respectively (*152, 153*). The authors divide the four annexins into two subgroups where AnxA1 and AnxA2 show low Ca^{2+} stoichiometry, whereas AnxA5 and AnxB12 show high Ca^{2+} stoichiometry. The significant difference in Ca^{2+} stoichiometry is due to the missing of some regulatory residues of Ca^{2+}-binidng sites in AnxA1 and AnxA2. It has been suggested that Anx(Gh1) harbours the endonexin motif in repeats I and IV for canonical calcium-binding (*24*). Thus His_4-Anx(Gh1) can be considered as a low Ca^{2+} stoichiometry annexin. The Ca^{2+} stoichiometry (~ 4) obtained by ITC implies that there might be other Ca^{2+}-binding sites harboured in Anx(Gh1), in addition to the two putative type II binding sites in repeats I and IV.

The initial crystallisation trial of Ca^{2+}-bound His_4-Anx(Gh1) was based on the condition used to produce Ca^{2+}-bound AnxA5 crystal, obtained from cocrystallisation in the presence of 1 mM Ca^{2+} (*173*). However, the results for the cocrystallisation method were not satisfactory, as no detectable anomalous difference density could be identified as Ca^{2+} ions. Increasing the Ca^{2+} ion concentration to a higher level in cocrystallisation trials was infeasible because ammonium sulphate in the crystallisation buffer forms insoluble $CaSO_4$ upon adding Ca^{2+}. The same difficulties were also encountered by Lewit-Bentley and

coworkers, when they attempted to cocrystallise AnxA5 in a high Ca^{2+} concentration solution (*165*), although they were eventually successful in obtaining a Ca^{2+}-bound structure. Soaking with Ca^{2+} has also been reported to produce Ca^{2+}-bound AnxA5 crystals (*10*). Unfortunately, soaking the Ca^{2+}-free His_4-Anx(Gh1) crystals with a high concentration calcium solution cracked the crystals immediately. Crystals obtained from high concentration solutions of Ca^{2+} (50 mM and 100 mM) using phosphate as a precipitant produced protein crystals successfully. The new reservoir condition is of great importance because it can be used to crystallise other annexins in the presence of high Ca^{2+} concentration.

Three Ca^{2+} ions are located in the new crystal structure of His_4-Anx(Gh1). However, the number does not correspond well with the predicted stoichiometry generated by the ITC experiment. It should be highlighted that, in the ITC experiments, Ca^{2+}-binding of His_4-Anx(Gh1) was performed in the presence of phospholipid vesicle, whereas there is no phospholipids in the crystals. Therefore, functional Ca^{2+} binding sites may not be able to be localised in crystal structures because of the low Ca^{2+} affinity in the absence of phospholipids.

In the Ca^{2+}-bound His_4-Anx(Gh1) structure, two Ca^{2+} ions were found in classical type II Ca^{2+}-binding sites in the loops IAB and IVAB, which conform very well to the prediction of type II Ca^{2+} binding sites of Anx(Gh1) (*23*). One Ca^{2+} ion is coordinated in the type III Ca^{2+}-binding site in the IVDE loop. The result is consistent with the general concept that AB loops have higher affinity for Ca^{2+} than do DE loops (*10*). In addition to the two type of binding sites, there is another type of binding sites, which are characterised in the AB' loops, found in several annexins (*12-14, 29*). The Ca^{2+} ions in the AB' loops are coordinated by the carboxylate side chains near the beginning of the helix B. Thus, Glu36 (repeat I), Asp191 (repeat III) and Asp265 (repeat IV) of His_4-Anx(Gh1) are geometrically suitable for the type

of Ca^{2+} binding. Though we use high concentration of Ca^{2+}, the binding site might be unoccupied due to the low affinity in the absence of phospholipid.

There are five phosphate ions localised in the Ca^{2+}-bound structure. The phosphate ion, PO_4 3, is of great interest because it displaces the water molecule in the Ca^{2+} coordination in IVDE loop (Figure 7-7c). Swairjo et al. (*29*) determined the structure of Ca^{2+}-bound rat AnxA5 in the presence of phospholipid analogues, glycerophosphoserince (GPS) and glycerophosphoethanolamine (GPE) (PDB code: 1A8A and 1A8B, respectively). In each complex, the phosphoryl oxygens of the analogues displace the water molecule in the apical ligand position of Ca^{2+}coordination in the IIIAB loop. This displacement is also shown in the complex structure of phospholipase A_2 (PLA_2) with phospholipid analogues (*174-176*), where PLA_2 has a type II Ca^{2+} binding loop similar to AnxA5. It is important to note that the phospholipid analogues are stabilised by another Ca^{2+}-binding pocket in an AB' site of the IIIAB loop. However, the binding site in the IVDE loop of His_4-Anx(Gh1) is too narrow to accommodate the head group of phospholipids. Thus, whether the phosphoryl coordination displacement is an artefact will only be determined by cocrystallising proteins in the presence of phospholipid analogues.

8 The putative function of Anx(Gh1) in response to oxidative stress

8.1 Introduction

Thiol-dependent regulatory switches play a key role in the response to oxidative stress, that results from partially reduced oxygen species (*177*). In normal cells, the cytoplasm contains plenty of reducing buffers and disulfide reductase, which allow the solvent accessible cysteine residues in proteins to maintain their reduced forms. Exposure of cysteine to partially reduced oxygen species, such as hydrogen peroxide, causes oxidation of its thiol group of cysteine to form an unstable product called sulfenic acid (RSOH). The product can be oxidised further to yield stable products such as sulfinic acid (RSOOH), sulfonic acid (RSO_3H) and finally, the disulfide bond, formed between two thiol groups. Formation of a disulfide bond sets free two electrons, and reduces the reactive oxygen species.

The X-ray crystallographic structure of cotton Anx(Gh1) shows that two sterically adjacent cysteine residues, Cys116 and Cys243, are in a reduced form, although the distance between the two residues (5.5 Å) is close enough to form a disulfide bond (*24*). It was thus hypothesised that the two cysteines might be involved in a RedOx process. In this section, the study aims to evaluate the RedOx activity of Anx(Gh1), in response to hydrogen peroxide (H_2O_2). Tryptic mapping using mass spectrometry was applied to fingerprint the trypsin-digested peptides, and evaluate whether the two cysteines form a disulfide bond. Furthermore, Anx(Gh1) treated with H_2O_2 was crystallised. The crystal structure was expected to yield an oxidised form of Anx(Gh1).

8.2 Trypsin digest fingerprint

The analytical method of trypsin digest fingerprinting was developed to identify a protein using mass spectrometry (*178*). The protein of interest is first cleaved into peptides using a protease, such as trypsin, thermolysin or chymotrypsin. The masses of the cleaved peptides are determined by mass spectrometry, either MALDI-MS or ESI-MS. The output of peptide masses is compared to a database of estimated protease-cleaved peptide masses of all known protein entries. The method provides a straightforward approach to confirm protein identity that merely requires merely peptide masses. In this study we adopted the in-solution trypsin digestion method to cleave His_4-Anx(Gh1). Fingerprinting of the digested peptides was performed using MALDI-TOF mass spectroscopy.

As mentioned in the first chapter, the X-ray structure of Anx(Gh1) shows two adjacent cysteine residues, Cys116 and Cys243, existing in their reduced forms. The steric positions of the two cysteines are displayed in Figure 8-1. In addition to the two cysteines, there are two other cysteines, Cys22 and Cys274 located in repeats I and IV, respectively. Theoretically, trypsin digestion of unoxidised His_4-Anx(Gh1) should generate 45 peptides. The amino acid sequence and calculated mass ($M—H^+$) of each cysteine-containing peptide are shown in Table 8-1. Ideally, if Cys116 and Cys243 are oxidised and form an intramolecular disulfide bond, one should be able to detect the disappearance of mass peaks p13 (Cys116) and p33 (Cys243), and the appearance of disulfide linked peptides p13–33 (calculated mass = 2587.2).

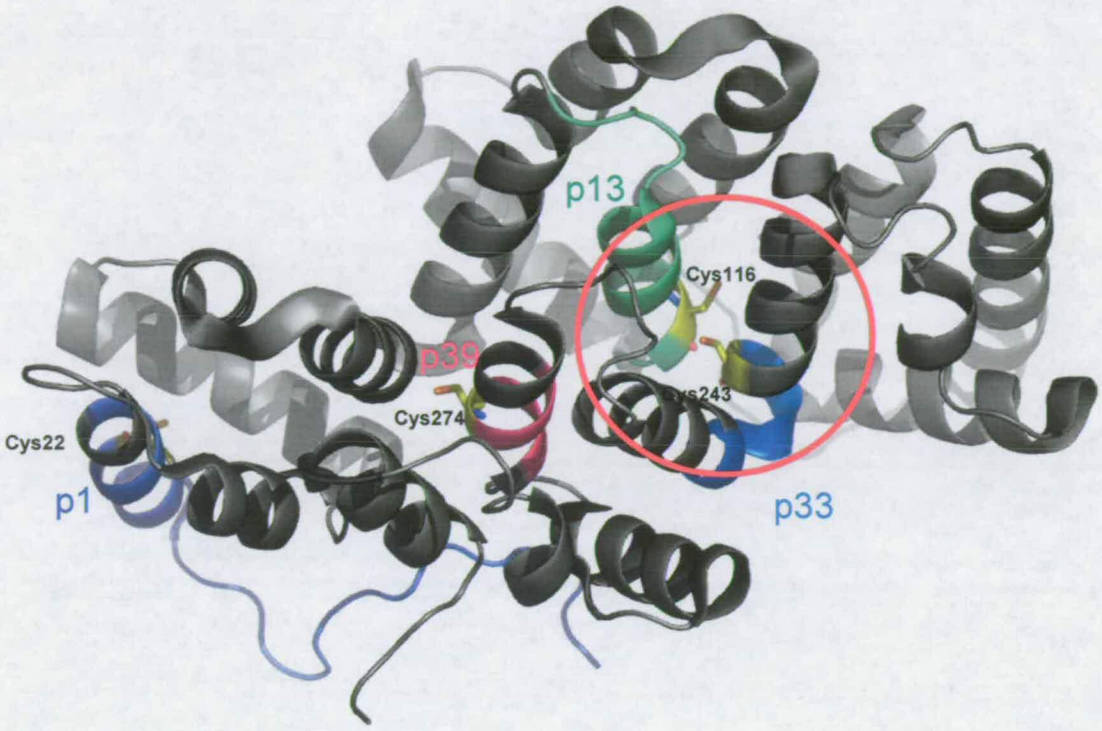

Figure 8-1 The structural locations of the four cysteine-containing peptide segments in Anx(Gh1), p1, p13, p33 and p39, obtained by the theoretical trypsin cutting sites. Cysteine residues, Cys22, Cys116, Cys243 and Cys274, are coloured yellow and their side chains are shown in stick diagram to display the orientation of the sulphur atoms. The two adjacent cysteines, Cys116 and Cys243, are shown inside the red circle.

Peptide segment	Sequence	mass (Da)
p1 1-26	M-A-H-H-H-H-A-T-L-T-V-P-T-T-V-P-S-V-S-E-D-C-E-Q-L-R	2896.4
p13 104-118	W-T-S-S-N-Q-V-L-M-E-I-A-C-T-R	1738.8
p33 243-249	C-L-V-Y-P-E-K	851.4
p39 272-276	V-V-C-T-R	577.3

Table 8-1 Sequences and masses of four cysteine-containing peptides derived from the theoretical cleavage site of trypsin. Cysteines are highlighted in grey box.

8.2.1 Procedures

In order to obtain the H_2O_2/Anx(Gh1) molar ratios (50:1~5000:1), an appropriate concentration of hydrogen peroxide (H_2O_2) was prepared by diluting stock H_2O_2 solution (30%) in 50 mM ammonium bicarbonate. Protein solution was diluted to an appropriate concentration using the H_2O_2-containing ammonium bicarbonate solution. Samples were incubated for 1 h at 37°C. The oxidised samples were then digested using the method as described in section 3.7.2.

8.2.2 Results

There is a standard variable defined as x = n(H_2O_2)/n(protein). Trials were constructed by controlling certain variables: the H_2O_2 to protein molar ratio x, the alkylation of cysteine thiols using iodoacetamide, and the unfolding condition (Table 8-2). Peak assignment for each condition is summarised in Table 8-3. In trial 1, His_4-Anx(Gh1) was oxidised at x = 50 without adding the alkylating reagent, iodoacetamide. There was no mass peak found to match the theoretical mass of the four cysteine-containing peptides. It is assumed that the digested peptides in this trial form a non-specific disulfide bridges with other cysteine-containing peptides. The masses of all possible disulfide-bonded peptides are shown as a matrix in Table 8-4. The figures were calculated by summation of any two protonated peptide masses (M—S—H + H^+) minus the mass of three hydrogen atoms (M_1—S—S—M_2 + H^+). Interestingly, three mass peaks: 2587.0537, 2313.0843 and 1425.7350 are observed in Table 8-5, representing disulfide-bonded peptides, p13–33, p13–39 and p33–39 respectively. Although the species with a mass of 2587.0537 is very close to the mass of the target p13–33, one cannot exclude the possibility that the p13-33 disulfide-bonded peptide is formed by the non-specific oxidation of cleaved p13 and p33 peptides after trypsin digestion.

Experiment trial	*Molar ratio x	Alkylation of cysteine	Denaturing conditions
1 (S10_3)	50	-	60°C 30 min
2 (S19_0)	0	+	60°C 30 min
3 (S19_1)	50	+	60°C 30 min
4 (S19_2)	500	+	60°C 30 min
5 (S19_3)	5000	+	60°C 30 min
6 (S20_0_2)	0	+	100°C 10 min
7 (S20_1_2)	50	+	100°C 10 min
8 (S20_2_2)	500	+	100°C 10 min
9 (S20_3_2)	5000	+	100°C 10 min

Table 8-2 Summary of the different experimental conditions for each of the nine oxidation trials. *Molar ratio x is defined as $n(H_2O_2)/n(protein)$.

Alkylation of cysteine using iodoacetamide has proven to be a useful tool for improving peptide mapping and protein identification in mass spectroscopy (*179*). To eliminate the effect of any residual oxidative reagent in solution, iodoacetamide was added to prevent the reduced-form cysteine from forming a non-specific disulfide bond. In trials 2 to 5 (Table 8-2), a step-wise increase of ratio x was employed ranging from 0 to 5000, followed by protein denaturation procedure at 60 °C for 30 min. Other experiments (trials 6 to 9), treated at 100 °C 10 min were performed to compare the completeness of trypsin digestion. Therefore, trials 2 to 5 and trials 6 to 9 are corresponding experiments with difference of denaturing conditions.

Trial	p1 (C22) (2896.3828 Da)	p13 (C116) (1738.8251 Da)	p33 (C243) (851.4331 Da)	p39 (C274) (577.3126 Da)
1	-	-	-	-
2	-	1738.8643	851.4934	577.3367
3	-	1738.8735	-	577.3194
4	-	1738.8866	-	577.3376
5	-	-	-	-
6		1738.9022	-	577.3270
7	-	1738.8630	-	577.3264
8	-	-	-	-
9	-	-	-	-

Table 8-3 Summary of the results of the nine tryptic digest fingerprint trials. For each of the four cysteine-containing peptides, both the theoretical masses (in parentheses) and the experimentally observed peak assignment masses (*m/z*) are shown. The cysteine-containing peptide whose mass could not be assigned is denoted as (-). The mass is derived from the experimental peptide mass subtracted by the mass of iodoacetamide.

Mass matrix	p1 (C22)	p13 (C116)	p33 (C243)	p39 (C274)
p1 (C22)	5789.7437	4632.1860	3744.7940	3470.6735
P13 (C116)		3474.6283	2587.2363	2313.1158
p33 (C243)			1699.8443	1425.7238
p39 (C274)				1151.6033

Table 8-4 Mass matrix for all possible disulfide-linked peptide masses. The figures (Da) represent the masses of the disulfide-bonded peptides.

	p1 (C22)	p13 (C116)	p33 (C243)	p39 (C274)
p1 (C22)	X	X	X	X
P13 (C116)		X	2587.0537	2313.0843
p33 (C243)			X	1425.7350
p39 (C274)				X

Table 8-5 Peak assignment for disulfide-linked peptides of trial 1. The observed peak masses (m/z) which match the mass matrix (**Table 8-4**) are shown. The theoretical disulfide-bonded peptides which can not be detected are denoted (X).

In trial 2, where no H_2O_2 was added, peak assignment showed that three cysteine-containing peptides (p13, p33 and p39) appeared in the mass spectrum (Table 8-3). In addition, no non-specific disulfide-bonded species were found (data not shown). Compared with trial 1, the result indicates that the residual H_2O_2 leads to non-specific disulfide-linkage of the four cysteine-containing peptides. It also shows that alkylation of cysteine successfully reduces the ambiguity of peak assignment. Upon addition of H_2O_2, peptide p33, containing Cys243 (trials 3 and 4), was missing in the mass spectrum. At ratio x = 5000, none of the four cysteine-containing peptides was found (trial 5) (Table 8-3). No peaks from trials 2 to 5 matched the mass of p13-33 peptide. In trial 6 (no H_2O_2 addition), two peaks were assigned representing p13 and p39, whereas peptide p33 was not detected (Table 8-3). The spectrum intensity of peptide p13 in trial 6 is weaker than the corresponding peak in trial 2. The comparison of two denaturing treatment suggests that the conditions of 60°C for 30 min are more effective for protein fragmentation. As the H_2O_2/protein molar ratio increased (like in trials 5, 8 and 9), the peptides p13 and p39 started to disappear from the spectrum. Similar to trials 2 to 5, no peak could be assigned using masses matrix of all possible disulfide-bonded peptides, including the targeted p13–33 species (trials 6 to 9).

The fingerprinting data shown in the trials indicate that no intramolecular disulfide bond between the two adjacent cysteines, Cys116 and Cys243, can be discovered after H_2O_2 oxidation using the tryptic mapping method. It is important to note that as the concentration of H_2O_2 increases, the peptide fingerprint becomes more difficult. It is speculated that the presence of excessive H_2O_2 causes an intermolecular disulfide link and forms heterogeneous oligomers, leading to a decrease in the digestion efficiency of trypsin. Furthermore, the formation of oligomers would increase the ambiguity of peak assignment, should miscleavage occur.

8.3 X-ray crystallographic structure of His_4-Anx(Gh1) after H_2O_2 treatment

8.3.1 Protein crystallisation

Protein crystals of H_2O_2-treated Anx(Gh1) were obtained by mixing purified His_4-Anx(Gh1) with an appropriate concentration of H_2O_2. Crystallisation solutions were based on the documented conditions which yielded the native Anx(Gh1) crystal (*24*). Crystals were obtained using the hanging-drop vapour-diffusion method. For cocrystallisation, 25 mg/ml of His_4-Anx(Gh1) were mixed with H_2O_2 stock solution in a ratio of 4:1 (v/v). Droplets consisted of 2 µl of oxidised protein and 2 µl of reservoir solution, equilibrated against a 300 µl reservoir solution at 290 K. Protein crystals were obtained after 4 weeks. For H_2O_2 soaking, the native crystals were obtained and soaked in a new mother liquor containing 22 mM H_2O_2.

The crystallisation conditions and H_2O_2 concentrations, from which crystals and corresponding data sets were collected, are summarised in Table 8-6. At low concentrations of H_2O_2 (20 µM and 1 mM), the crystal shape is triangular prism-like (Figure 8-2a, b). However, at higher concentration of H_2O_2 (10 mM), the crystals display a triangular, plate shape (Figure 8-2c). For H_2O_2 soaking, the crystals obtained from 1.7 M $(NH_4)_2SO_4$, 0.1 M MES (pH 6.5) were soaked in a new solution containing 2.3 M $(NH_4)_2SO_4$, 0.1 M MES (pH 6.5), and 20 mM H_2O_2 (Figure 8-2d). The crystals were soaked for 20 min, because they started to crack in the soaking solution after the soaking time.

	Crystallisation condition	$[H_2O_2]$	*Molar ratio x	Cocrystallisation /soaking
G22_14	2.0 M $(NH_4)_2SO_4$ 0.1 M MES (pH 6.5)	20 µM	0.04	cocrystallisation
G33_2_9	2.0 M $(NH_4)_2SO_4$ 0.1 M MEPES (pH 7.5)	1 mM	2	cocrystallisation
G40_8	1.7 M $(NH_4)_2SO_4$ 0.1 M MEPES (pH 7.0)	10 mM	20	cocrystallisation
G44_1	1.7 M $(NH_4)_2SO_4$ 0.1 M MES (pH 6.5)	20 mM	-	soaking

Table 8-6 Crystallisation conditions of His_4-Anx(Gh1) after H_2O_2 treatment. The corresponding crystal images are shown in **Figure 8-2**.

*Molar ratio x is defined as $n(H_2O_2)/n(protein)$.

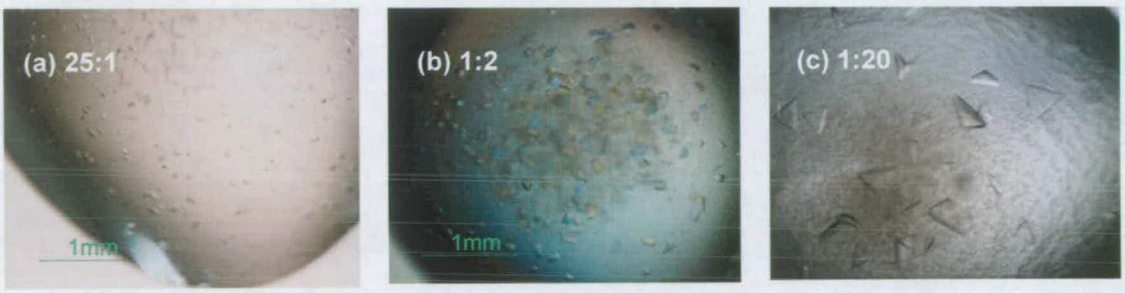

Figure 8-2 Crystals of His_4-Anx(Gh1) after H_2O_2 treatment. The crystals were obtained from the conditions summarised in **Table 8-6**. Protein:H_2O_2 molar ratio in each crystallisation setup is shown.

8.3.2 Data collection and structural refinement

The crystals, cryo-protected with 25% glycerol, were cooled to 100 K and X-ray diffraction data were collected. Synchrotron radiation at the protein crystallography beamline 14.1 at the Daresbury Synchrotron Radiation Source (Daresbury, UK) was used, as was BM14 at the European Synchrotron Radiation Facility (Grenoble, France). Data sets were indexed using the program *MOSFLM* (*156, 157*) and the resulting intensities were scaled and merged using the program *SCALA* (*158*), from the *CCP4* package (*159*). Unit cell parameters and data-collection statistics are shown in Table 8-7. The structures were solved by molecular replacement using the program *MolRep* (*160*), starting from the atomic coordinates of the C116G and C243G mutant of Anx(Gh1) (PDB code 1N00), as the search model. Structure refinement was performed using the program *REFMAC 5.0* (*161*). To calculate the R_{free} values (*162*), 5% of the data were set aside prior to the refinements. The initial refinement cycles were conducted using the omit map. Subsequently, the two glycine residues were replaced by cysteine, and the conformation of the side chain was determined unambiguously, according to the final omit map.

8.3.3 Crystal structure of H_2O_2-treated His_4-Anx(Gh1)

As shown in Table 8-7, both H_2O_2-treated and native Anx(Gh1) crystallise in the same space group: $P3_112$, with similar unit cell dimensions: $a = b = 61.1$ Å, $c = 215.4$ Å and angles: $\alpha = \beta = 90°$, $\gamma = 120°$. The c-axis is, however, shorter in the H_2O_2-soaked crystals (dataset G44_1). The molecular replacement solution revealed that there is one molecule in the asymmetric unit, as indicated by the Matthew coefficient calculation for each dataset of around 3.2 $Å^3$/Da (*180*). The value corresponds to about 61% water content, which is similar to that of the native crystal. The small differences observed in a comparison of all the similar parameters suggest that H_2O_2 does not cause significant changes in unit cell packing.

Compared with the previously determined structure, the H_2O_2-treated His_4-Anx(Gh1) proteins reveal no striking difference in overall conformation. An omit map of oxidised Anx(Gh1) obtained from a crystal produce using the 10 mM H_2O_2 cocrystallisation method (dataset G40_8, ratio x = n(H_2O_2)/n(protein) = 20), shows that no $2F_o$-F_c peak exists to connect the side chain area of C116G and C243G (Figure 8-3a). It is important to note that the positive F_o-F_c map exhibits two independent density blobs in this region, pointing away in opposite directions. The two glycine residues were then substituted by cysteines and the side chains were built according to the omitted map. After structural refinement, a new electron density map was produced (Figure 8-3b), indicating the two cysteines stay in a reduced form, separated by a distance of 5.43 Å. Electron density maps obtained from other H_2O_2 cocrystallisation (dataset G22_14 and G33_2_9) and soaking (G44_1) methods, also reveal an open conformation of Cys116 and Cys243 (data not shown).

Dataset	G22_14	G33_2_9	G40_8	G44_1
soaked/co-crystallised	co-crystallised	co-crystallised	co-crystallised	soaked
X-ray source	SRS 14.1	SRS 14.1	ESRF BM14	ESRF BM14
Wavelength (Å)	0.979	1.541	1.033	0.979
Space group	$P3_112$	$P3_112$	$P3_112$	$P3_112$
Unit cell dimension (Å)	61.2, 61.2, 215.3	61.0, 61.0, 214.0	61.2, 61.2, 214.5	60.9, 60.9, 211.7
Resolution (Å)	3.1	2.9	2.9	3.2
No. of measurements	30921 (2512)	54083 (4057)	69614 (9270)	48216 (6554)
No. of independent measurements	6679 (841)	10289 (1405)	10539 (1512)	7528 (1085)
Completeness (%)	88.9 (87.4)	98.2 (93.2)	99.7 (98.9)	98.2 (99.0)
Multiplicity	4.2 (2.6)	5.3 (2.9)	6.6 (6.1)	6.4 (6.0)
R_{merge}	0.084 (0.379)	0.100 (0.479)	0.086 (0.331)	0.084 (0.952)
R-factor	0.23	0.20	0.22	0.27
R_{free} (%)	0.31	0.28	0.28	0.36

Table 8-7 Data collection and structural refinement statistics for crystals of H_2O_2-treate His_4-Anx(Gh1). Values for the highest resolution shell are given in parentheses.

R_{merge}: $\sum(I-\bar{I})/\sum I$, for all measurements

R-factor: $\sum(|F_o|-|F_c|)/\sum|F_o|$

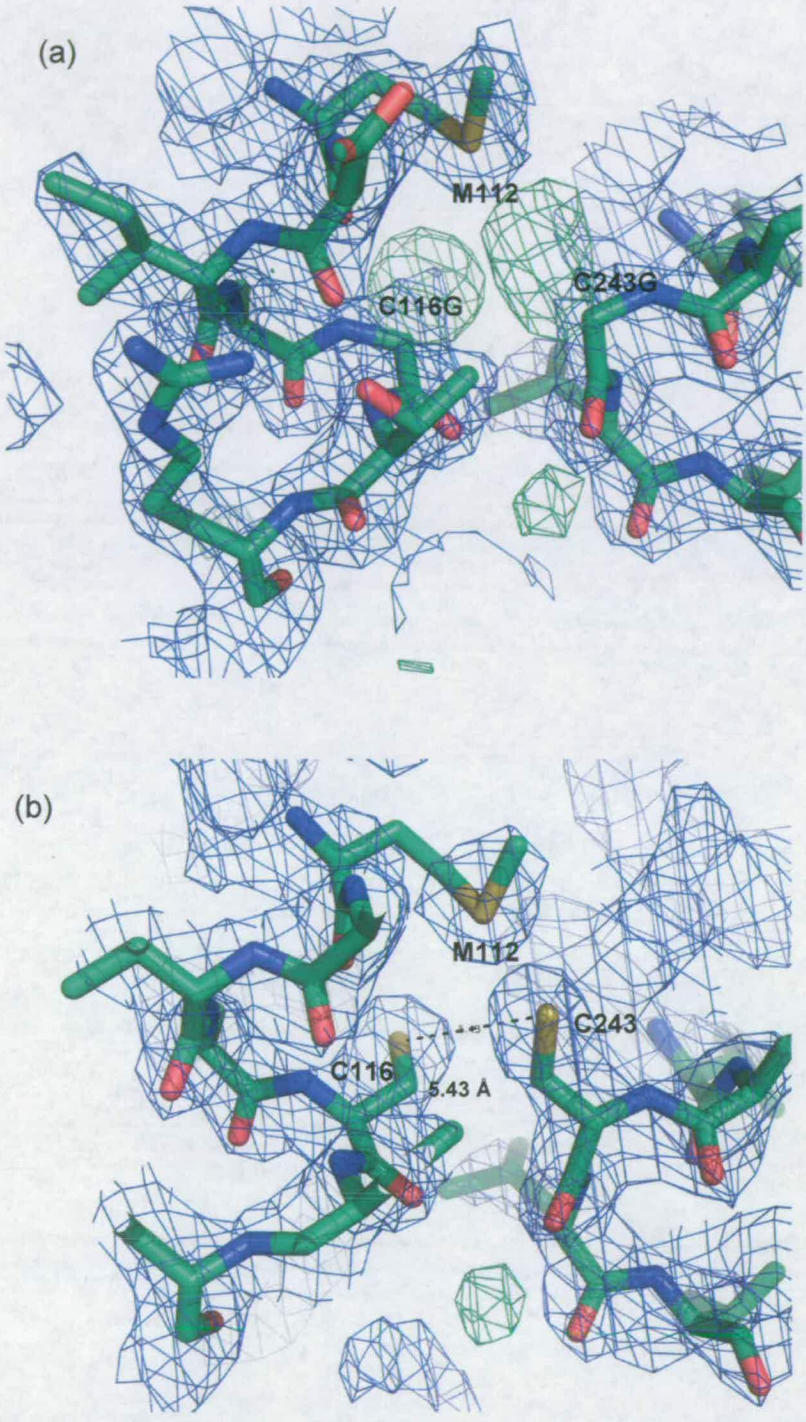

Figure 8-3 (a) Omit map obtained from the C116G and C243G mutant model of Anx(Gh1). $2F_o-F_c$ map id shown in blue and contoured at 2.0σ, while positive F_o-F_c map is shown in green and contoured at 3.0σ. (b) Anx(Gh1) refinement with substitution of cysteine for glycine, built on the basis of omit maps. $2F_o-F_c$ map is shown in blue and contoured at 2.0σ, while positive F_o-F_c map is shown in green and contoured at 3.0σ. The two blobs at Cys116 and Cys243 in the positive F_o-F_c map disappears after substitute the glycine to cysteine.

8.4 Discussion

Several reasons might account for the failure of trypsin digest fingerprinting. Firstly, the presence of H_2O_2 may cause the complication of in peptide fingerprinting. It has been presumed that the protein forms a heterogeneous oligomer using intermolecular disulfide bonds. Although iodoacetamide has been added, the sulfhydryl group of cysteine in Anx(Gh1) is oxidised to sulfenic acid (CSOH) in the presence of H_2O_2, and is not reactive with the modifying reagent. The unstable sulfenic group on an intact protein, or a half-digested protein, easily forms a disulfide bond easily with another cysteine-containing peptide or half-digested protein (*181*). The number of combinations of all possible species containing cysteine is enormous. This explains why the spectrum peaks cannot be assigned using the molecular weight matrix, which is calculated merely by summation of any two cysteine-containing peptides (Table 8-4). Since blocking the thiol group from non-specific oxidation reaction failed, removal of the residual H_2O_2, after the oxidation reaction, is the alternative approach. Separation using chromatography seems to be the most efficient method. A PD-10 desalting column has been reported to remove excess H_2O_2 successfully, before trypsin digestion (*182*). Additional steps conjugated to the separation step are required to optimise the procedure and reduce the complication in data analysis.

Secondly, the excess H_2O_2 might produce other oxidised byproducts instead of disulfide bond. A previous study, aimed at studying the kinetics of the reaction of cysteine and hydrogen peroxide, demonstrated that oxidation of cysteine by H_2O_2 is based on a two-step nucleophilic reaction, shown in scheme I (*183*).

$$CSH \xleftrightarrow{Ka} CS^- + H^+$$

$$(1)\ CS^- + H_2O_2 \xrightarrow{K1} CSOH + HO^-$$

$$(2)\ CSOH + CS^- \xrightarrow{K2} CSSC + HO^-$$

Scheme I

In order to evaluate the kinetics of the two-step reaction, the authors of the study performed a series of experiment, in which the ratio of the starting concentrations of cysteine and hydrogen peroxide, $[H_2O_2]/[CSH]$, was varied. They found that at $[H_2O_2]/[CSH]$ ratios of 0.01 to 2.3, cysteine forms the reactive sulfenic acid intermediate (CSOH) in the first step. However, the disulfide (CSSC) concentration, formed in the second step, declined as the $[H_2O_2]/[CSH]$ ratio becomes bigger than 10. This is because the excess H_2O_2 starts to compete with CS^- in the second step to produce CSSC. At an $[H_2O_2]/[CSH]$ ratio of 1000:1, instead of CSSH formation, the excessive H_2O_2 was found to react with sulfenic acid (CSOH) to form other products such as cysteine sulfinic acid (CSO_2H) and cysteine sulfonic acid (CSO_3H). In the tryptic mapping experiments, varying H_2O_2/protein molar ratios from 50 to 5000 have been employed. As Anx(Gh1) contains four cysteine residues, the actual H_2O_2/CSH ratios are varied from 12.5 to 1250. According to the reported parameters, an excess of H_2O_2 of more than 1000-fold in the trypsin digest mapping would affect the reaction, so as to produce other byproducts. This perfectly explains the missing mass peak in MALDI spectra, corresponding to the correctly cleaved peptides containing one single cysteine, at high H_2O_2/protein molar ratio (Table 8-3, trials 5, 8 and 9). As a result, the experimental trials were not in an optimal condition to monitor the disulfide bond formation. A lower concentration H_2O_2 treatment (H_2O_2/protein ratio no more than 10) should be enough to oxidise the two near cysteines in Anx(Gh1).

As seen in the crystal structure of His_4-Anx(Gh1), Cys116 and Cys243 are located in helix B in repeat II, and helix E in repeat IV, respectively. The torsion angles N-C_α-C_β-S of the two residues are -62° for Cys116, and -75° for Cys243, with a distance of 5.5 Å between the sulfur atoms (*24*). The authors suggest that the presence of Met112 near the two cysteine residues would assist the two cysteine residues in maintaining their reduced state, due to hydrogen bonding of both sulfhydryl groups to the methionine. Theoretically, to form a disulfide bond, the two sulfur atoms should satisfy the geometry of the disulfide bond, with torsion angle C_β-S-S-C_β near ±90°, and a distance close to 2.2 Å. The authors proposed a likely geometry with torsion angles N-C_α-C_β-S = 65° for Cys116, 102° for Cys243, and S-S distance = 2.2 Å. However, the torsion angle C_β-S-S-C_β is -160° in the proposed geometry, which is less than favourable for disulfide bond formation. Other torsion angles have also been investigated, but none can satisfy the disulfide geometry constraints. Therefore, the assumption that the putative role of Anx(Gh1) in the response to oxidative stress is conducted by oxidation of the two adjacent cysteine residues, does not seem to be geometrically possible, unless a drastic conformational change occurs after oxidation. An X-ray structural study on human peroxiredoxin 5 has shown that two cysteine residues, Cys47 and Cys151, with an S-S distance of 13.8 Å, adopt a conformational change to form an intramolecular disulfide bond, after peroxide oxidation (*184*). The crystal structures of H_2O_2-treated His_4-Anx(Gh1) show similar overall conformation compared with the native protein, which indicates that the protein does not undergo conformational changes or domain movement in order to satisfy the disulfide geometry, in the presence of H_2O_2. The two cysteine residues which remain in open form after addition of H_2O_2 suggest that the putative function of Anx(Gh1) in the oxidative stress response, remains uncertain.

9 Summary, conclusions and future work

It has been well known that annexins associate with membranes in response to the stimuli of intracellular Ca^{2+} ions. The X-ray structures of Ca^{2+}-bound annexins have demonstrated their unique Ca^{2+}-binding sites on the surface of their C-terminal core, by which we can visualise the Ca^{2+}-dependent membrane binding behaviour. In addition to the canonical Ca^{2+} binding motifs conserved on the convex surface, some annexin members show Ca^{2+}-independent membrane binding abilities.

In the present studies, the membrane binding behaviour of AnxA1 N-terminal peptides in the absence Ca^{2+} of has been investigated. The N-terminal tail, harboured in apo-AnxA1, undergoes a domain movement in the presence of Ca^{2+}. The Ca^{2+}-bound AnxA1 adopts an open form and allows the N-terminus to bind to a second membrane. Plant annexins also reveal a direct interaction with membranes in the absence of Ca^{2+}, albeit with a different mechanism. It is demonstrated that the conservation of the positively charged and aromatic residues on the convex surface is an important determinant of this mechanism.

The low affinity for Ca^{2+} of plant annexins in the absence of membranes has caused difficulty in obtaining an X-ray structure of Ca^{2+}-bound Anx(Gh1). In this study, His_4-Anx(Gh1) has been successfully cocrystallised in the presence of high Ca^{2+} concentration, and the first crystal structure of a Ca^{2+}-bound plant annexin is reported. Two type II and one type III binding sites were located in loop regions in repeats I and IV.

The putative RedOx function of Anx(Gh1) could not be proven by tryptic digestion mapping and crystallographic experiments. Although the side chains of Cys116 and Cys243 are located in spatial vicinity in crystal structure of native protein, treatment with H_2O_2 did not

produce the anticipated disulfide link between the two cysteines. To characterise the peroxidase activity of Anx(Gh1), further assays will be required.

9.1 The open form of AnxA1 triggered by Ca^{2+} ions

The N-terminal domain of AnxA1 has been thought to be involved in the membrane aggregation activity in the annexin protein family. The unique Trp12 in the N-terminal domain serves as an excellent intrinsic fluorescence probe to monitor the domain movement triggered by the Ca^{2+}-binding on its convex surface. A slight red shift of tryptophan emission maximum wavelength upon Ca^{2+} addition suggests an open form of AnxA1. The conformational changes are further confirmed by the observation of an increase in fluorescence intensity due to the declining quenching effects of Met248 on the C-terminal core. The secondary structure components analysis obtained by CD shows an increase in α-helical conformation in the presence of Ca^{2+}, even though the increase is not significant. On the contrary, pH does not play an important factor in conformational constitution in the absence of membranes. The results show that Ca^{2+} ions serve as a key to control the open and closed forms of AnxA1. The expelled N-terminal domain in the open form is important in the mechanism of membrane aggregation.

9.2 Membrane Aggregation initiated by AnxA1

Membrane aggregation mediated by AnxA1 is confirmed by measuring the liposome turbidity using spectrophotometric absorbance at 450 nm. A significant increase in absorbance was observed upon addition of AnxA1 and Ca^{2+} into SUV solution. SANS profiles also indicate that the distance between two membranes becomes closer in the presence of AnxA1 and Ca^{2+}. Fluorescence analysis shows that Trp12 is in a more hydrophobic environment at the membrane aggregation status. The results show a direct

interaction of the N-terminal domain with membranes. Interestingly, about 3% increase in α-helical component of AnxA1 upon membrane aggregation indicates the presence of membranes assists the α-helical folding of AnxA1.

The crucial role of the N-terminal domain of AnxA1 in membrane aggregation is confirmed by a series of biophysical experiments of AnxA1 N-terminal peptides. Firstly, the peptides show a phospholipid monolayer penetration activity in the absence of Ca^{2+}. Secondly, the folding of AnxA1 N-terminal peptide reveals a dramatic increase in α-helical component upon the addition of SUVs into the peptide solution. Thirdly, neutron diffractometry study shows the N-terminal peptides are located at the interface between the phospholipid headgroup and solvent in the multiple-stack membrane system. The neutron scattering density profiles show the peptides lie parallel to the surface of membrane bilayer. The Ca^{2+}-independent binding interaction is favourable due to the amphipathic nature of the peptides when they present in an α-helical conformation.

It is important to notice that the status of membrane aggregation initiated by AnxA1 can be restored by adding Ca^{2+} chelator. The CD profile analysis shows that the secondary structure components of AnxA1 in the presence of SUVs and Ca^{2+} ions are recovered after addition of EDTA. It is assumed that chelation of the Ca^{2+} ions coordinated by the primary Ca^{2+}-binding sites on the convex surface makes AnxA1 restores its closed form. The AnxA1 protein with its N-terminal tail inserted loses the secondary membrane binding ability and dissociates from the membranes. The recovered AnxA1 can be observed in the co-pelleting assay followed by addition of EDTA.

In summary of the results, it is thus concluded that both the canonical Ca^{2+}-biding sites on the convex surface and the N-terminal domain of AnxA1 are involved in the mechanism of membrane aggregation. In the absence of the S100A11, one can exclude the model of the

heterotetramer $(AnxA1)_2$-$(S100A11)_2$ (Figure 1-2, model C). The model of head-to-head dimer might be excluded (Figure 1-2, model B), because it contradicts the red shift of fluorescence upon Ca^{2+} addition in the absence of membrane, and the 17% retention of AnxA1 on membrane after addition EDTA in the copelleting assay. Therefore, the most likely model AnxA1 might adopt is that AnxA1 employs its primary and secondary membrane binding sites on the opposite sides of the protein to interact simultaneously with two separate membrane (Figure 1-2, model A).

9.3 Membrane-binding behaviour of plant annexins

In the present study, copelleting assays show that both Anx24(Ca32) and Anx(Gh1) bind to liposomes in a Ca^{2+}-dependent manner. Intriguingly, 20% of membrane-binding degree of these plant annexins was detected in the absence of Ca^{2+} ions. Point mutation of the positively charged and aromatic residues on the convex surface disrupts the Ca^{2+}-indendent membrane binding behaviour of plant annexins.

Thermodynamic studies have shown that His_4-Anx(Gh1) could mediate DMPS domain segregation of the DMPC/DMPS mix liposomes in the presence of Ca^{2+}. In contrast, the phase separation of the mix liposomes was not observed in the absence of Ca^{2+}. It is presumed that the Ca^{2+} ions, which are firmly captured by the Ca^{2+}-binding sites of Anx(Gh1), enhance the domain segregation of phospholipids. However, in the absence of Ca^{2+}, the sticking-out residues extend their side chains to the alkyl tails, and thus disorder the packing of phospholipids. The findings strongly support the twofold membrane binding activities of plant annexins. In addition, the two membrane binding mechanisms cause different effects on the molecular order of phospholipids.

9.4 Calcium-binding sites of cotton Anx(Gh1)

The affinity between Ca^{2+} and His_4-Anx(Gh1) has been studied by ITC. The thermodynamic experiments reveal a very low affinity between Ca^{2+} and His_4-Anx(Gh1) in the absence of SUVs. A strong binding affinity (in the low micromolar range) is only detectable in the presence of SUVs. The ITC measurement yields a stoichiometry of 4 Ca^{2+} ions per protein molecule.

His_4-Anx(Gh1) in the presence of up to 15 mM Ca^{2+} was successfully crystallised. Anomalous X-ray diffraction data show no signals for Ca^{2+} ions in the putative binding loops on the C-terminal core surface. Increase of Ca^{2+} concentration using the original crystallisation buffer failed due to the sulphate ions forming an insoluble precipitate. His_4-Anx(Gh1) was successfully crystallised in a phosphate crystallisation buffer in the presence of 50 mM $CaCl_2$. Binding of the ions caused conformational changes of the loops to satisfy coordination geometry. Three Ca^{2+} ions were located in the IAB, IVAB and IVDE loops. The finding is consistent with the sequence alignment analysis showing the endonexin sequence to be conserved in the IAB and IVAB loops. The fourth Ca^{2+} is invisible probably due to the low affinity in the absence of membrane.

9.5 Putative peroxidase activity of cotton Anx(Gh1)

Tryptic digest mapping using MALDI-TOF has been employed to evaluate the intramolecular link of the two adjacent Cys116 and Cys243 residues. The peptide mass assignments are not successful probably due to the excess of H_2O_2. There are two possible explanations. Firstly, the residual H_2O_2 oxidises any two cysteine-containing peptides after trypsin digestion and produces non-specific disulfide link, which causes complication of the mass fingerprint. Secondly, the excessive H_2O_2 in reaction with cysteines may produce

unwanted byproducts, such as cysteine sulfinic acid (CSO_2H) and cysteine sulfonic acid (CSO_3H), instead of disulfide bond.

X-ray crystallography of the H_2O_2-treated (20 μM to 20 mM) His_4-Anx(Gh1) shows no significant electron density of disulfide link detectable in the four cysteines in the protein core, especially between Cys116 and Cys243. In the native structure, the geometry of the side chains of Cys116 and Cys243 is not favourable for the formation of disulfide bond, even though rotation of the side chains can shorten the distance between the two sulphur atoms to 2.2 Å. The dihedral angle (C_β-S-S-C_β) at this status is -165° instead of the typical angle of ±90°.

9.6 Future work

SANS measurements were performed to monitor the membrane aggregation mediated by AnxA1 by analysing the changes of *d*-spacing of MLVs. A significant decrease in *d*-spacing was observed, even thought the experiments were conducted at pH 8.0. The liposome turbidity assay shows that AnxA1 exhibits a greater ability of membrane aggregation at pH 6.0. To further clarify the membrane aggregation mechanism of AnxA1, neutron experiments under varying pH conditions are required to measure the *d*-spacing of MLVs.

In the present study, phospholipid mixture DMPC/DMPS (mol 3:1) was used to evaluate the Ca^{2+}-dependent membrane binding behaviour of annexins. However, to investigate the Ca^{2+}-independent membrane binding ability of the N-terminal domain of AnxA1, further experiments with zwitterionic or non-polar phospholipids are required to analyse membrane-binding of AnxA1 N-terminal peptides by lateral surface pressure measurement and neutron diffraction.

Neutron diffraction is a powerful technique and can be used to study the orientation of full-length AnxA1 in the membrane-aggregation status, because it can not only give the information of *d*-spacing but also the scattering profile of the protein molecules in the multiple stack membrane system. The neutron diffraction experiments with AnxA1 need to be optimised by varying the lipid/protein ratio. Furthermore, Trp12 on the N-terminal domain of AnxA1 needs be deuterated to monitor the interaction of the N-terminal domain in full-length AnxA1 upon membrane aggregation.

Although the X-ray structure of Anx(Gh1) implies that the two cysteine residues, Cys116 and Cys243, play a role in oxidative stress, the putative peroxidase activity of the plant annexin remains uncertain. Chemiluminescence measurements using RedOx dye, such as luminol or ferric-xylenol orange could be used to determine the peroxidase kinetics of Anx(Gh1). The procedure of tryptic digest mapping requires further optimisation to eliminate the excessive H_2O_2 before trypsin digestion.

Appendix

PDB	protein	Resolution (Å)	No. of calcium	Calcium ID	position	Coordination number	type	number	Ca-O distance (Å)
1MCX (*12*)	AnxA1	2.03	8	CA1	IAB	8	AB'	4	G59 O=2.27, V60 O=2.34, E62 OE1=2.42, E62 OE2=2.46
								4	HOH1=2.59, HOH2=2.33, HOH333=2.60, HOH334=2.36
				CA2	IDE	7	III	3	K97 O=2.29, L100 O=2.53, E105 OE2=2.44
								4	HOH3=2.49, HOH4=2.42, HOH335=2.37, (D196 OD2=2.30)
				CA3	IIAB	7	II	5	M127 O=2.26, K129 O=2.32, G131 O=2.35, D171 OD1=2.42, D171 OD2=2.59,
								2	HOH5=2.34, HOH51=2.42
				CA4	IIAB	8	AB'	3	T132 O=2.36, E134 OE1=2.63, E134 OE2=2.53
								5	HOH6=2.29, HOH7=2.57, HOH8=2.54, HOH32=2.45, HOH214=2.53
				CA5	IIIAB	7	II	5	G210 O=2.44, R213 O=2.38, G215 O=2.38, E255 OE1=2.61, E255 OE2=2.70
								2	HOH9=2.36, HOH314=2.41
				CA6	IVAB	7	II	5	M286 O=2.37, G288 O=2.31, G290 O=2.46, E330 OE1=2.55, E330 OE2=2.49
								2	HOH10=2.46, HOH11=2.49
				CA7	IVDE	7	III	3	L328 O=2.27, T331 O=2.26, E336 OE1=2.24
								4	HOH12=2.87, HOH13=2.28, HOH183=2.29, HOH140=2.41
				CA8	IIIDE	7	III	4	D253 O=2.45, L256 O=2.60, E261 OE2=3.03, D253 OD1=3.08
								3	HOH15=2.55, HOH244=2.90, HOH337=2.80
1XJL (*13*)	AnxA2	2.59	14	CA301	IAB	7	AB'	4	G50A O=2.48, V51A O=2.84, E53A OE1=2.95, E53A OE2=2.22
								3	HOH8=2.31, HOH9=2.48, HOH208=2.29
				CA302	IDE	5	III	3	K88A O=2.39, L91A O=2.42, E96A OE1=2.37
								2	HOH10=2.52, (E36 OE2=2.96)
				CA303	IIAB	5	II	5	M118A O=2.40, G120A O=2.66, G122A O=2.48, D162A OD1=3.21, D162A OD2=2.19
				CA304	IIIAB	7	II	5	G202A O=2.87, R205A O=2.29, G207A O=2.29, E247A OE1=2.58, E247A

									OE2=2.77
								2	HOH11=2.68, HOH203=2.25
				CA305	IIIDE	5	III	3	R245A O=2.66, V248A O=2.35, E253A OE2=2.46
								2	HOH2=2.41, HOH3=3.19
				CA306	IVAB	7	II	5	M278A O=2.40, G280A O=2.20, G282A O=2.40, D322A OD1=2.47, D322A OD2=2.54
								2	HOH13=2.22, (S234A OG=2.58)
				CA307	IAB	6	AB'	4	G50B O=2.27, V51B O=2.87, E53B OE1=2.49, E53B OE2=2.55
								2	HOH1=2.32, HOH14=2.27
				CA308	IDE	5	III	3	K88B O=2.34, L91B O=2.49, E96B OE1=2.40
								2	HOH4=2.70, HOH5=2.69
				CA309	IIAB	6	II	5	M118B O=2.45, G120B O=2.32, G122B O=2.36, D162B OD1=2.53, D162B OD2=2.22
								1	HOH15=2.89
				CA310	IIIAB	6	II	5	G202B O=2.49, R205B O=2.12, G207B O=2.38, E247B OE1=2.51, E247B OE2=2.64
								1	HOH16=2.56
				CA311	IIIDE	5	III	3	R245B O=2.67, V248B O=2.44, E253B OE2=2.70
								2	HOH6=2.66, HOH7=2.63
				CA312	IVAB	6	II	5	M278B O=2.38, G280B O=2.41, G282B O=2.37, D322B OD1=2.77, D322B OD2=2.24
								1	(S234B OG=2.56)
				CA313	IIAB	6	AB'	3	T123A O=2.39, E125A OE1=2.44, E125A OE2=2.72
								3	HOH212=2.34, HOH14=2.40, HOH15=2.61
				CA314	IIAB'	6	III	3	T123B O=2.57, E125B OE1=3.09, E125B OE2=2.50
								3	HOH213=2.67, HOH217=2.36, HOH218=2.36
1AII (*14*)	AnxA3	1.95	5	CA351	IAB	5	II	5	I32 O=2.67, G34 O=2.64, G36 O=2.89, D76 OD1=2.93, D76 OD2=2.99
				CA353	IIIAB	7	II	5	G187 O=2.62, R190 O=2.57, G192 O=2.40, E232 OE1=2.60, E232 OE2=2.76
								2	HOH409=2.68, HOH576=2.71
				CA354	IIIDE	5	III	4	K230 O=2.82, L233 O=2.91, E238 OE1=3.15, E238 OE2=3.21
								1	HOH534=3.14
				CA355	IIIAB	4	AB'	3	T193 O=2.98, E195 OE1=2.89, E195 OE2=3.27
								1	HOH633=2.88

				CA357	IIAB	5	II	5	M104 O=2.80, G106 O=2.77 G108 O=2.88, E148 OE1=2.85, E148 OE2=3.98
1AXN (*15*)	AnxA3	1.78	5	CA351	IAB	5	II	5	I32 O=2.29, G34 O=2.57, G36 O=2.19, D76 OD1=3.11, D76 OD2=2.70
				CA352	IIAB	5	II	5	M104 O=2.42, G106 O=2.37 G108 O=2.38, E148 OE1=2.86, E148 OE2=4.57
				CA353	IIIAB	7	II	5	G187 O=2.32, R190 O=2.37, G192 O=2.28, E232 OE1=2.35, E232 OE2=2.53
								2	HOH406=2.66, HOH407=2.62
				CA354	IIIDE	5	III	4	K230 O=2.53, L233 O=2.41, E238 OE1=3.16, E238 OE2=3.08
								1	HOH580=2.99
				CA355	IIIAB	5	AB'	3	T193 O=2.39, E195 OE1=2.51, E195 OE2=3.02
								2	HOH458=2.79, HOH603=2.75
1ANN	AnxA4	2.3	2	CA1	IVAB	6	II	5	M257 O=2.41, G259 O=2.42, G261 O=2.37, D301 OD1=2.54, D301 OD2=2.58
								1	HOH259B=2.57
				CA2	IAB	7	II	5	M26 O=2.39, G28 O=2.35, G30 O=2.32, E70 OE1=2.66, E70 OE2=2.57
								2	HOH28A=2.64, HOH30B=2.70
1AVH (*9*)	AnxA5	2.3	5	CA1	IIAB	4	II	3	L100A O=3.03, G102A O=3.17, G104A O=3.17
								1	(L31B O=2.35)
				CA2	IAB	5	II	5	M28A O=3.60, G30A O=2.80, G32A O=2.90, E72A OE1=2.88, E72A OE2=3.02
				CA3	IAB	5	II	5	M28B O=3.25, G30B O=3.33, G32B O=2.84, E72B OE1=2.81, E72B OE2=3.30
				CA4	IVAB	5	II	5	M259A O=2.98, G261A O=2.70, G263A O=2.97, D303A OE1=3.60, D303A OE2=2.69
				CA5	IVAB	5	II	5	M259B O=2.98, G261B O=2.94, G263B O=2.74, D303B OE1=2.74, D303B OE2=2.64
1AVR (*9*)	AnxA5	2.3	5	CA321	IIAB	7	II	5	L100 O=2.42, G102 O=2.35, G104 O=2.43, D144 OD1=3.00, D144 OD2=2.46
								2	HOH478=2.36, HOH481=2.38
				CA322	IVAB	6	II	5	M259 O=2.49, G261 O=2.46, G263 O=2.36, D303 OE1=2.59, D303 OE2=2.71
								1	HOH483=2.40
				CA323	IAB	7	II	5	M28 O=2.44, G30 O=2.36, G32 O=2.44, E72 OE1=2.46, E72 OE2=2.50
								2	HOH403=2.97, HOH706=2.39
				CA324	IAB	6	AB'	3	T33 O=2.46, E35 OE1=2.50, E35 OE2=2.75
								3	HOH498=2.57, HOH499252, HOH500=2.59
				CA325	IDE	5	III	4	K70 O=2.45, L73 O=2.40, E78 OE1=2.62, E78 OE2=3.55

								1	HOH605=3.20
1SAV (*9*)	AnxA5	2.5	5	CA321	IIAB	5	II	5	L100 O=2.92, G102 O=2.00, G104 O=2.41, D144 OD1=3.23, D144 OD2=2.29
				CA322	IVAB	5	II	5	M259 O=2.58, G261 O=3.49, G263 O=2.50, D303 OE1=2.82, D303 OE2=3.27
				CA323	IAB	6	II	5	M28 O=2.57, G30 O=2.69, G32 O=2.95, E72 OE1=2.14, E72 OE2=3.19
								1	HOH402=2.93
				CA324	IAB	4	AB'	3	T33 O=3.53, E35 OE1=3.54, E35 OE2=3.74
								1	HOH457=2.88
				CA325	IDE	4	III	2	K70 O=3.23, L73 O=3.00
								1	HOH474=3.30
1ANW (*185*)	AnxA5	2.4	4	CA351	IAB	6	II	5	M28A O=2.35, G30A O=2.33, G32A O=2.40, E72A OE1=2.70, E72A OE2=2.34
								1	HOH823=2.32
				CA352	IVAB	7	II	5	M259A O=2.20, G261A O=2.16, G263A O=2.12, D303A OD1=2.96, D303A OD2=2.76
								2	HOH902=3.04, HOH981=1.83
				CA353	IAB	7	II	5	M28B O=2.36, G30B O=2.46, G32B O=2.37, E72B OE1=2.51, E72B OE2=2.54
								2	HOH757=2.27, HOH861=2.23
				CA354	IVAB	6	II	5	M259B O=2.43, G261B O=2.37, G263B O=2.55, D303B OD1=2.69, D303B OD2=2.48
								1	HOH891=2.68
1ANX (*165*)	AnxA5	1.9	12	CA321A	IIIAB	8	II	5	G183A O=2.39, K186A O=2.33, G188A O=2.43, E228A OE1=2.54, E228A OE2=2.67
								3	HOH331A=2.52, SO4 322A O1=2.70, SO4 322A O4=2.71
				CA323A	IAB	5	II	5	M28A O=2.19, G30A O=2.44, G32A O=2.33, E72A OE1=2.61, E72A OE2=2.70
				CA324A	IDE	3	III	3	K70A O=2.12, L73A O=2.30, E78A OE2=2.64
				CA325A	IIIDE	5	III	5	D226A O=2.50, D226A OD1=2.89, T229A O=2.86, E234A OE1=2.89, E234A OE2=3.38
				CA321B	IIIAB	8	II	5	G183B O=2.16, K186B O=2.65, G188B O=2.46, E228B OE1=2.26, E228B OE2=2.40
								3	HOH349B=2.52, SO4 322B O3=2.11, SO4 322B O4=2.39
				CA323B	IAB	6	II	5	M28B O=2.38, G30B O=2.73, G32B O=2.33, E72B OE1=2.41, E72B OE2=2.60
								1	HOH459B=2.98
				CA324B	IDE	4	III	3	K70B O=2.18, L73B O=2.33, E78B OE2=2.34

								1	HOH473B=2.85
				CA325B	IIIDE	5	III	5	D226B O=2.49, D226B OD1=3.01, T229B O=2.82, E234B OE1=3.02, E234B OE2=3.25
				CA321C	IIIAB	8	II	5	G183C O=2.18, K186C O=2.40, G188C O=2.37, E228C OE1=2.54, E228C OE2=2.51
								3	HOH386B=2.47, SO4 322C O3=2.56, SO4 322C O4=2.30
				CA323C	IAB	6	II	5	M28C O=2.18, G30C O=2.70, G32C O=2.19, E72C OE1=2.53, E72C OE2=2.55
								1	HOH378C=2.75
				CA324C	IDE	3	III	3	K70C O=2.21, L73C O=2.20, E78C OE2=2.67
				CA325C	IIIDE	5	III	5	D226C O=2.41, D226C OD1=2.76, T229C O=2.87, E234C OE1=3.04, E234C OE2=3.20
1A8A (*29*)	AnxA5	1.9	10	CA401	IAB	7	II	5	M26 O=2.34, G28 O=2.42, G30 O=2.41, E70 OE1=2.46, E70 OE2=2.57
								2	HOH635=2.60, HOH636=2.54
				CA402	IDE	5	III	4	K68 O=2.40, L71=2.40, E76 OE1=2.51, E76 OE2=2.54
								1	HOH591=2.50
				CA403	IAB	6	AB'	3	T31 O=2.48, E33 OE1=2.51, E33 OE2=2.73
								3	HOH630=2.55, HOH638=2.56, HOH637=2.48
				CA404	IIAB	6	II	6	L98 O=2.46, G100 O=2.78, A101 O=2.48, G102 O=2.35, D142 OD1=2.60, D142 OD2=2.48
				CA405	IIDE	4	III	2	V140 O=2.46, T143 O=2.43
								2	HOH607=2.58, HOH640=2.45
				CA406	IIAB'	4	III	3	T103 O=2.45, E105 OE1=2.45, E105 OE2=2.52
								1	HOH639=2.52
				CA407	IIIAB	7	II	5	G181 O=2.34, K184 O=2.43, G186 O=2.43, E226 OE1=2.51, E226 OE2=2.48
								2	HOH512=2.50, *GPS O14=2.36
				CA408	IIIDE	4	III	4	D224 O=2.53, T227 O=2.43, E232 OE1=2.83, E232 OE2=2.53
				CA409	IIIAB	7	AB'	3	T187 O=2.41, E189 OE1=2.62, E189 OE2=2.65
								4	HOH626=2.50, HOH642=2.47, HOH644=2.69, *GSE O16=2.56
				CA410	IVAB	6	II	6	M257 O=2.44, G259 O=2.51, A260 O=2.47, G261 O=2.40, D301 OD1=2.49 D301 OD2=2.53
1A8B (*5*)	AnxA5	1.9	10	CA401	IAB	7	II	5	M26 O=2.29, G28 O=2.38, G30 O=2.35, E70 OE1=2.52, E70 OE2=2.68
								2	HOH759=2.36, HOH761=2.52
				CA402	IDE	5	III	4	K68 O=2.41, L71=2.44, E76 OE1=2.56, E76 OE2=2.46

									1	HOH699=2.36
				CA403	IAB	4	AB'	3	T31 O=2.88, E33 OE1=2.55, E33 OE2=2.81	
								1	HOH580=2.41	
				CA404	IIAB	7	II	6	L98 O=2.39, G100 O=2.49, A101 O=2.60, G102 O=2.44, D142 OD1=2.47, D142 OD2=2.71	
								1	HOH737=2.45	
				CA405	IIDE	3	III	2	V140 O=2.41, T143 O=2.51	
								1	HOH768=2.52	
				CA406	IIAB	3	AB'	3	T103 O=3.05, E105 OE1=2.48, E105 OE2=2.49	
				CA407	IIIAB	7	II	5	G181 O=2.22, K184 O=2.44, G186 O=2.43, E226 OE1=2.46, E226 OE2=2.64	
								2	HOH500=2.50, *GPE O14=2.33	
				CA408	IIIDE	5	III	4	D224 O=2.41, T227 O=2.35, E232 OE1=2.74, E232 OE2=2.70	
								1	HOH705=2.36	
				CA409	IIIAB	4	AB'	3	T187 O=2.44, E189 OE1=2.46, E189 OE2=2.65	
								1	HOH627=2.60	
				CA410	IVAB	5	II	5	M257 O=2.36, G259 O=2.82, G261 O=2.52, D301 OD1=2.47 D301 OD2=2.52	
2RAN (*166*)	AnxA5	1.89	7	CA320	IAB	6	II	5	M26 O=2.41, G28 O=2.43, G30 O=2.39, E70 OE1=2.54, E70 OE2=2.56	
								1	HOH404=2.53	
				CA321	IDE	5	III	4	K68 O=2.46, L71 O=2.37, E76 OE1=2.59, E76 OE2=2.99	
								1	HOH499=2.64	
				CA322	IIAB	7	II	6	L98 O=2.38, G100 O=2.54, A101 O=2.49, G102 O=2.54, D142 OD1=2.64, D142 OD2=2.74	
								1	HOH408=2.68	
				CA323	IIDE	6	III	3	V140 O=2.41, T143 O=2.42, Q148 OE1=2.59	
								3	HOH409=2.54, HOH410=2.54, HOH411=2.62	
				CA324	IIIAB	7	II	5	G181 O=2.33, K184 O=2.53, G186 O=2.41, E226 OE1=2.60, E226 OE2=2.59	
								2	HOH412=2.52, HOH414=2.57	
				CA325	IIIDE	6	III	4	D224 O=2.55, T227 O=2.45, E232 OE1=2.63, E232 OE2=3.22	
								2	HOH418=2.76, HOH503=2.66	
				CA326	IVAB	7	II	6	M257=2.43, K258 O=2.84, A260 O=2.42, G261 O=2.41, D301 OD1=2.58, D301 OD2=2.47	
								1	HOH419=2.55	

1ALA (*186*)	AnxA5	2.25	3	CA400	IAB	5	II	5	M28 O=2.46, G30 O=2.22, G32 O=2.60, E72 OE1=2.18, E72 OE2=2.62
				CA401	IIAB	5	II	5	I100 O=2.15, G102 O=2.10, G104 O=2.35, E144 OE1=2.85, E144 OE2=3.48
				CA402	IVAB	6	II	5	M259 O=2.42, G261 O=2.64, G263 O=2.15, D303 OD1=2.97, D303 OD2=2.31
								1	HOH469=2.64
1YII (*187*)	AnxA5	1.42	3	CA401	IAB	6	II	5	M28 O=2.55, G30 O=2.45, G32 O=2.52, E72 OE1=2.61, E72 OE2=2.60
								1	HOH241=2.65
				CA402	IIAB	6	II	5	I100 O=2.71, G102 O=2.67, G104 O=2.68, E144 OE1=2.90, E144 OE2=4.54
								1	HOH284=2.99
				CA403	IVAB	7	II	5	M259 O=2.46, G261 O=2.43, G263 O=2.51, D303 OD1=2.60, D303 OD2=2.59
								2	HOH276=2.72, HOH277=2.70
1AVC (*18*)	AnxA6	2.9	6	CA1	VAB	5	II	5	G378 O=2.73, L379 O=2.52, G380 O=2.45, E420 OE1=2.49, E420 OE2=2.85
				CA2	IDE	3	III	3	K75 O=2.79, L78 O=2.69, E83 OE1=3.21
				CA3	IVAB	5	II	5	M264 O=2.66, G266 O=2.47, G268 O=2.70, D308 OD1=2.73, D308 OD2=2.60
				CA4	IIIAB	3	II	3	G188 O=2.68, G193 O=2.68, E233 OE1=2.63
				CA5	VIIIAB	3	II	3	G614 O=2.76, G616 O=2.29, D656 OD2=2.53
				CA6	VIAB	4	II	4	M448 O=2.58, G450 O=2.54, G452 O=2.53, D492 OD1=2.65
1W3W (*20*)	AnxA8	1.99	1	CA1328	IVAB	6	II	5	M266 O=2.39, G268 O=2.42, G270 O=2.29, D310 OD1=3.00, D310 OD2=2.41
								1	HOH86=2.40
1AEI (*22*)	AnxB12	2.8	24	CA1	IDE	4	III	4	K68E O=2.29, L71E O=2.22, E76E OE2=2.24, E105A OE2=2.16
				CA2	IDE	4	III	4	K68D O=2.19, L71D O=2.34, E76D OE2=2.10, E105B OE2=2.12
				CA3	IDE	4	III	4	K68F O=2.22, L71F O=2.26, E76F OE2=2.06, E105C OE2=2.05
				CA4	IDE	4	III	4	K68B O=2.28, L71B O=2.42, E76B OE2=2.11, E105D OE2=2.11
				CA5	IDE	4	III	4	K68A O=2.21, L71A O=2.38, E76A OE2=2.14, E105E OE2=2.10
				CA6	IDE	4	III	4	K68C O=2.21, L71C O=2.15, E76C OE2=2.14, E105F OE2=2.08
				CA7	IAB	5	II	5	M26A O=2.47, G28A O=2.14, G30A O=2.23, E70A OE1=2.29, E70A OE2=2.20
				CA8	IAB	5	II	5	M26B O=2.29, G28B O=2.14, G30B O=2.25, E70B OE1=2.44, E70B OE2=2.15
				CA9	IAB	5	II	5	M26C O=2.38, G28C O=2.19, G30C O=2.04, E70C OE1=2.17, E70C OE2=2.23
				CA10	IAB	5	II	5	M26D O=2.48, G28D O=2.26, G30D O=2.22, E70D OE1=2.15, E70D OE2=2.12

				CA11	IAB	5	II	5	M26E O=2.21, G28E O=2.22, G30E O=2.12, E70E OE1=2.21, E70E OE2=2.15
				CA12	IAB	5	II	5	M26F O=2.59, G28F O=2.20, G30F O=2.07, E70F OE1=2.16, E70F OE2=2.14
				CA13	IIIAB	6	II	6	G181A O=2.23, Q184A O=2.11, I185A O=2.66, G186A O=2.18, E226A OE1=2.20, E226A OE2=2.13
				CA14	IIIAB	6	II	6	G181B O=2.31, Q184B O=2.19, I185B O=2.56, G186B O=2.35, E226B OE1=2.20, E226B OE2=2.09
				CA15	IIIAB	6	II	6	G181C O=2.41, Q184C O=2.18, I185C O=2.53, G186C O=2.20, E226C OE1=2.11, E226C OE2=2.15
				CA16	IIIAB	6	II	6	G181D O=2.23, Q184D O=2.12, I185D O=2.72, G186D O=2.28, E226D OE1=2.14, E226D OE2=2.15
				CA17	IIIAB	6	II	6	G181E O=2.53, Q184E O=2.23, I185E O=2.37, G186E O=2.10, E226E OE1=2.15, E226E OE2=2.18
				CA18	IIIAB	6	II	6	G181F O=2.38, Q184F O=2.07, I185F O=2.55, G186F O=2.14, E226F OE1=2.18, E226F OE2=2.21
				CA19	IVAB	5	II	5	M257A O=2.73, G259A O=2.29, G261A O=2.00, D301A OD1=2.18, D301A OD2=2.09
				CA20	IVAB	5	II	5	M257B O=2.84, G259B O=2.19, G261B O=2.00, D301B OD1=2.16, D301B OD2=2.18
				CA21	IVAB	5	II	5	M257C O=2.75, G259C O=2.17, G261C O=2.18, D301C OD1=2.10, D301C OD2=2.17
				CA22	IVAB	5	II	5	M257D O=2.71, G259D O=2.23, G261D O=2.06, D301D OD1=2.17, D301D OD2=2.11
				CA23	IVAB	5	II	5	M257E O=2.94, G259E O=2.07, G261E O=2.09, D301E OD1=2.25, D301E OD2=2.26
				CA24	IVAB	5	II	5	M257F O=2.64, G259F O=2.16, G261F O=2.22, D301F OD1=2.23, D301F OD2=2.14
2IIC (27)	Alpha-1 giardin	2.93	4	CA401	IDE	4	IIIb	3	K53A O=2.88, I56A O=2.34, E62A OE2=2.78
								1	HOH83=2.52
				CA402	IDE	5	IIIb	4	K53B O=3.04, I56B O=2.93, N58B OD1=3.04, E62B OE2=2.60
								1	HOH89=2.95
				CA403	IDE	6	IIIb	5	K53C O=2.75, I56C O=2.81, N58C OD1=2.98, E62C OE2=2.59, D126B O=3.05
								1	HOH3=3.03
				CA404	IDE	6	IIIb	4	K53D O=2.69, I56D O=3.16, N58D OD1=2.78, E62D OE2=2.57
								2	HOH5=3.00, HOH96=2.80

Appendix: A summary table of calcium coordination found in vertebrate annexins (AnxA1, AnxA2, AnxA3, AnxA4, AnxA5, AnxA6 and AnxA8) and non-vertebrate annexins (AnxB12 and Alpha-1 giardin). Ca^{2+} coordinated by solvent molecules is highlighted in grey.

References

1. Streb, H., Heslop, J. P., Irvine, R. F., Schulz, I., and Berridge, M. J. (1985) *J Biol Chem 260*, 7309-15.
2. Klee, C. B. (1988) *Biochemistry 27*, 6645-53.
3. Burgoyne, R. D., and Geisow, M. J. (1989) *Cell Calcium 10*, 1-10.
4. Raynal, P., and Pollard, H. B. (1994) *Biochim. Biophys. Acta 1197*, 63-93.
5. Swairjo, M. A., and Seaton, B. A. (1994) *Annu. Rev. Biophys. Bioeng. 23*, 193-213.
6. Gerke, V., and Moss, S. E. (1997) *Biochim. Biophys. Acta 1357*, 129-54.
7. Gerke, V., and Moss, S. E. (2002) *Physiol. Rev. 82*, 331-71.
8. Gerke, V., Creutz, C. E., and Moss, S. E. (2005) *Nat Rev Mol Cell Biol 6*, 449-61.
9. Huber, R., Berendes, R., Burger, A., Schneider, M., Karshikov, A., Luecke, H., Romisch, J., and Paques, E. (1992) *J. Mol. Biol. 223*, 683-704.
10. Huber, R., Schneider, M., Mayr, I., Romisch, J., and Paques, E. P. (1990) *FEBS Lett 275*, 15-21.
11. Rosengarth, A., Gerke, V., and Luecke, H. (2001) *J. Mol. Biol. 306*, 489-98.
12. Rosengarth, A., and Luecke, H. (2003) *J. Mol. Biol. 326*, 1317-25.
13. Tran, J. T., Rosengarth, A., and Luecke, H. (2002) *Acta Crystallogr D Biol Crystallogr 58*, 1854-7.
14. Perron, B., Lewit-Bentley, A., Geny, B., and Russo-Marie, F. (1997) *J Biol Chem 272*, 11321-6.
15. Favier-Perron, B., Lewit-Bentley, A., and Russo-Marie, F. (1996) *Biochemistry 35*, 1740-4.
16. Zanotti, G., Malpeli, G., Gliubich, F., Folli, C., Stoppini, M., Olivi, L., Savoia, A., and Berni, R. (1998) *Biochem J 329 (Pt 1)*, 101-6.
17. Freemont, P. S., Driessen, H. P., Verbi, W., and Crumpton, M. J. (1990) *J Mol Biol 216*, 219-21.
18. Avila-Sakar, A. J., Creutz, C. E., and Kretsinger, R. H. (1998) *Biochim Biophys Acta 1387*, 103-16.
19. Benz, J., Bergner, A., Hofmann, A., Demange, P., Gottig, P., Liemann, S., Huber, R., and Voges, D. (1996) *J Mol Biol 260*, 638-43.
20. Rety, S., Sopkova-de Oliveira Santos, J., Dreyfuss, L., Blondeau, K., Hofbauerova, K., Raguenes-Nicol, C., Kerboeuf, D., Renouard, M., Russo-Marie, F., and Lewit-Bentley, A. (2005) *J Mol Biol 345*, 1131-9.
21. Cartailler, J. P., Haigler, H. T., and Luecke, H. (2000) *Biochemistry 39*, 2475-83.

22. Luecke, H., Chang, B. T., Mailliard, W. S., Schlaepfer, D. D., and Haigler, H. T. (1995) *Nature 378*, 512-5.

23. Hofmann, A., Proust, J., Dorowski, A., Schantz, R., and Huber, R. (2000) *J. Biol. Chem. 275*, 8072-82.

24. Hofmann, A., Delmer, D. P., and Wlodawer, A. (2003) *Eur. J. Biochem. 270*, 2557-64.

25. Wesenberg, G. E., Phillips JR, G. N., Bitto, E., Bingman, C. A., and Allard, S. T. M. *To be Published.*

26. Liemann, S., Bringemeier, I., Benz, J., Gottig, P., Hofmann, A., Huber, R., Noegel, A. A., and Jacob, U. (1997) *J Mol Biol 270*, 79-88.

27. Pathuri, P., Nguyen, E. T., Svard, S. G., and Luecke, H. (2007) *J Mol Biol 368*, 493-508.

28. Geisow, M. J., Fritsche, U., Hexham, J. M., Dash, B., and Johnson, T. (1986) *Nature 320*, 636-8.

29. Swairjo, M. A., Concha, N. O., Kaetzel, M. A., Dedman, J. R., and Seaton, B. A. (1995) *Nat. Struct. Biol. 2*, 968-74.

30. Jost, M., Weber, K., and Gerke, V. (1994) *Biochem. J. 298*, 553-9.

31. DeLano, W. L. (2002), DeLano Scientific, San Carlos, CA, USA.

32. Boersma, H. H., Kietselaer, B. L., Stolk, L. M., Bennaghmouch, A., Hofstra, L., Narula, J., Heidendal, G. A., and Reutelingsperger, C. P. (2005) *J Nucl Med 46*, 2035-50.

33. Babiychuk, E. B., and Draeger, A. (2000) *J Cell Biol 150*, 1113-24.

34. Babiychuk, E. B., and Draeger, A. (2006) *Biochem Soc Trans 34*, 374-6.

35. Goebeler, V., Ruhe, D., Gerke, V., and Rescher, U. (2006) *FEBS Lett 580*, 2430-4.

36. Hayes, M. J., Shao, D., Bailly, M., and Moss, S. E. (2006) *Embo J 25*, 1816-26.

37. Hayes, M. J., Rescher, U., Gerke, V., and Moss, S. E. (2004) *Traffic 5*, 571-6.

38. Kohler, G., Hering, U., Zschornig, O., and Arnold, K. (1997) *Biochemistry 36*, 8189-94.

39. Isas, J. M., Cartailler, J.-P., Sokolov, Y., Patel, D. R., Langer, R., Luecke, H., Hall, J. E., and Haigler, H. T. (2000) *Biochemistry 39*, 3015-22.

40. Lambert, O., Cavusoglu, N., Gallay, J., Vincent, M., Rigaud, J. L., J.-P., H., and Ayala-Sanmartin, J. (2004) *J. Biol. Chem. 279*, 10872-82.

41. Naka, M., Qing, Z. X., Sasaki, T., Kise, H., Tawara, I., Hamaguchi, S., and Tanaka, T. (1994) *Biochim Biophys Acta 1223*, 348-53.

42. Seemann, J., Weber, K., and Gerke, V. (1996) *Biochem J 319 (Pt 1)*, 123-9.

43. Zobiack, N., Gerke, V., and Rescher, U. (2001) *FEBS Lett 500*, 137-40.

44. Sudo, T., and Hidaka, H. (1998) *J Biol Chem 273*, 6351-7.

45. Meers, P., Mealy, T., Pavlotsky, N., and Tauber, A. I. (1992) *Biochemistry 31*, 6372-82.

46. Meers, P., Mealy, T., and Tauber, A. I. (1993) *Biochim. Biophys. Acta 1147*, 177-84.

47. Blackwood, R. A., and Ernst, J. D. (1990) *Biochem. J. 266*, 195-200.

48. Kaetzel, M. A., Mo, Y. D., Mealy, T. R., Campos, B., Bergsma-Schutter, W., Brisson, A., Dedman, J. R., and Seaton, B. A. (2001) *Biochemistry 40*, 4192-9.

49. Nir, S., Stutzin, A., and Pollard, H. B. (1987) *Biochim. Biophys. Acta 903*, 309-18.

50. Donnelly, S. R., and Moss, S. E. (1997) *Cell Mol Life Sci 53*, 533-8.

51. Lee, G., and Pollard, H. B. (1997) *Anal. Biochem. 252*, 160-4.

52. Andree, H. A., Willems, G. M., Hauptmann, R., Maurer-Fogy, I., Stuart, M. C., Hermens, W. T., Frederik, P. M., and Reutelingsperger, C. P. (1993) *Biochemistry 32*, 4634-40.

53. Bitto, E., and Cho, W. (1999) *Biochemistry 38*, 14094-100.

54. Solito, E., Nuti, S., and Parente, L. (1994) *Br J Pharmacol 112*, 347-8.

55. Brownstein, C., Falcone, D. J., Jacovina, A., and Hajjar, K. A. (2001) *Ann N Y Acad Sci 947*, 143-55; discussion 155-6.

56. Benevolensky, D., Belikova, Y., Mohammadzadeh, R., Trouve, P., Marotte, F., Russo-Marie, F., Samuel, J. L., and Charlemagne, D. (2000) *Lab Invest 80*, 123-33.

57. Parente, L., and Solito, E. (2004) *Inflamm Res 53*, 125-32.

58. Perretti, M., Croxtall, J. D., Wheller, S. K., Goulding, N. J., Hannon, R., and Flower, R. J. (1996) *Nat Med 2*, 1259-62.

59. Perretti, M. (1998) *Gen Pharmacol 31*, 545-52.

60. Solito, E., Romero, I. A., Marullo, S., Russo-Marie, F., and Weksler, B. B. (2000) *J Immunol 165*, 1573-81.

61. Comera, C., and Russo-Marie, F. (1995) *Br J Pharmacol 115*, 1043-7.

62. Boustead, C. M., Smallwood, M., Small, H., Bowles, D. J., and Walker, J. H. (1989) *FEBS Lett 244*, 456-60.

63. Delmer, D. P., and Potikha, T. S. (1997) *Cell Mol Life Sci 53*, 546-53.

64. Hofmann, A. (2004) *Annexins 1*, 8-18.

65. Shin, H., and Brown, R. M., Jr. (1999) *Plant Physiol 119*, 925-34.

66. Calvert, C. M., Gant, S. J., and Bowles, D. J. (1996) *Plant Cell 8*, 333-42.

67. Gidrol, X., Sabelli, P. A., Fern, Y. S., and Kush, A. K. (1996) *Proc Natl Acad Sci U S A 93*, 11268-73.

68. Gorecka, K. M., Konopka-Postupolska, D., Hennig, J., Buchet, R., and Pikula, S. (2005) *Biochem Biophys Res Commun 336*, 868-75.

69. de la Fuente, M., and Ossa, C. G. (1997) *Biophys J 72*, 383-7.

70. Creutz, C. E., and Sterner, D. C. (1983) *Biochem. Biophys. Res. Commun. 114*, 355-64.

71. de la Fuente, M., and Parra, A. V. (1995) *Biochemistry 34*, 10393-9.

72. Lambert, O., Gerke, V., Bader, M. F., Porte, F., and Brisson, A. (1997) *J. Mol. Biol. 272*, 42-55.

73. Rosengarth, A., Wintergalen, A., Galla, H., Hinz, H., and Gerke, V. (1998) *FEBS Lett. 438*, 279-84.

74. Bitto, E., Li, M., Tikhonov, A. M., Schlossman, M. L., and Cho, W. (2000) *Biochemistry 39*, 13469-77.

75. Yoon, M. K., Park, S. H., Won, H. S., Na, D. S., and Lee, B. J. (2000) *FEBS Lett. 484*, 241-5.

76. Hong, Y. H., Won, H. S., Ahn, H. C., and Lee, B. J. (2003) *J. Biochem. 134*, 427-32.

77. Weng, X., Luecke, H., Song, I. S., Kang, D. S., Kim, S., and Huber, R. (1993) *Protein Sci. 2*, 448-58.

78. Andrawis, A., Solomon, M., and Delmer, D. P. (1993) *Plant J 3*, 763-72.

79. Laemmli, U. K. (1970) *Nature 227*, 680-5.

80. Burger, A., Berendes, R., Voges, D., Huber, R., and Demange, P. (1993) *FEBS Lett. 329*, 25-28.

81. Warburg, O., and Christian, W. (1941) *Biochem. Z. 310*, 384.

82. Perkins, D. N., Pappin, D. J., Creasy, D. M., and Cottrell, J. S. (1999) *Electrophoresis 20*, 3551-67.

83. Sjolin, C., and Dahlgren, C. (1996) *Biochim Biophys Acta 1281*, 227-34.

84. Raynal, P., and Pollard, H. B. (1994) *Biochim Biophys Acta 1197*, 63-93.

85. Rothhut, B. (1997) *Cell. Mol. Life Sci. 53*, 522-6.

86. Szoka, F. J., and Papahadjopoulos, D. (1980) *Annu. Rev. Biophys. Bioeng. 9*, 467-508.

87. Pagano, R. E., and Weinstein, J. N. (1978) *Ann. Rev. Biophys. Bioeng. 7*, 435-68.

88. Mukhopadhyay, S., and Cho, W. (1996) *Biochim. Biophys. Acta 1279*, 58-62.

89. Dabitz, N., Hu, N. J., Yusof, A. M., Tranter, N., Winter, A., Daley, M., Zschornig, O., Brisson, A., and Hofmann, A. (2005) *Biochemistry 44*, 16292-300.

90. Hofmann, A., and Wlodawer, A. (2002) *Bioinformatics 18*, 209-10.

91. Hu, N. J., Currid, M., Daley, M., and Hofmann, A. (2005) *Appl Spectrosc 59*, 68A.

92. Hillenkamp, F., Karas, M., Beavis, R. C., and Chait, B. T. (1991) *Anal. Chem. 63*, 1193A-1203A.

93. Chalkley, R. J., Baker, P. R., Huang, L., Hansen, K. C., Allen, N. P., Rexach, M., and Burlingame, A. L. (2005) *Mol. Cell. Proteomics 4*, 1194-204.

94. Wiseman, T., Williston, S., Brandts, J. F., and Lin, L. N. (1989) *Anal Biochem 179*, 131-7.

95. Fisher, H. F., and Singh, N. (1995) *Methods Enzymol 259*, 194-221.

96. Zhang, Y. L., and Zhang, Z. Y. (1998) *Anal Biochem 261*, 139-48.

97. Turnbull, W. B., and Daranas, A. H. (2003) *J Am Chem Soc 125*, 14859-66.

98. Darkes, M. J., and Bradshaw, J. P. (2000) *Acta Crystallogr. D Biol. Crystallogr. D56*, 48-54.

99. Balali-Mood, K., Ashley, R. H., Hauss, T., and Bradshaw, J. P. (2005) *FEBS Lett. 579*, 1143-8.

100. Davies, S. M., Harroun, T. A., Hauss, T., Kelly, S. M., and Bradshaw, J. P. (2003) *FEBS Lett. 548*, 119-24.

101. *http://www.hmi.de/bereiche/I/DE/systeme/car_caress.html*.

102. Richard, D., Ferrand, M., and Kearley, G. J. (1996) *http://www.ill.fr/data_treat/lamp/front.html* .

103. Winter, R., and Pilgrim, W. C. (1989) *Ber Bunsenges Phys Chem 93*, 708-717.

104. Porte, F., de Santa Barbara, P., Phalipou, S., Liautard, J.-P., and Sri Widada, J. S. (1996) *Biochim. Biophys. Acta 1293*, 177-84.

105. Meers, P. (1990) *Biochemistry 29*, 3325-30.

106. Rety, S., Osterloh, D., Arie, J. P., Tabaries, S., Seeman, J., Russo-Marie, F., Gerke, V., and Lewit-Bentley, A. (2000) *Structure 8*, 175-84.

107. Hu, N. J., Bradshaw, J., Lauter, H., Buckingham, J., Solito, E., and Hofmann, A. (2007) *Biophys J.*

108. Newman, R., Tucker, A., Ferguson, C., Tsernoglou, D., Leonard, K., and Crumpton, M. J. (1989) *J Mol Biol 206*, 213-9.

109. Dang, Z., and Hisrt, J. D. (2006) *Proteins: From Analytics to Structural Genomics*, Vol. 1, 1 ed., Wiley-VCH, Weinheim.

110. Lecona, E., Turnay, J., Olmo, N., Guzman-Aranguez, A., Morgan, R. O., Fernandez, M. P., and Lizarbe, M. A. (2003) *Biochem J 373*, 437-49.

111. Turnay, J., Lecona, E., Fernandez-Lizarbe, S., Guzman-Aranguez, A., Fernandez, M. P., Olmo, N., and Lizarbe, M. A. (2005) *Biochem J 389*, 899-911.

112. Eftink, M. R. (1991) in *Biophysical and Biochemical Aspects of Fluorescence Spectroscopy* (Dewey, T. G., Ed.) pp 1-14, Plenum Press, New York.

113. Ladokhin, A. S., Jayasinghe, S., and White, S. H. (2000) *Anal Biochem 285*, 235-45.

114. Rosengarth, A., Rosgen, J., Hinz, H. J., and Gerke, V. (1999) *J. Mol. Biol. 288*, 1013-25.

115. Rosengarth, A., Rosgen, J., Hinz, H. J., and Gerke, V. (2001) *J. Mol. Biol. 306*, 825-35.

116. Seemann, J., Weber, K., Osborn, M., Parton, R. G., and Gerke, V. (1996) *Mol. Biol. Cell. 7*, 1359-1374.

117. Meers, P., Daleke, D., Hong, K., and Papahadjopoulos, D. (1991) *Biochemistry 30*, 2903-8.

118. Kastl, K., Herrig, A., Luthgens, E., Janshoff, A., and Steinem, C. (2004) *Langmuir 20*, 7246-53.

119. Seul, M., and Sammon, M. J. (1990) *Physical Review Letters 64*, 1903-1906.

120. King, G. I., Chao, N.-M., and White, S. H. (1982) *Neutron diffraction studies on incorporation of hexane into oriented lipid bilayers*, Plenum Publishing Corp., New York.

121. King, G. I., and White, S. H. (1986) *Biophys. J. 49*, 1047-1054.

122. King, G. I., and Worthington, C. R. (1971) *Phys. Lett. A 35*, 259-60.

123. Bradshaw, J. P., Darkes, M. J., and Davies, S. M. (1998) *Physica B 241/243*, 1115-21.

124. Wiener, M. C., King, G. I., and White, S. H. (1991) *Biophys. J. 60*, 568-76.

125. Wiener, M. C., and White, S. H. (1991) *Biophys. J. 59*, 162-73.

126. Nowotny, P., Ruhl, M., Nowotny, V., May, R. P., Burkhardt, N., Voss, H., and Nierhaus, K. H. (1994) *Biophys Chem 53*, 115-22.

127. Hirai, M., Iwase, H., Hayakawa, T., Koizumi, M., and Takahashi, H. (2003) *Biophys J 85*, 1600-10.

128. Datta, S. A., Curtis, J. E., Ratcliff, W., Clark, P. K., Crist, R. M., Lebowitz, J., Krueger, S., and Rein, A. (2007) *J Mol Biol 365*, 812-24.

129. Petoukhov, M. V., and Svergun, D. I. (2006) *Eur Biophys J 35*, 567-76.

130. Nishiyama, Y., Kim, U. J., Kim, D. Y., Katsumata, K. S., May, R. P., and Langan, P. (2003) *Biomacromolecules 4*, 1013-7.

131. Hvidt, A., and Nielsen, S. O. (1966) *Adv. Protein. Chem. 21*, 287-386.

132. Hvidt, A., and Linderstrom-Lang, K. (1954) *Biochim. Biophys. Acta 14*, 574-5.

133. Bradshaw, J. P. (1997) *Biophys. J. 72*, 2180-6.

134. Bradshaw, J. P., Duff, K. C., Gilchrist, P. J., and Saxena, A. M. (1996) *Basic Life Sci. 64*, 191-202.

135. Johnson, J. E., and Cornell, R. B. (1999) *Mol. Membr. Biol. 16*, 217-35.

136. Hennig, L. (1999) *Biotechniques 26*, 1170-2.

137. Hoekstra, D., Buist-Arkema, R., Klappe, K., and Reutelingsperger, C. P. (1993) *Biochemistry 32*, 14194-202.

138. Wu, F., Gericke, A., Flach, C. R., Mealy, T. R., Seaton, B. A., and Mendelsohn, R. (1998) *Biophys. J. 74*, 3273-81.

139. Jacobson, K., and Papahadjopoulos, D. (1975) *Biochemistry 14*, 152-61.

140. Hofmann, A., and Huber, R. (2003) in *Annexins* (Bandorowicz-Pikula, J., Ed.) pp 38-60, Landes Bioscience, Georgetown, TX.

141. Ayala-Sanmartin, J., Vincent, M., Sopkova, J., and Gallay, J. (2000) *Biochemistry 39*, 15179-89.

142. Arboledas, D., Olmo, N., Lizarbe, M. A., and Turnay, J. (1997) *FEBS Lett. 416*, 217-20.

143. Bazzi, M. D., and Nelsestuen, G. L. (1991) *Biochemistry 30*, 7970-7.

144. Tait, J. F., Gibson, D. F., and Smith, C. (2004) *Anal Biochem 329*, 112-9.

145. Hofmann, A., Ruvinov, S., Hess, S., Schantz, R., Delmer, D. P., and Wlodawer, A. (2002) *Protein Sci 11*, 2033-40.

146. Seals, D. F., Parrish, M. L., and Randall, S. K. (1994) *Plant Physiol 106*, 1403-12.

147. Parente, R. A., and Lentz, B. R. (1986) *Biochemistry 25*, 1021-6.

148. Tokutomi, S., Lew, R., and Ohnishi, S. (1981) *Biochim Biophys Acta 643*, 276-82.

149. Meyer, H. W. (1983) *Exp Pathol 23*, 3-26.

150. Chapman, D. (1975) *Q Rev Biophys 8*, 185-235.

151. Moya-Quiles, M. R., Munoz-Delgado, E., and Vidal, C. J. (1996) *Chem Phys Lipids 79*, 21-8.

152. Patel, D. R., Isas, J. M., Ladokhin, A. S., Jao, C. C., Kim, Y. E., Kirsch, T., Langen, R., and Haigler, H. T. (2005) *Biochemistry 44*, 2833-44.

153. Patel, D. R., Jao, C. C., Mailliard, W. S., Isas, J. M., Langen, R., and Haigler, H. T. (2001) *Biochemistry 40*, 7054-60.

154. Arseneault, M., and Lafleur, M. (2006) *Chem. Phys. Lipids 142*, 84-93.

155. Brennan, S., and Cowan, P. L. (1992) *Rev Sci Instrum 63*, 850.

156. Leslie, A. G. (1999) *Acta Crystallogr D Biol Crystallogr 55*, 1696-702.

157. Leslie, A. G. (2006) *Acta Crystallogr D Biol Crystallogr 62*, 48-57.

158. Blessing, R. H. (1995) *Acta Crystallogr A 51 (Pt 1)*, 33-8.

159. (2002) *Acta Crystallogr D Biol Crystallogr 58*, 1897-970.

160. Vagin, A., and Teplyakov, A. (1997) *J. Appl. Crystallogr. 30*, 1022-5.

161. Murshudov, G. N., Vagin, A. A., and Dodson, E. J. (1997) *Acta Crystallogr D Biol Crystallogr 53*, 240-55.

162. Brunger, A. T. (1992) *Nature 355*, 472-5.

163. Emsley, P., and Cowtan, K. (2004) *Acta Crystallogr D Biol Crystallogr 60*, 2126-32.

164. Maiti, R., Van Domselaar, G. H., Zhang, H., and Wishart, D. S. (2004) *Nucleic Acids Res 32*, W590-4.

165. Sopkova, J., Renouard, M., and Lewit-Bentley, A. (1993) *J Mol Biol 234*, 816-25.

166. Concha, N. O., Head, J. F., Kaetzel, M. A., Dedman, J. R., and Seaton, B. A. (1993) *Science 261*, 1321-4.

167. Meers, P., and Mealy, T. (1993) *Biochemistry 32*, 5411-8.

168. Thiel, C., Weber, K., and Gerke, V. (1991) *J Biol Chem 266*, 14732-9.

169. Evans, T. C., Jr., and Nelsestuen, G. L. (1994) *Biochemistry 33*, 13231-8.

170. Schlaepfer, D. D., and Haigler, H. T. (1987) *Biol. Chem. 262*, 6931-7.

171. Glenney, J. (1986) *J Biol Chem 261*, 7247-52.

172. Schlaepfer, D. D., and Haigler, H. T. (1987) *J Biol Chem 262*, 6931-7.

173. Huber, R., Romisch, J., and Paques, E. P. (1990) *Embo J 9*, 3867-74.

174. Thunnissen, M. M., Kalk, K. H., Drenth, J., and Dijkstra, B. W. (1990) *J Mol Biol 216*, 425-39.

175. Scott, D. L., White, S. P., Browning, J. L., Rosa, J. J., Gelb, M. H., and Sigler, P. B. (1991) *Science 254*, 1007-10.

176. Scott, D. L., White, S. P., Otwinowski, Z., Yuan, W., Gelb, M. H., and Sigler, P. B. (1990) *Science 250*, 1541-6.

177. Paget, M. S., and Buttner, M. J. (2003) *Annu Rev Genet 37*, 91-121.

178. Griffin, P. R., MacCoss, M. J., Eng, J. K., Blevins, R. A., Aaronson, J. S., and Yates, J. R. r. (1995) *Rapid. Commun. Mass. Spectrom. 9*, 1546-51.

179. Sechi, S., and Chait, B. T. (1998) *Anal. Chem. 70*, 5150-8.

180. Matthews, B. W. (1968) *J Mol Biol 33*, 491-7.

181. Park, H. S., Jin, D. K., Shin, S. M., Jang, M. K., Longo, N., Park, J. W., Bae, D. S., and Bae, Y. S. (2005) *Diabetes 54*, 3175-81.

182. Oliveira, M. A., Guimaraes, B. G., Cussiol, J. R., Medrano, F. J., Gozzo, F. C., and Netto, L. E. (2006) *J Mol Biol 359*, 433-45.

183. Luo, D., Smith, S. W., and Anderson, B. D. (2005) *J Pharm Sci 94*, 304-16.

184. Declercq, J. P., Evrard, C., Clippe, A., Stricht, D. V., Bernard, A., and Knoops, B. (2001) *J Mol Biol 311*, 751-9.

185. Lewit-Bentley, A., Morera, S., Huber, R., and Bodo, G. (1992) *Eur. J. Biochem. 210*, 73-7.

186. Bewley, M. C., Boustead, C. M., Walker, J. H., Waller, D. A., and Huber, R. (1993) *Biochemistry 32*, 3923-9.

187. Ortlund, E. A., Chai, G., Genge, B., Wu, L. N. Y., Wuthier, R. E., and Lebioda, L. (2005) *Annexins 1*, 183-90.